Dynamics of Electromagnetic Systems for Energy Harvesting and Filtering

by

Benjamin A. M. Owens

Department of Mechanical Engineering and Materials Science
Duke University

Date: _____

Approved:

_____
Brian P. Mann, Supervisor

_____
Robert E. Kielb

_____
Laurens E. Howle

_____
Donald B. Bliss

_____
Thomas P. Witelski

Dissertation submitted in partial fulfillment of the requirements for the degree of Doctor of Philosophy in the Department of Mechanical Engineering and Materials Science
in the Graduate School of Duke University
2014

Abstract

Dynamics of Electromagnetic Systems for Energy Harvesting and Filtering

by

Benjamin A. M. Owens

Department of Mechanical Engineering and Materials Science
Duke University

Date: _____

Approved:

_____
Brian P. Mann, Supervisor

_____
Robert E. Kielb

_____
Laurens E. Howle

_____
Donald B. Bliss

_____
Thomas P. Witelski

An abstract of a dissertation submitted in partial fulfillment of the requirements for the degree of Doctor of Philosophy in the Department of Mechanical Engineering and Materials Science
in the Graduate School of Duke University
2014

Abstract

The focus of this dissertation is on the dynamics of electromagnetic systems for energy harvesting and filtering applications. The inclusion of magnets into systems generates nonlinearity due to the nature of electromagnetic interactions. In this work, magnetic nonlinearity manifests in tip interactions for cantilever beams, coupling effects for electromagnetic transduction, and bistable potential wells for a two beam system. These electromagnetic interactions are used to add non-contact coupling effects for the creation of bistable oscillators or arrays of coupled beams for energy filtering.

Nonlinearity at the tip of cantilever beams acts to change the dynamic and static behavior of the system. In this dissertation, these interactions are analyzed both with and without the nonlinear tip interactions. A linear analysis of the system without the tip interaction first provides insight into the shifting frequencies of the first four natural oscillation modes when considering a rigid body tip mass with rotational inertia and a center of mass that is offset from the tip of the beam. Then, the characterization of the nonlinearities in the beam stiffness and magnetic interaction provide insight into the static and dynamic behavior of the beam. The analytical and numerical investigations, using Rayleigh-Ritz methods and an assumed static deflection, are shown to be consistent with experimental tests. These methods provide a framework for theoretically establishing nonlinear static modes and small-amplitude linear modes that are consistent with physical behavior.

In electromagnetic coupling, the role of nonlinearity can have a detrimental or beneficial effect on energy harvesting. This work includes an investigation of the response of an energy harvester that uses electromagnetic induction to convert ambient vibration into electrical energy. The system's response behavior with linear coupling or a physically motivated form of nonlinear coupling is compared with single and multi-frequency base excitation. This analysis is performed with combined theoretical and numerical studies.

The ability of magnets to add nonlinearity to a system allows for the expansion of the phenomenological behavior of said system and potential advantages and disadvantages for energy harvesting. This work studies a two beam system made up of carbon fiber cantilever beams and attached magnetic tip masses with a focus on energy harvesting potential. Numerical and experimental investigations reveal an array of phenomena from static bifurcations, chaotic oscillations, and sub-harmonic orbits. These features are used to highlight the harvesting prospects for a similarly coupled system.

Beyond nonlinearity, the non-contacting coupling effects of magnets allow for the hypothetical creation of energy filtering systems. In this work, the band structure of a two dimensional lattice of oscillating beams with magnetic tip masses is explored. The focus of the wave propagation analysis is primarily on regions in the band structure where propagation does not occur for the infinite construction of the system. These band gaps are created in this system of 2 x 2 repeating unit cells by periodically varying the mass properties and, for certain configurations, the frequency band gaps manifest in different size and band location. Uncertainty in these regions is analyzed using potential variations associated with specific physical parameters in order to elucidate their influence on the band gap regions. Boundary effects and damping are also investigated for a finite-dimensional array, revealing an erosion of band gaps that could limit the expected functionality.

Dedicated to my wife and best friend, Julie

Contents

List of Tables

List of Figures

Acknowledgements

A huge thanks goes to Professor Brian Mann for his support, assistance, and guidance. His time and commitment to his students from undergraduates to doctoral candidates is admirable and a model for advisor-student relationships. Other professors I would like to thank for their insight and assistance along the way are Professors Thomas Witelski, Henri Gavin, Robert Kielb, and Lawrence Virgin.

I would also like to thank several colleagues (former and current) for their help and collaborative contributions: Dr. Genevieve Lipp, Dr. Clark McGehee, Dr. Sam Stanton, Dr. Brian Bernard, Dr. Firas Khasawneh, Dr. Zach Ballard, Dr. Simo Sah, Michael Mazzoleni, and Jake Greenstein. The assistance of many of these people goes well beyond what they were called to do with their own research and school work, from late night sanity talks to marathon movie sessions.

My wife Julie joined me on this journey halfway to the finish line, but has been my biggest cheerleader ever since. She is my best friend and even in the midst of her own job changes, the planning of our wedding, and an impending move, she has been a supportive constant by my side, helping me maintain perspective in all of this.

Last, I want to thank my parents for their emotional and academic support over the years. From reading to me as a child to helping me through my university years, their hope and love for me has been a powerful force in my academic career.

1

Introduction

The goal of this doctoral work is to explore the dynamics of systems with nonlinear, magnetic interactions within the framework of energy harvesting and filtering. In this work, nonlinearity is used as a tool to expand the phenomenological behaviors of the systems and expand on the predictable linear behavior patterns of common systems. In the course of this exploration, several problems associated with these systems were explored.

In vibration energy harvesting, mechanical excitation sources are translated into usable electricity. These sources vary from ocean and ground surface waves to vehicle and bridge motion to human walking [1–5]. Traditionally, harvesting systems are designed as linear harvesters, with the system resonance tuned to that of the dominant frequency of the environment [6–11] and transduction from physical vibration energy to electrical energy by means of electromagnetic [12–14] or piezoelectric [15–17] systems . This strategy is efficient in single frequency excitation environments, however for multi-frequency, time-varying, stochastic, and other more diverse environments, much of the energy remains untapped by these tuned linear harvesters [18–23] . It is these environments that call for more complex systems to more efficiently and

consistently harvest energy [18].

For energy filtering systems, research is primarily centered on systems that filter light or acoustic waves. These photonic [24–28] and phononic [29–34] systems, respectively, are designed with characteristics such that energy in the form of waves can only pass through the system in certain directions and at particular frequencies. This is done by periodically varying properties, either by use of different materials or specific construction to select frequency regions known as band gaps where the band structure of the wave propagation does not exist [35]. The variation for photonic and phononic systems is often designed on a microscale for frequency bands in the kHz or greater range [24–34]. The potential, however, exists for utilization of elastic systems and macro-scale organization for filtering at lower frequencies [36, 37].

For the explorations of energy harvesting and filtering systems described in this dissertation, analysis is done by way of mathematical modeling and approximation of physical systems made up primarily of elastic beams and nonlinear magnets. The following two sections lay out the modeling framework used as the basis for this work and the magnetic interactions that are featured.

1.1 Modeling framework

Variational calculus methods are the modeling basis for the majority of the analysis in this thesis. A fundamental example of this method in calculus of variations is the minimization of a functional

$$J(\vec{q}(t)) = \int_a^b L\left(\vec{q}(t), \dot{\vec{q}}(t), t\right)\, dt \tag{1.1}$$

for the shortest trajectory $\vec{q}^*(t)$ found at the stationary points of the functional. By finding the first variation of J and equating to zero, the functional can be minimized. This example is a form of Hamilton's principle of natural systems. Systems seek the

shortest or minimally resistive path. By expansion to typical dynamic systems with kinetic and potential energy, Euler-Lagrange equations are used to find the governing equations of motion for an ideal trajectory of least resistance

$$\frac{d}{dt}\left(\frac{\partial \mathcal{L}}{\partial \dot{q}_n}\right) - \frac{\partial \mathcal{L}}{\partial q_n} = 0\,, \tag{1.2}$$

where $\mathcal{L}$ is the Lagrangian of the system and q_n is a generalized coordinate used to describe a degree of freedom of the system. This equation constitutes a necessary condition for a local minimum and is similar to finding the root of the first derivative in differential calculus [38]. The number of generalized coordinates q_n is equal to the number of equations generated by Euler-Lagrange. Applications of Hamilton's principle of variation in certain configurations (such as beam mechanics) yield boundary conditions that fully define the resulting equations. An extension of Hamilton's principle includes expressions accounting for nonconservative forces such as viscous damping or external forcing. More detailed explorations of variational calculus and expansions on Hamilton and Euler-Lagrange are found in Refs. [38, 39].

1.2 Magnet modeling

The systems analyzed in this thesis often include magnets, interacting either with other magnets or conductive material, such as a wire coil. The dipole point source model is used exclusively for the derivation of the magnetic interactions in all systems (see derivation in Refs. [40, 41]).

For a point source dipole, as shown in Fig. 1.1, the magnet is theorized to have infinitesimal volume and existence at a single point. The B-field, also known as magnetic flux density or magnetic field in free space, at a point from the magnet source is expressed as

$$\vec{B}_{p/s} = -\frac{\mu_0}{4\pi}\nabla\frac{\vec{m}_s \cdot \vec{r}_{p/s}}{|\vec{r}_{p/s}|^3}, \tag{1.3}$$

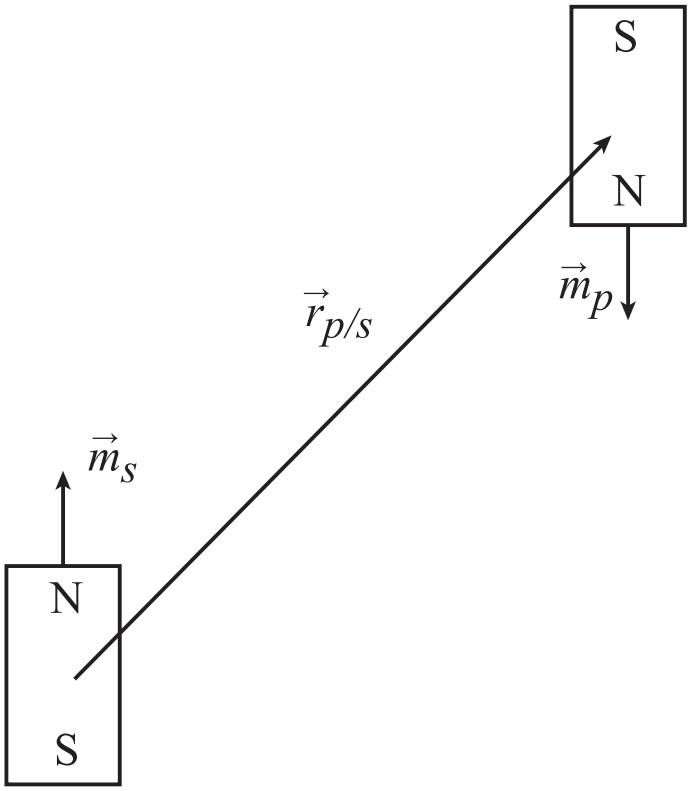

FIGURE 1.1: Schematic illustration of vectors used in the dipole approximation for the interactions between two magnets.

where $\mu_0 = 4\pi \times 10^{-7}$ H/m is the permeability, or magnetic constant, of free space, $\vec{\nabla}$ represents a vector gradient operation, and $\vec{r}_{p/s}$ is a vector from the source magnetic dipole to a given point. The magnetic moment of the source magnet can be expressed by

$$\vec{m}_s = \vec{M}_s v_s \,, \tag{1.4}$$

where v_s is volume of the source magnet and $\vec{M}$ is the magnetization vector. The amplitude of this magnetization vector is

$$\left|\vec{M}_s\right| = \frac{B_r}{\mu_0} \,, \tag{1.5}$$

where B_r is the residual magnetic flux density. This B-field indicates the amplitude and direction of the magnetic field flux at that point generated by the source.

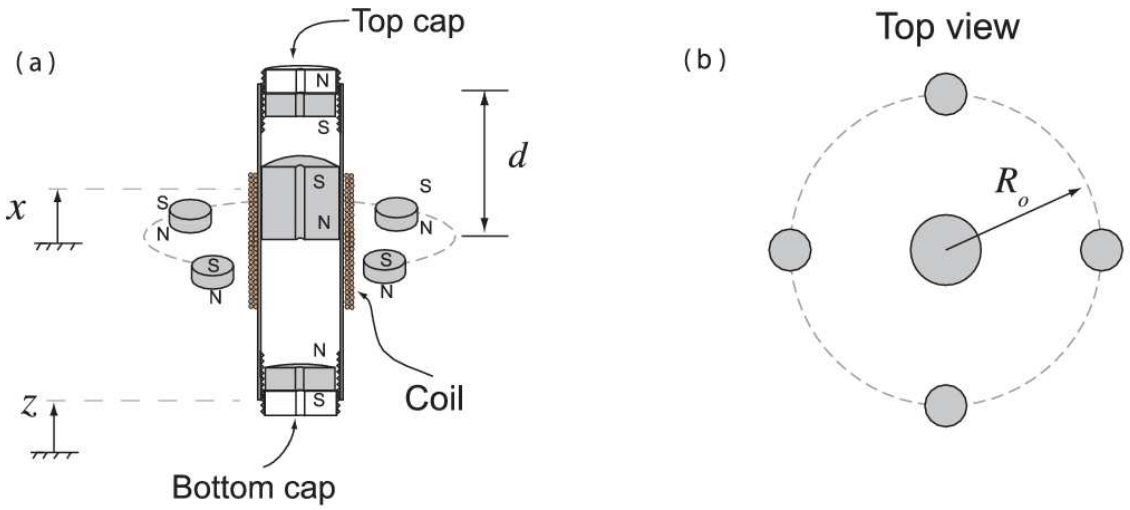

FIGURE 1.2: Schematic illustration of the nonlinear magnet system from Ref. [13] with 3-dimensional view in (a) and top view in (b).

The addition of a second magnetic dipole having moment $\vec{m}_p$ creates a potential energy between the two magnets. This interaction manifests itself in the form of a torque and force on the magnets. The potential energy of this interaction is

$$U_{p/s} = -\vec{m}_p \cdot \vec{B}, \tag{1.6}$$

where $\vec{m}_p$ is the magnetic moment of the magnet at some point from the source. From this energy expression, the interaction force between the magnets is derived by taking the negative of the gradient of Eq. 1.6. Additionally, the torque is found from

$$\vec{\tau}_{p/s} = -\vec{m}_p \times \vec{B}_{p/s} \tag{1.7}$$

where $\vec{\tau}_{p/s}$ is the torque generated by the source on the point.

One example of these interactions is found in Ref. [13]. This nonlinear system is made up of a center magnet on a fixed axis with a magnet on either end and a ring of magnets about the center of the system. A diagram of this configuration is found in Fig. 1.2. From the dimensions of the system and utilizing Eqs. 1.3-1.6, the

potential energy expression for this system becomes

$$U(y) = \frac{B_{r,c}v_c}{2\pi}\left[v_t B_{r,t}\left(\frac{1}{(d+y)^3}+\frac{1}{(d-y)^3}\right)-\frac{B_{r,o}v_o N}{2}\left(\frac{y^2}{(y^2+R_o^2)^{5/2}}-\frac{1}{(y^2+R_o^2)^{3/2}}\right)\right], \tag{1.8}$$

where v_c, v_o, and v_t are the volumes of the center magnet, the individual outer ring magnets, and the two magnets at the top and bottom of the system, respectively and $B_{r,c}$, $B_{r,o}$, and $B_{r,t}$ are the residual magnetic flux densities of the respective magnets. Also note that $y = x - z$ is the position of the center magnet with respect to the housing of the system, while d represents the spacing between the top, or bottom, magnet and the device center. R_o is the radial distance from the outer magnets to the central axis along which the center magnet moves and $N = 4$ is the number of evenly spaced outer magnets in the system. In the case of this system, the torque effects were ignored as constant vertical alignment was assumed. To obtain an expression for the restoring force of the system, the derivative with respect to the relative parameter y is taken to yield

$$F_m(y) = \frac{B_{r_c}v_c}{2\pi}\left[\frac{B_{r_o}v_o N}{2}\left(\frac{5y}{(y^2+R_o^2)^{5/2}}-\frac{5y^3}{(y^2+R_o^2)^{7/2}}\right)\right.$$
$$\left.-v_t B_{r_t}\left(\frac{3}{(d-y)^4}-\frac{3}{(d+y)^4}\right)\right]. \tag{1.9}$$

for the force on the center, movable magnet. This complex expression has three fixed points, one unstable and two stable, making this system bistable.

This example illustrates the highly nonlinear interactions of magnets. This fact is a theme through the dissertation as it introduces a layer of complexity in the systems of interest.

1.3 Research contributions

This doctoral work has four main contributions. The first is a method for analyzing the mode shapes of cantilever beams with considerable nonlinear tip interactions [42]. This analysis takes into account nonlinear beam effects as the result of large amplitude deflections. By assuming the large amplitude deflections are primarily static and oscillations occur as small scale perturbations, this work studies the dynamic behavior of this system. Using Rayleigh-Ritz methods and assuming a static deflection, the analytical and numerical investigations are shown to be consistent with experimental tests. This theoretical framework is important in that it provides a blueprint for theoretically establishing nonlinear static modes and small-amplitude linear modes that are consistent with physical system behaviors.

The second contribution provides a comparative study for the effects of nonlinear electromagnetic coupling in an otherwise linear harvester [43]. This study highlights the positional dependence of the coupling effects and illustrates the changing bandwidth considerations for diverse multifrequency excitation environments. The principles examined are applicable to nonlinear mechanical systems with electromagnetic coupling and show promise for increasing the energy harvested from some environments.

The third contribution is a study of a two beam bistable system from an energy harvesting perspective [44]. The two beam system is modeled with large deflection nonlinear effects taken into consideration. Numerical and experimental studies unveil a diverse set of behavior with qualitative and quantitative considerations for vibrational energy harvesting.

The final contribution is an exploration of a hypothetical two dimensional lattice of oscillating beams with magnetic tip masses [45]. This system is explored first as an infinite array of repeating N x N unit cells. By varying the mass configuration in

a simple 2 x 2 cell, the band structure of the resulting wave propagation is analyzed for the existence of frequency gaps with no propagating waves. The effects of uncertainty are then explored using Monte Carlo simulations and assumed probabilistic uncertainty in the mass and magnetization properties. The effects of boundary conditions associated with a finite manifestation of the array system are analyzed as are the effects of physical damping for periodically excited arrays of various sizes.

1.4 Thesis organization

This dissertation proposal is organized as follows: In Chapter 2, energy harvesting systems with four classes of restoring forces are analytically analyzed using harmonic balance with a focus on power bandwidth and coexisting solutions. The restoring force classes are: linear, softening, hardening, and bistable. Chapter 3 explores the effects of highly nonlinear boundary interactions on beam dynamics for a cantilever beam with nonlinear stiffness properties. The analysis is performed using the approximations of admissible functions and Rayleigh-Ritz energy methods. Chapter 4 investigates the response of an energy harvester that uses electromagnetic induction to convert ambient vibration into electrical energy, comparing the system's response behavior when either a linear or a physically motivated form of nonlinear coupling is applied. In Chapter 5, a two beam, magnetically coupled bistable oscillator system is investigated from the perspective of its integration into an energy harvester. Numerical and experimental investigations are performed. Chapter 6 explores the band structure of a two dimensional lattice of oscillating beams with magnetic tip masses. Analysis of the band structure is primarily focused where wave propagation does not occur, with these band gaps explored for infinite lattice configurations, parametric uncertainty effects on band gap sizes and locations, and the detriment of finite lattice considerations on the gaps. Chapter 7 provides a brief summary and conclusions of the doctoral work, as well as proposed future work that branches from the existing

studies.

2

Linear and nonlinear energy harvesting

In the field of vibration energy harvesting, research has shifted focus from linear systems [1, 10] with or without tuning capabilities to nonlinear systems with widened usable bandwidth, multiple attractors, and chaotic oscillations [9, 13, 16, 17, 46]. This chapter seeks to model and analyze both classes of systems, comparing linear harvester behavior with nonlinear behavior. Specifically, a simple single degree of freedom system with electrical coupling to a basic harvesting circuit is analyzed. This single degree of freedom is given one of four potential energy signatures: linear, softening, hardening, and bistable. Using harmonic balance, periodic solutions at the excitation frequency are approximated, as is the electrical power of these solutions.

The chapter is organized as follows. The next section derives the general, dimensionless energy harvesting model from system energies and nonconservative forces. Section 2.2 then uses harmonic balance of assumed periodic oscillations to develop frequency and amplitude response curves for different parameter sets. Conclusions are in the final section.

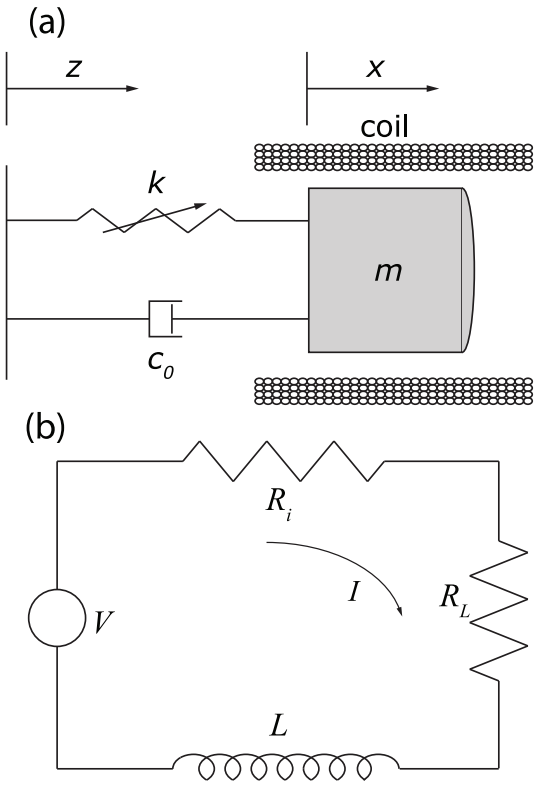

FIGURE 2.1: Diagrams of an electromagnetic induction based energy harvester (a) and corresponding electrical circuit (b).

2.1 Energy harvester model

This section derives dimensionless equations for the energy harvesting systems in question from kinetic and potential energies and noncoservative forces. For these systems, energy conversion is done by electromagnetic induction with constant coupling [47] as shown in Fig. 2.1.

2.1.1 Energy expressions

The kinetic energy of the single degree of freedom electromechanical system is expressed as

$$\mathcal{T} = \frac{1}{2}m\dot{x}^2 + \frac{1}{2}L\dot{q}^2 + \tilde{\Theta}\dot{q}y\,, \tag{2.1}$$

where $\dot{x}$ is the velocity of the mass m, L is the inductance, q is a charge coordinate, $y = x - z$ is the relative velocity between mass and base, and $\tilde{\Theta}$ is the coupling coefficient of the electromechanical transducer. The nonconservative, dissipative energy of the system is

$$\mathcal{D} = \frac{1}{2} c_d \dot{y}^2 + \frac{1}{2} \left(R_L + R_i \right) \dot{q}^2 \tag{2.2}$$

where c_d is a constant used to describe the viscous mechanical damping, R_i is the internal resistance of the coil, and R_L is the resistance of the external load. The potential energy of the system can be described by the integral

$$\mathcal{U} = -\int_0^y \chi(y)\, dy\,, \tag{2.3}$$

of the restoring force $\chi(y)$. This restoring force will take different forms to be examined later for the the four linear and nonlinear cases.

2.1.2 Equations of motion

Choosing q as a generalized coordinate for the electrical system and applying Lagrange's equation gives the governing electrical equation

$$L\ddot{q} + \dot{q}\left(R_L + R_i \right) + \tilde{\Theta}\dot{y} = 0\,. \tag{2.4}$$

Likewise, choosing y as a generalized coordinate and substituting $x = y + z$ into Eq. 2.1 gives the governing equation for the mechanical system

$$m\ddot{y} + c_d\dot{y} - \chi(y) - \dot{q}\,\tilde{\Theta} = -m\ddot{z}\,, \tag{2.5}$$

after applying Lagrange's equation.

The potential energy and restoring force signatures for the four cases are found in Fig. 2.2. The restoring forces can be written as a cubic polynomial $\chi(y) = \pm ky \pm k_3 y^3$, where sign changes in front of k and k_3 are changed to form each restoring force case.

To generalize the analytical study, Eqs. 2.4 and 2.5 are made dimensionless but substituting $\omega_l = \sqrt{k_l/m}$, $\tau = \omega_l t$, $y = \hat{y}\ell$, $z = \hat{z}\ell$, and $\dot{q} = i_m I$, where τ is dimensionless time, i_m is a convenient reference current, and ℓ is a convenient physical dimension. Excitation for the mechanical system, will take the form $\ddot{z} = -A\sin\Omega t$, where Ω represents the excitation frequency and A the acceleration amplitude. For convenience, the dimensionless terms drop the ($\hat{}$). The electrical equation now becomes the dimensionless equation

$$I' + \rho I + \theta y' = 0\,, \tag{2.6}$$

where a ($'$) denotes a derivative with respect to dimensionless time and the dimensionless constants,

$$\rho = \frac{R_L + R_i}{\omega_l L} \quad \text{and} \quad \theta = \frac{\ell}{i_m L}\hat{\Theta}\,, \tag{2.7}$$

are defined in terms of the original physical parameters. The dimensionless mechanical equation becomes

$$y'' + \mu y' + \alpha y + \beta y^3 - \epsilon\theta I = \Gamma\sin\eta\tau\,, \tag{2.8}$$

where dimensionless system constants

$$\mu = \frac{c_o}{m\omega_l}\,,\ \alpha = \frac{k_l}{k_m}\,,\ \beta = \frac{k_3 l^2}{k_l}\,,\ \epsilon = \frac{L}{m}\left(\frac{i_m}{\omega_l \ell}\right)^2 = \frac{L}{k_l}\left(\frac{i_m}{\ell}\right)^2\,,\ \Gamma = \frac{A}{\ell\omega_l^2}\,,\ \eta = \frac{\Omega}{\omega_l}\,. \tag{2.9}$$

2.2 Harmonic balance analysis

This section derives the responses of the mechanical and electrical systems for average power harvesting comparisons. An expression for this power is derived by integrating the dimensionless form of the instantaneous power $P = \rho I^2$ over the period of the excitation

$$P_a = \frac{1}{T}\int_0^T \rho I^2\, dt\,, \tag{2.10}$$

where $T = 2\pi/\eta$ is the period of the excitation source and an ideal transducer with zero internal resistance is presumed.

2.2.1 Frequency response for hardening, softening, and linear harvester cases

In this section, the frequency response for the hardening, softening, and linear restoring force cases are derived. For these cases, the dimensionless mechanical equation is

$$y'' + \mu y' + \alpha y + \beta y^3 - \epsilon\theta I = \Gamma \sin \eta\tau \,, \tag{2.11}$$

where the value of β determines which case is used. For the linear case, $\beta = 0$, for the hardening system $\beta > 0$, and for the softening system $\beta < 0$. Solutions to the mechanical and electrical system are assumed to take the form of a truncated Fourier series with slowly varying coefficients

$$y = a(\tau)\cos\eta\tau + b(\tau)\sin\eta\tau \tag{2.12}$$

$$I = c(\tau)\cos\eta\tau + d(\tau)\sin\eta\tau \,, \tag{2.13}$$

with time derivatives

$$y' = \Big(a' + b\eta\Big)\cos\eta\tau + \Big(b' - a\eta\Big)\sin\eta\tau \,, \tag{2.14}$$

$$I' = \Big(c' + d\eta\Big)\cos\eta\tau + \Big(d' - c\eta\Big)\sin\eta\tau \,, \tag{2.15}$$

$$y'' = \Big(2b' - a\eta\Big)\eta\cos\eta\tau - \Big(b\eta + 2a'\Big)\eta\sin\eta\tau \,, \tag{2.16}$$

where $a'' = b'' = 0$, accordingly with the slowly varying assumption. The expressions for y, y', y'', I, and I' are then substituted back into Eqs. 2.6 and Eq. 2.11 and the

coefficients of $\cos\eta\tau$ and $\sin\eta\tau$ are balanced on each side of the equation to obtain

$$c' + \theta a' = -\rho c - \eta d - \theta\eta b\,, \tag{2.17}$$

$$d' + \theta b' = -\rho d + \eta c + \theta\eta a\,, \tag{2.18}$$

$$\mu a' + 2\eta b' = a\left(\eta^2 - \alpha - \beta\frac{3}{4}r^2\right) - \mu\eta b + \epsilon\theta c\,, \tag{2.19}$$

$$-2\eta a' + \mu b' = b\left(\eta^2 - \alpha - \beta\frac{3}{4}r^2\right) + \mu\eta a + \epsilon\theta d + \Gamma\,, \tag{2.20}$$

where $r^2 = a^2 + b^2$. The steady-state amplitude of the periodic response is obtained from the fixed points of Eqs. 2.17–2.20. This steady-state assumptions requires $a' = b' = c' = d' = 0$. After zeroing these terms, the coefficients for the assumed solution of the electrical equation are written in terms of the displacement coefficients

$$c^* = -\frac{\theta\eta}{\rho^2+\eta^2}(\eta a^* + \rho b^*) \qquad \text{and} \qquad d^* = \frac{\theta\eta}{\rho^2+\eta^2}(\rho a^* - \eta b^*) \tag{2.21}$$

where a (*) is used to represent the fixed point solutions. The expressions for c^* and d^* are then substituted into Eqs. 2.19 and 2.20 for c and d, respectively, along with $a' = b' = 0$. This gives the expressions

$$\left(\left(\frac{\epsilon\theta^2}{\rho^2+\eta^2} - 1\right)\eta^2 + \alpha + \frac{3}{4}\beta r^{*2}\right)a^* + \left(\mu + \frac{\epsilon\theta^2\rho}{\rho^2+\eta^2}\right)\eta b^* = 0\,, \tag{2.22}$$

$$\left(\left(\frac{\epsilon\theta^2}{\rho^2+\eta^2} - 1\right)\eta^2 + \alpha + \frac{3}{4}\beta r^{*2}\right)b^* - \left(\mu + \frac{\epsilon\theta^2\rho}{\rho^2+\eta^2}\right)\eta a^* = \Gamma\,, \tag{2.23}$$

The final expression for the frequency response of these cases is found by squaring and adding Eqs 2.22 and 2.23,

$$\left[\left(\frac{\epsilon\theta^2}{\rho^2+\eta^2} - 1\right)\eta^2 + \alpha + \frac{3}{4}\beta r^{*2}\right]^2 r^{*2} + \left[\mu + \frac{\epsilon\theta^2\rho}{\rho^2+\eta^2}\right]^2 \eta^2 r^{*2} = \Gamma^2\,. \tag{2.24}$$

The response of a linear harvester is found by setting β to zero and solving for r,

$$r^* = \frac{\Gamma}{\sqrt{\left(\alpha + \left(\frac{\epsilon\theta^2}{\rho^2+\eta^2} - 1\right)\eta^2\right)^2 + \left(\mu\eta + \frac{\epsilon\theta^2\rho\eta}{\rho^2+\eta^2}\right)^2}}\,. \tag{2.25}$$

From the mechanical response, a natural and illustrative extension is an expression for the electrical power. This is found by first squaring and adding the expressions for c^* and d^* in Eq. 2.21 to get the steady-state current amplitude

$$r_e^{*2} = \sqrt{\tilde{c}^2 + \tilde{d}^2} = \frac{\theta^2 \eta^2}{\rho^2 + \eta^2} r^{*2} \tag{2.26}$$

By substituting this expression into Eq. 2.10, the average power is found in terms of the mechanical response amplitude

$$P_a = \frac{1}{2} \rho r_e^{*2} = \frac{1}{2} \frac{\rho \theta^2 \eta^2}{\rho^2 + \eta^2} r^{*2} \,. \tag{2.27}$$

By first finding the roots of Eq. 2.24 to solve for the mechanical response of the linear, softening, or hardening system, the power can be found by inserting that computed value into Eq. 2.27. Likewise, mechanical solutions of the bistable system can be inserted to find the average power.

2.2.2 Bistable harvester analysis

This subsection solves for the frequency response of the bistable system which is described by the mechanical equation

$$y'' + \mu y' - y + \beta y^3 - \epsilon \theta I = \Gamma \sin \eta \tau \,. \tag{2.28}$$

Here β acts as a tuning constant for the nonlinearity of the system. To solve for the mechanical responses of the bistable system, it is instrumental to note that the system has two stable equilibria. When $\beta > 0$ (as is required for bistable system) these stable equilibria are

$$y_{st} = \pm \sqrt{\frac{1}{\beta}} \,. \tag{2.29}$$

Approximate analytical solutions for the bistable system can be found in much the same was as the previous section. However, the first term in the Fourier series $p(\tau)$

is included

$$y = p(\tau) + a(\tau)\cos\eta\tau + b(\tau)\sin\eta\tau\,, \tag{2.30}$$

with first and second derivates

$$y' = p' + \Big(a' + b\eta\Big)\cos\eta\tau + \Big(b' - a\eta\Big)\sin\eta\tau\,, \tag{2.31}$$

$$y'' = \Big(2b' - a\eta\Big)\eta\cos\eta\tau - \Big(b\eta + 2a'\Big)\eta\sin\eta\tau\,, \tag{2.32}$$

where accelerations are ignored, e.g. $a'' = b'' = p'' = 0$, as consistent with the slowly varying approximation. The Fourier series expressions and their derivatives are then inserted into Eqs. 2.28 and 2.6. Balancing cosine, sine, and offset terms gives

$$\mu p' = p\left[1 - \beta\left(p^2 + \frac{3}{2}r^2\right)\right], \tag{2.33}$$

for the offset term and

$$\mu a' + 2\eta b' = a\left(\eta^2 + 1 - 3\beta p^2 - \frac{3}{4}\beta r^2\right) - \mu\eta b + \epsilon\theta c\,, \tag{2.34}$$

$$-2\eta a' + \mu b' = b\left(\eta^2 + 1 - 3\beta p^2 - \frac{3}{4}\beta r^2\right) + \mu\eta a + \epsilon\theta d + \Gamma\,, \tag{2.35}$$

for the periodic terms in the mechanical equation. Electrical balancing from Eqs. 2.17 and 2.18 is the same for the bistable system.

To derive the steady-state response of the system, all time varying coefficients are set to zero such that $a' = b' = p' = c' = d' = 0$. The expressions for c^* and c^* are then returned to Eqs. 2.34 and 2.35 for c and d to obtain

$$\left(\left(1 - \frac{\epsilon\theta^2}{\rho^2 + \eta^2}\right)\eta^2 + 1 - 3\beta p^{*2} - \frac{3}{4}\beta r^{*2}\right)a^* - \left(\mu + \frac{\epsilon\theta^2\rho}{\rho^2 + \eta^2}\right)\eta b^* = 0\,, \tag{2.36}$$

$$\left(\left(1 - \frac{\epsilon\theta^2}{\rho^2 + \eta^2}\right)\eta^2 + 1 - 3\beta p^{*2} - \frac{3}{4}\beta r^{*2}\right)b^* + \left(\mu + \frac{\epsilon\theta^2\rho}{\rho^2 + \eta^2}\right)\eta a^* = -\Gamma\,. \tag{2.37}$$

Again, squaring and adding these two equations gives an expression for response of the mechanical system

$$\left[\left(1-\frac{\epsilon\theta^2}{\rho^2+\eta^2}\right)\eta^2+1-3\beta p^{*2}-\frac{3}{4}\beta r^{*2}\right]^2 r^{*2}+\left[\mu+\frac{\epsilon\theta^2\rho}{\rho^2+\eta^2}\right]^2\eta^2 r^{*2}=\Gamma^2\,. \quad (2.38)$$

Note that p^* has varying values. By setting $p'=0$ in Eq. 2.33 and solving for the steady-state solution, the steady state offset terms are found

$$p^*=0 \text{ and } p^*=\pm\sqrt{\frac{1}{\beta}-\frac{3}{2}r^{*2}}\,. \quad (2.39)$$

Physical solutions are restricted by the second expression to $r^{*2}\leqslant\frac{2}{3\beta}$. The average power is then found by inserting the r^* expression into Eq. 2.27.

2.3 Response results comparison

This section compares the amplitude and power responses of the four restoring force cases. Fig. 2.3 shows the amplitude (a, d, g, j) and electrical power (b, e, h, k) response as a function of frequency and the electrical power (c, f, i, l) as a function of excitation amplitude. Stable periodic orbits are shown in blue and unstable orbits in red.

The linear case is shown in subplots a-c. The amplitude and power frequency responses show peak values near the natural frequency $\eta=1$. The power shows scaling with the square of the excitation amplitude Γ as expected for a linear system.

The softening system is shown in subplots d-f. For softening systems, the resonant amplitude peak bends to the left at an excitation frequency lower than the natural frequency of the linear system. The softening system also shows coexisting solutions with the peak values coexisting with small amplitude values. The power bandwidth of this system shows an improvement over the narrow peaked linear system. The power vs. excitation amplitude figure illustrates the nonlinear relationship that is not

present in the linear system. Likewise, in this case, coexisting solutions are present for lower amplitudes, while at higher amplitudes a single high energy solution is present.

The hardening case in subplots g-i shows similar behavior to the softening case. Instead of bending to the left however, the response peak bends to the right, greater than the linear system natural frequency. The power response is favorable over the softening case because this right bend indicates peaks at higher frequencies, meaning higher response velocities and higher coupling forcing to the electrical system. Like the softening case, this higher power output has a larger bandwidth than the linear system.

The final and most behaviorally rich case is that of the bistable case in subplots j-l. The bistable solution is uniquely multi-branched. One branch, the large amplitude solutions, shows oscillations about the center, indicating well mixing behavior. This solutions have a higher velocity and therefore a higher power. The other branch of solutions is lower amplitude and is for oscillations about either local potential well. The coexistence of three unique solutions for oscillations at the linear natural frequency $\eta = 1$ provides an opportunity for response control, allowing for solutions to lock into different oscillation levels. Also of note is the shape of the frequency response and power curves. The large orbit solutions show a shape similar to to the hardening oscillator, while the low orbits mirror the softening system. Examining the potential energies in Fig. 2.2 shows the local softening shape and global hardening shape of the bistable potential energy. The power vs. excitation amplitude subplot illustrates the coexistence of solutions for the different excitation levels. At low amplitudes, three solutions exist with different power levels while higher amplitudes lock into the high energy orbit.

2.4 Conclusions

This chapter modeled and analyzed via harmonic balance four classes of single degree of freedom energy harvester: linear, softening, hardening, and bistable. The approximate responses were used to generate electrical power responses for comparison. The linear solutions showed the predictable single peak near the natural frequency, while the nonlinear harvesters showed a more diverse response. These systems showed increased power bandwidth over the linear system and coexisting solutions. In the case of the bistable harvester, high amplitude well mixing behavior provided large amplitude solutions over a wide bandwidth at lower frequencies. While the linear harvester showed a far better response to excitation level increases, this is only the case near the natural frequency, where the system is at resonance. For off-resonance oscillations, the nonlinear systems have more potential for high level power generation. This showed that the nonlinear systems had the additional advantage of robustness to changes in the system.

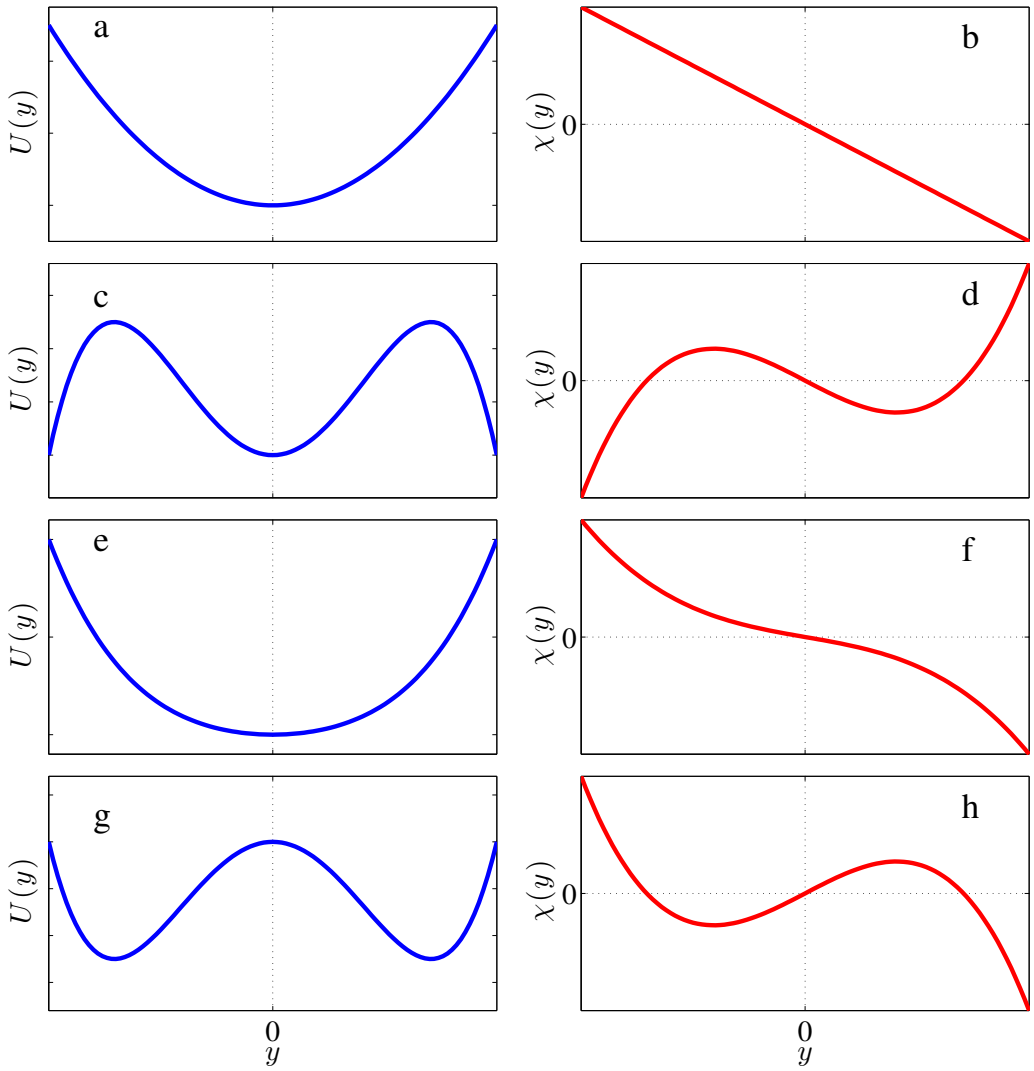

FIGURE 2.2: Potential energy (a,c,e,g) and restoring force (b,d,f,h) diagrams for the four cases presented in this chapter: linear (a,b), softening (c,d), hardening (e,f), and bistable (g,h).

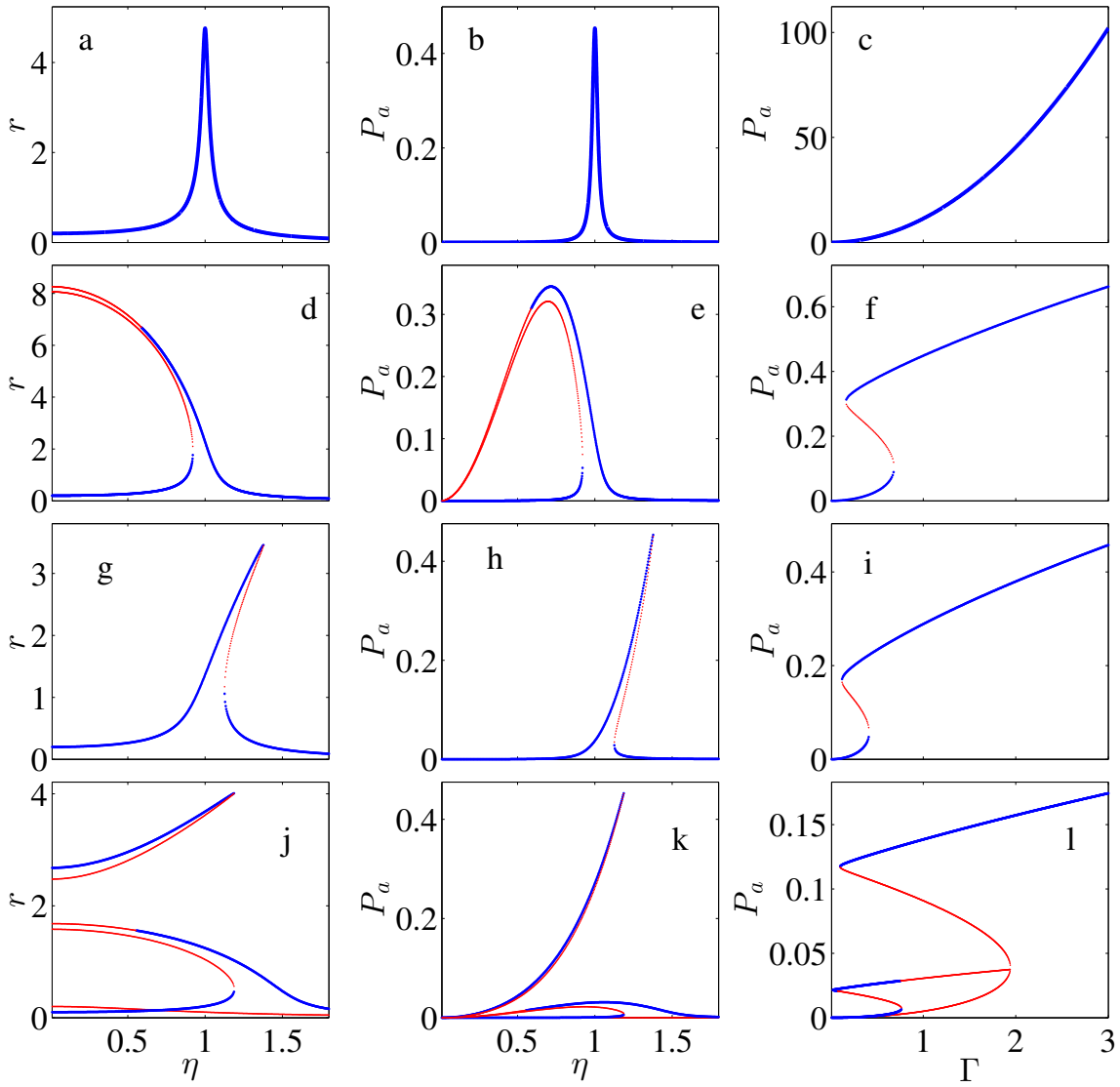

FIGURE 2.3: Plots showing the dimensionless mechanical response (a,d,g,j) and average power (b,e,h,k) versus frequency and the dimensionless average power versus excitation amplitude (c,f,i,l) for the four restoring force cases: linear (a,b,c), softening (d,e,f), hardening (g,h,i), and bistable (j,k,l). System parameters $\mu = 0.01$, $\epsilon = 0.8$, $\theta = 10$, and $\rho = 2500$ were used for all plots. For the softening, hardening, and bistable systems $\beta = -0.02$, 0.1, and 0.2. Frequency response plots used excitation amplitude $\Gamma = 0.2$ and power versus amplitude figures used $\eta = 1$, 0.8, 1.2, and 0.75 for linear, softening, hardening, and bistable cases (c,f,i,l), respectively.

3

Nonlinear tip interactions of a cantilever beam

A cantilever beam with unusual loading, either nonlinear or significant amplitude, large boundary excitation, or non-ideal geometry and properties often is mischaracterized by the assumptions of linear Euler-Bernouilli beam theory. In many cases, if the oscillations result in large amplitude deflections, the assumptions of linear theory may fail to capture the requisite behavior of the system oscillations [48]. Exact analytical expressions are sometimes still possible with given ideal assumptions, but often approximate, numerical, or derived analysis is used to find the deflection modes and resonant frequencies of a system.

Wang [49, 50] and Holden [51] separately looked at numerical solutions for a cantilever beam with finite, but moderate deflections, focusing on angular rotations along the beam. In another strategy, Denman and Schmidt used approximate methods with Chebyshev polynomials for nonlinear boundary conditions [52]. Timoshenko took an alternative approach to beam modeling by taking into account shear deformation and rotational inertia effects to help describe oscillations for beams of unique geometric and material properties [53]. Eisley looked at nonlinear deformations in plates and beams, including post-buckling oscillations [54]. Genin explored nonlin-

ear bending by way of nonlinear inertial terms [55]. Bisshopp and Drucker solved problems with elliptical integrals to find beams subjected to concentrated, vertical loading at one end [56]. Tada and Lee [57], and Hibbitt et al [58] used finite element analysis, with the former comparing results to analytical elliptical solutions. Luongo looked at torsional modes out of plane, utilizing Galerkin methods [59]. Relating to nonlinear boundary conditions, Turner explored the effects of Hertizian tip contacts [60]. In similar analysis, Crandall [61] looked at nonlinear quadratic damping effects.

The literature includes an expanse of modeling techniques to adjust linear models for nonlinear beam motion and boundary conditions. The beam energy modeling for this chapter are based on a couple of these techniques. Starting from the guiding principles of Euler-Bernoulli, curvature-based deflection models, the approximations of static and vibration solutions are improved by inclusion of nonlinear terms. At various points Da Silva et al. [62], Bathe and Bolourchi [63], and Nayfeh and Pai [64] developed nonlinear equations that capture more of the behavior for beams that undergo large deflections. The expansive work of Nayfeh and Pai [64] served as the analytical basis for examining the nonlinear expressions for the beam energies for a cantilever beam.

The physical system that provides the basis and motivation for this chapter is shown in Figure 3.1. The system is a cantilever beam with a tip magnet that is acted on by a fixed magnet. For particular configurations, this creates a bistable system and gives a static mode with non-zero deflection. This system has been explored for piezoelectric beams and others [16, 17, 65–68]. In Refs. [17, 65, 66], the systems are assumed to have a single mode that oscillates about zero static deflection with the bistability instead appearing in the ordinary differential equations for the mechanical system.

This chapter approaches this system differently by including static deflection modes along with the dynamic flexural modes. First, the nonlinear expressions for

the beam energies for a cantilever beam are derived primary from Ref. [64]. With the complexity of a significant nonlinear magnetic tip interaction, manifesting as both a tip force and torque, the nonlinear beam deflection analysis provides an approach to characterizing the interactions. Departing from the approaches of Refs. [17, 65, 66] which assume zero static deflection and single mode simplification, this chapter first considers a moderate size static deflection. This is done by confining the nonlinear analysis to weakly nonlinear static elastic energies of the beam stiffness and including the highly nonlinear magnetic boundary conditions. Using approximations and assumed solutions, the physical system response is modeled in the chapter on a functionally accurate analysis level. From the static deflections, a linear analysis for resonant modes about this new beam equilibrium provides further insight into the effects of nonlinear magnetic tip interactions and the dynamic response of a cantilevered beam. This alternative analysis provides detail beyond first mode models prominent in the literature.

In addition, this chapter details a comparative analysis for linear cases with a rigid body tip mass and no nonlinear magnetic tip interactions. Assuming simple linear beam energies, this analysis highlights the effects of including rotational inertia and accurate center of mass offsets. These considerations have significant impact on the natural frequencies and corresponding linear mode shapes of the beam for small oscillations. Compared to modeling the tip mass as a point, the rigid body tip mass approach provides a more complete analysis of the linear cantilever beam with attached mass at the free end.

The chapter is organized as a progression from model development to theoretical analysis to experimental demonstration. First, the nonlinear physical system that provides the chapter basis and experimental comparison is detailed in Section 3.1. Next, Section 3.2 details the system modeling, including derivations of the beam energies, nonlinear magnet interaction, simplification to dimensionless form, and the

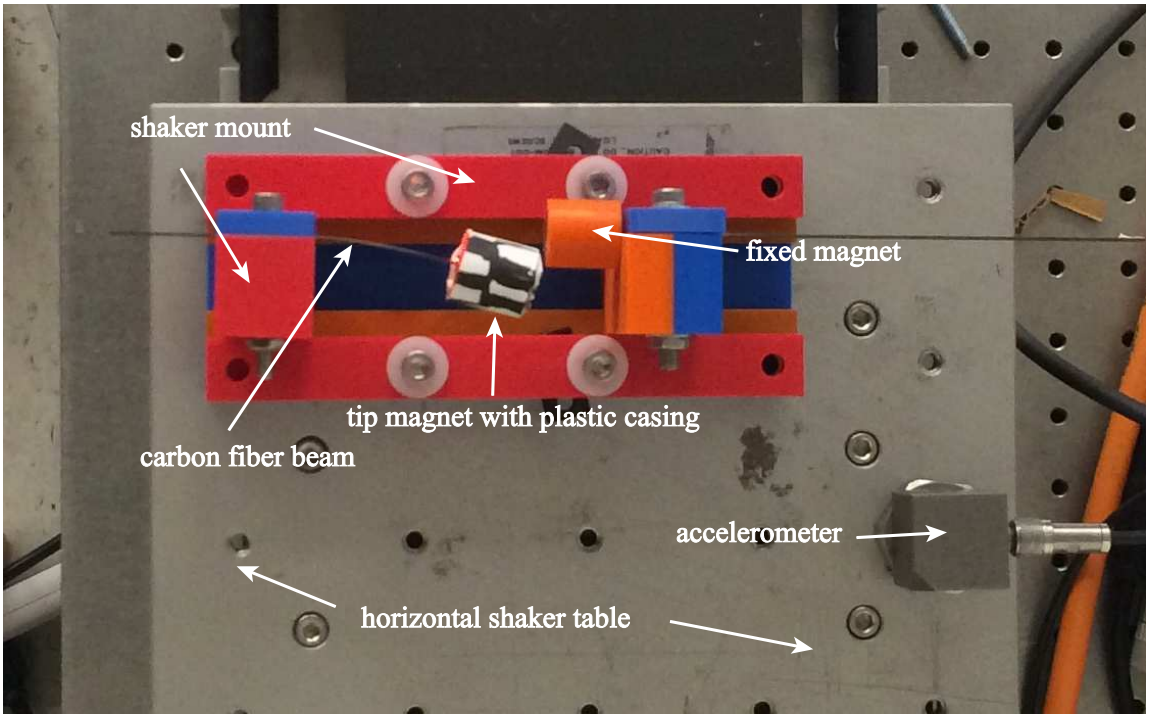

FIGURE 3.1: Experimental system with cantilevered beam, tip mass with magnet, and a fixed magnet that can slide along a guide track to adjust the magnet-magnet separation distance.

establishment of the equations of motion. Section 3.3 solves these equations to obtain the analytical mode shapes and natural frequencies for the linear cases and for the nonlinear magnetic tip interaction case, applies approximate techniques through Rayleigh-Ritz to determine static deflections and natural frequencies. Section 3.4 then characterizes the experimental system and compares the results with the dimensionless theoretical representations in the previous sections. Conclusions follow in the final section.

3.1 Experimental system description

An image of the experimental system is shown in Figure 3.1. The system is a cantilever beam with a tip magnet on the free end and a second magnet fixed some distance away. The beam is made from a carbon fiber strip (DragonPlate^{TM}) with a

parallel fiber alignment held by an epoxy matrix. The beam is clamped to the base at one end with a tip mass fixed to the other end. This mass setup can be seen in some detail in Figure 3.2d and is a neodymium magnet held in a small plastic casing. Also fixed in a small plastic casing and attached to the plastic mount is a second magnet, oriented such that it lies on the same axis as the beam and tip magnet, but has the opposite magnetization direction to generate a repulsion force and rotational torque on the tip magnet. The relevant parameters for the system are found in Table 3.1.

Static deflection measurements were obtained from image processing of digital images of the deflected beam. Dynamic measurements were performed by a Polytec scanning laser vibrometer.

3.2 System modeling

Figure 3.2 shows the beam configuration cases considered in this chapter. For each case, vibration is only considered in one flexural direction and the mode shapes and resonant frequencies are found either through exact analytical methods or approximate techniques. The appropriate expressions are developed from the fully complex case of the beam with a tip mass and nonlinear magnetic tip interactions before simplifying by removing appropriate terms for the comparison cases. Figure 3.2 a - c shows the progression from the simplest case, without a tip mass, to the beam with a tip mass, and then including the magnetic tip interaction. Figure 3.2d shows the relevant dimensions for the tip mass.

3.2.1 Energy derivations

This section derives the conservative energy expressions for all system components. For the case of a beam in bending in a single direction, the choice is taken to ignore

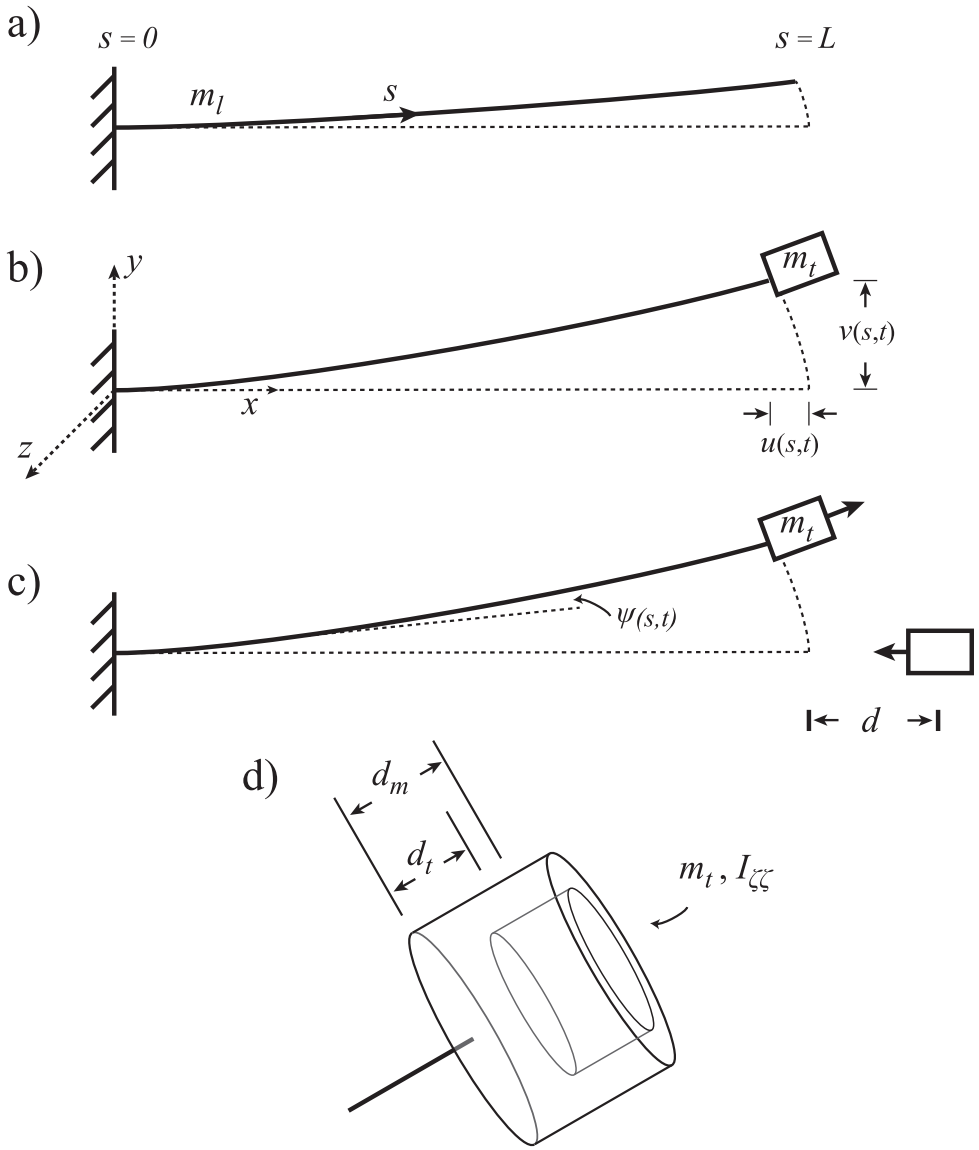

FIGURE 3.2: Three beam configurations: a) cantilever beam with linear density m_l, b) cantilever beam with tip mass m_t and mass moment of inertia $I_{\zeta\zeta}$, and c) cantilever beam with magnetic tip mass and a fixed magnet, and a detailed diagram d) of magnetic tip mass. Magnetic moment vectors are indicated by arrows on the masses, spatial deflection angle ψ is indicated, and the stationary magnet is $d + L$ from the origin at the beam base. The detailed magnetic diagram d) shows center of mass displacement from the beam tip d_t and magnet center displacement from the beam tip d_m.

rotational inertia effects, and pose the kinetic energy for a freely vibrating beam as

$$T_B = \frac{1}{2}\int_0^L m_l \left(\dot{u}^2 + \dot{v}^2\right) ds\,, \tag{3.1}$$

where s is the spatial coordinate along the beam, u and v are the vibration in the x and y directions respectively (see Fig. 3.2) and vary with time t and s, m_l is the density per unit length along the beam, L is the length of the beam, and an overdot $(\dot{})$ represents a time derivative. For the tip mass, significant rotational inertia is assumed and therefore the mass has rotational as well as translational kinetic energy. For the given system in Figure 3.2, the kinetic energy is

$$T_T = \frac{1}{2} m_t\, \dot{\vec{r}}_T \cdot \dot{\vec{r}}_T + \frac{1}{2} I_{\zeta\zeta}\, \dot{\psi}(L,t)^2\,, \tag{3.2}$$

where m_t is the tip mass, $\dot{\vec{r}}_T$ is the translation velocity vector for the mass, $I_{\zeta\zeta}$ is the mass moment of inertia for the mass at the tip of the beam, and $\dot{\psi}(L,t)$ is the angular velocity of the beam at the tip $s = L$. Figure 3.2c illustrates the representation of the beam angle ψ which varies spatially in s and in time t. The position vector for the tip mass is as follows

$$\vec{r}_T = \begin{bmatrix} L + d_t \cos\psi(L,t) + u(L,t) \\ v(L,t) + d_t \sin\psi(L,t) \\ 0 \end{bmatrix}, \tag{3.3}$$

where d_t is the distance from the tip to the center of mass of the tip mass as shown in Figure 3.2c. Taking the first time derivative of that expression and inserting into Eq. 3.2 gives a strongly nonlinear equation for the tip kinetic energy.

The potential energy for the system comes from the bending of the beam as well as the tip interactions. Bending in the beam has potential because of internal strain energy in the material, which is the result of stress-strain inducing curvature [69].

The expression for potential energy with this in mind becomes

$$V_B = \frac{1}{2}\int_0^L EI_\zeta \psi'^2 ds\,, \tag{3.4}$$

where E is the elastic modulus of the beam material, I_ζ is the second moment of inertia for the beam cross-section about the central axis of bending, and a prime symbol ($'$) indicates a partial derivative along the beam, $\frac{\partial}{\partial s}$. For the case of this system, the nonlinear magnetic tip interactions are in the form of magnetic interactions between two dipoles and are captured by a highly nonlinear potential energy field dependent on the displacement and rotation of the beam tip, $U_M\left(\psi(L), u(L), v(L)\right)$. The development of this equation is discussed in detail in Section 3.2.2.

In order to simplify the energy expressions from their fully nonlinear form, it is necessary to make some assumptions about the nature of the beam and its expected deflections. For the purposes of this analysis, up to third order nonlinearity for beam bending angles are considered in the motion equation form, which is a fourth order approximation for the energy expressions.

To start the analysis, first consider the beam to be slender and inextensible. For an inextensible beam constraint, the arc length of the beam remains constant at all times for all deflection profiles. As noted in Ref. [70], this implies

$$\left(1+u'\right)^2 + v'^2 = 1\,. \tag{3.5}$$

This inextensibility expression is used as a geometric constraint with a Lagrangian multiplier

$$h(s,t) = \lambda(s,t)\left(1-\left(1+u'\right)^2 - v'^2\right)\,. \tag{3.6}$$

Assuming that deformations occur only due to bending, this means that angle ψ can be related to the spatial derivatives along the beam at all times and points by

$$\tan\psi = \frac{v'}{1+u'}\,. \tag{3.7}$$

Following substitution and simplification the system energies are then collected to form the Lagrangian for the system

$$\mathcal{L} = T_B + T_T - V_B - U_M + h\,. \tag{3.8}$$

3.2.2 Nonlinear magnet interactions

To properly analyze the beam with tip interactions, it is first necessary to establish those tip interactions. As shown in Figure 3.2c-d, the tip mass is assumed to include a magnet with a moment direction following the direction of the angle at the beam tip $\psi(L,t)$. The interacting magnet is fixed at a distance d from the undeflected beam end (or $d+L$ from the fixed beam end). To derive the interactions, these two magnets are modeled as magnetic dipoles. For a pair of magnetic dipoles, the field due to one magnet (in this case, the fixed magnet) can be described by

$$\vec{B}_{ft} = -\frac{\mu_0}{4\pi}\left(\frac{\vec{p}_f}{|\vec{r}_{ft}|^3} - (\vec{p}_f \cdot \vec{r}_{ft})\,\frac{3\vec{r}_{ft}}{|\vec{r}_{ft}|^5}\right), \tag{3.9}$$

where $\vec{r}_{ft}$ is a vector from the fixed magnet to the tip magnet, $\vec{p}_f$ is the magnetic moment of the fixed magnet, and $\mu_0 = 4\pi \times 10^{-7}$ H/m is the permeability of free space.

The potential energy of another magnet as a result of the magnetic field is described by

$$U_M = -\vec{p}_t \cdot \vec{B}_{ft}\,. \tag{3.10}$$

where $\vec{p}_t$ is the magnetic moment of the tip magnet. The magnetization moments are $\vec{p} = \vec{M}v$, where v is volume of the magnet and $\vec{M}$ is the magnetization per unit volume vector. For the two magnetics, the fully nonlinear vectors after substitution for the beam tip angle ψ are

$$\vec{p}_f = |M_f|v_f \begin{bmatrix} \text{-1} \\ 0 \\ 0 \end{bmatrix} \quad \text{and} \quad \vec{p}_t = |M_t|v_t \begin{bmatrix} \sqrt{1-v'(L,t)^2} \\ v'(L,t) \\ 0 \end{bmatrix}. \tag{3.11}$$

Likewise, the displacement vector between the magnets with substitution for angle ψ is a function of the two position vector of the magnets

$$\vec{r}_{ft} = \vec{r}_t - \vec{r}_f = \begin{bmatrix} L + u(L,t) + d_m \cos\psi(L,t) \\ v(L,t) + d_m \sin\psi(L,t) \\ 0 \end{bmatrix} - \begin{bmatrix} L + d \\ 0 \\ 0 \end{bmatrix}$$

$$= \begin{bmatrix} u(L,t) + d_m\sqrt{1 - v'(L,t)^2} - d \\ v(L,t) + d_m v'(L,t) \\ 0 \end{bmatrix} . \tag{3.12}$$

where d_m is the distance from the tip of the beam to the center of the tip magnet and d is the distance between the tip of the beam and the center of the fixed magnet. Note that the parameter d_m differs from d_t due to the additional mass of the magnet casing and other tip additions as illustrated in Figure 3.2. This gives a fully nonlinear equation for the potential field between the magnets in terms of the tip angle and displacement.

3.2.3 Nondimensionalization

In order to further generalize the analyses that follow, this section nondimensionalizes the energy expressions. First, for convenience, a ($\tilde{}$) is added for all dimensioned variables, meaning that variables without ($\tilde{}$) are assumed to be dimensionless for the rest of the analysis. Given such a variable change, the dimensioned variables are defined in terms of the dimensionless variables and appropriately dimensional scaling

$$\tilde{v} = Lv \ , \ \tilde{s} = Ls, \ , \tilde{t} = \left(L^2\sqrt{\frac{m_l}{EI_\zeta}}\right) t \ , \text{ and } \tilde{E}_N = E_N^* E_N \, , \tag{3.13}$$

where $\tilde{E}$ represents any of the dimensioned energy expressions, kinetic or potential (T_B, V_B, etc.). It is most convenient to define the energy scaling parameter as $E_N^* = \frac{EI_\zeta}{L}$. As the following derivation shows, this analysis will result in three dimensionless variables

$$\Pi_1 = \frac{m_t}{m_l L} \, , \, \Pi_2 = \frac{d_t}{L} \ , \text{ and } \Pi_3 = \frac{I_{\zeta\zeta}}{m_l L^3} \, , \tag{3.14}$$

which can be used to characterize a wide array of systems and scalings.

The last step to take is to separate a potential solution into two parts, static and dynamic. In this analysis, assume that the static deflection has amplitude an order of magnitude larger such that the substitution for the two parts is

$$v(s,t) = \epsilon V_s(s) + \epsilon^2 v_m(s,t) \tag{3.15}$$

$$u(s,t) = \epsilon^2 U_s(s) + \epsilon^2 u_m(s,t)\,. \tag{3.16}$$

Note the order of the static deflection differs between the axial and flexural coordinates; this decision will be apparent later in the analysis. Taking into account this final substitution, a fourth order approximation is used to arrive at the expressions for the Lagrangian energy and constraint equations

$$T_B = \frac{1}{2}\int_0^1 \left(\dot{u}_m^2 + \dot{v}_m^2\right) ds\,, \tag{3.17}$$

$$V_B = \frac{1}{2}\int_0^1 \left(v_m'\left(2V_s'' + v_m'\right) + V_s''\Big(V_s''\left(1 - 2U_s' - 2V_s'^2 - 2u_m'\right) - 2V_s'\left(U_s'' + u_m''\right)\Big)\right) ds\,, \tag{3.18}$$

$$T_T = \frac{1}{2}\Pi_1\left(\dot{u}_m^2 + \left(\dot{v}_m + \Pi_2 \dot{v}_m'\right)^2\right) + \frac{1}{2}\Pi_3 \dot{v}_m'^2 \quad \text{at } \; s = 1 \tag{3.19}$$

$$V_M = \frac{1}{E_N^*} U_M\,, \tag{3.20}$$

$$h(s,t) = \lambda(s,t)\left(1 - \left(1 + U_s' + u_m'\right)^2 - \left(V_s' + v_m'\right)^2\right)\,. \tag{3.21}$$

3.2.4 Equations of motion

With the dimensionless Lagrangian defined, Hamilton's principle is now applied

$$\int_{t_1}^{t_2} \delta\mathcal{L}\, dt = 0\,. \tag{3.22}$$

Taking the first variation of the dimensionless Lagrangian gives the dimensionless equations of motion, as well as the boundary conditions needed to define fully define

the system. The derivation starts with the static equations and boundary conditions before moving on to the dynamic equations. Starting from deflection in two directions u and v with the inextensionality constraint, the problem simplifies to characterization of static and dynamic deflections of $v(s,t)$.

First, considering only the static variables V_s and U_s, the Lagrangian becomes

$$\mathcal{L} = \frac{1}{2}\int_0^1 \left(\lambda_s(s)\left(1-(1+U_s')^2 - V_s'^2\right) - V_s''\left(V_s''\left(1-2U_s'-2V_s'^2\right) - 2V_s'U_s''\right)\right) ds - V_M \,. \tag{3.23}$$

Taking the first variation of the Lagrange multiplier and rearranging gives an equation for U_s'

$$U_s' = \sqrt{1-V_s'^2} - 1 \,. \tag{3.24}$$

To provide equations for V_s, an expression is also needed for the Lagrange multiplier. Finding the variation of U_s provides a static equation

$$\left(\lambda(s,t)\left(1+U_s'\right) + V_s'V_s'''\right)' = 0 \,, \tag{3.25}$$

which can be solved for the Lagrange multiplier and reduced to fourth order

$$\lambda(s,t) = V_s'V_s'''\left(U_s'-1\right) \,. \tag{3.26}$$

Next, take and collect variations of the static variable V_s and substitute expressions from Eqs. 3.24 and 3.26 to reach a third order nonlinear equation of motion for static deflections

$$V_s''''\left(1+V_s'^2\right) + 4V_s'V_s''V_s''' + V_s''^3 = 0 \,. \tag{3.27}$$

Solving this equation exactly is difficult, therefore Section 3.3.2 details solving an approximation of this static mode from the nonlinear potential energies of the beam and magnet interactions.

Assuming the static deflection is established by approximate solutions, equations for the dynamic modes are developed. First, start with the full expression for the

Lagrangian and find the variation of u_m. With simplification, the zeroing of the first variation of u_m gives

$$\ddot{u}_m = \left(V_s' V_s''' + \lambda \left(1 + U_s' + u_m' \right) \right)' . \tag{3.28}$$

Taking the spatial integration of this expression and rearranging, the nonlinear dynamic with static deflection Lagrange multiplier becomes

$$\lambda(s,t) = \frac{\int_0^s \ddot{u}_m \, ds - V_s' V_s'''}{\sqrt{1 - V_s'^2} + u_m'} . \tag{3.29}$$

Before finding the variation of v_m to find the final equation of motion, the variation of the Lagrangian multiplier is taken and rearranged to yield an expression for u_m'

$$u_m' = -V_s' v_m' - \frac{1}{2} v_m'^2 . \tag{3.30}$$

Next, the variation of v_m is taken and Eq. 3.29 substituted for the Lagrange multiplier. The expression in Eq. 3.30 is then integrated over the beam coordinate s and the second derivative is taken with respect to time to find a substation for $\ddot{u}_m$ in Eq. 3.29. With these substitution and a third order approximation, the simplification of the variation equation becomes

$$\ddot{v}_m + \left(\left(\int_0^s \frac{\partial^2}{\partial t^2} \left(\int_0^s V_s' v_m' ds \right) ds \right) V_s' + \left(1 + V_s'^2 \right) V_s''' + v_m''' \right)' = 0 . \tag{3.31}$$

This is the nonlinear partial differential equation (PDE) that describes small oscillations about a moderate static beam deflection for a cantilever beam with setup from Figure 3.2c-d. The complexity of this problem means that an approximate solution is necessary to properly characterize the vibration modes of this problem; this is developed later in the chapter.

The setup for Figure 3.2a-b is found by eliminating the static deflection terms from Eq. 3.31 such that it becomes

$$\ddot{v}_m + v_m'''' = 0\,. \tag{3.32}$$

In the nonlinear example, boundary forces and torques were not listed because the equation of motion does not lend itself to a typical linear PDE analysis.

Without the tip force or torque, the solution method requires boundary conditions at either end of the beam. These emerge from the process of integration by parts required in taking the first variations of the oscillation variables and can be further defined by the geometric considerations of the system. For the fixed end $s = 0$ the boundary conditions are geometric and are

$$v_m = 0 \quad \text{and} \quad v_m' = 0\,, \tag{3.33}$$

while the boundary conditions at $s = 1$ represent shear and moment balancing and are

$$v_m''' = \Pi_1 \left(\ddot{v}_m + \Pi_2 \ddot{v}_m'\right) \tag{3.34}$$

$$v_m'' = \text{-}\Pi_1\Pi_2 \left(\ddot{v}_m + \Pi_2 \ddot{v}_m'\right) - \Pi_3 \ddot{v}_m'\,. \tag{3.35}$$

Keeping the dimensionless parameters, gives the boundary conditions for Figure 3.2b, while setting $\Pi_1 = I_{\zeta\zeta} = 0$ gives the conditions for a massless cantilever beam.

3.3 Mode Shape Analysis

The equations of motion for various cases are described in dimensionless form by Eqs. 3.31-3.35. This section analytically finds the mode shapes for the simple cases of Fig. 3.2a-b first. Next, the nonlinear magnetic tip interactions are included and a Rayleigh-Ritz approximate method is used to find the convergent natural frequencies and mode shapes.

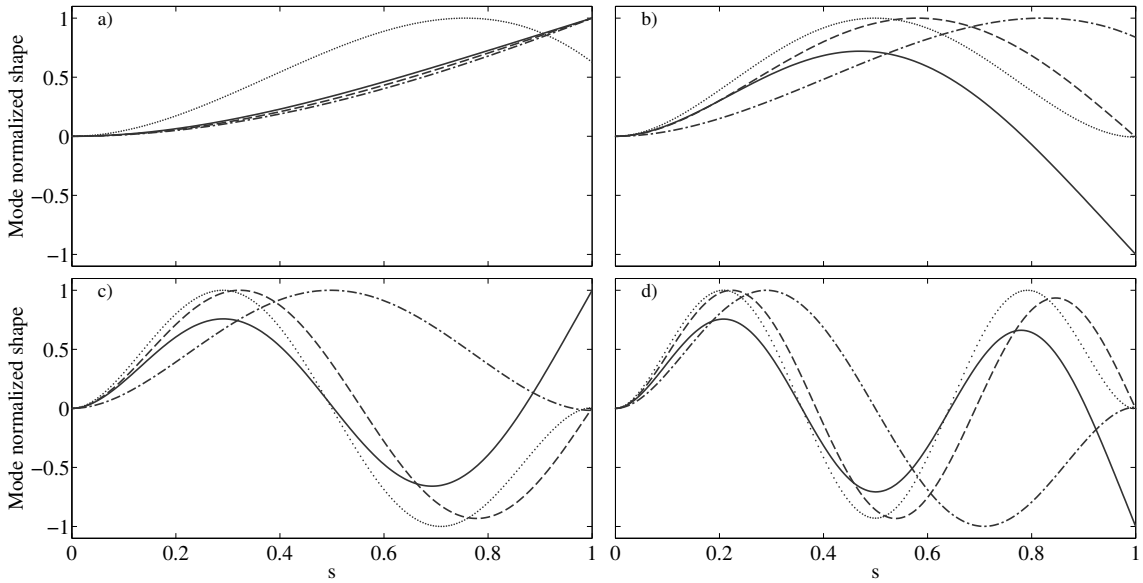

FIGURE 3.3: First four mode shapes a)-d) of four different tip boundary condition cases: cantilever beam with no tip mass (solid line), point tip mass without offset (dashed), tip mass with rotational inertia and no offset (dotted), rotational inertia and offset (dash-dot). Dimensionless natural frequency η for each mode in order of the four cases (solid, dashed, dotted, dash-dot): $\eta_1 = 3.516$, 0.2849, 1.085, 0.1797; $\eta_2 = 22.03$, 15.44, 22.45, 1.507; $\eta_3 = 61.70$, 49.99, 61.73, 22.55; $\eta_4 = 120.9$, 104.3, 121.0, 61.81. Dimensionless variables $\Pi_1 = 36.72$, $\Pi_2 = 0.3073$, and $\Pi_3 = 4.334$.

3.3.1 Exact linear analytical solutions

Consider Eqs. 3.32-3.35. These equations fully describe the oscillating system with no nonlinear magnetic tip interactions, either with or without a mass and tip rotational inertia. From Eq. 3.32, a dynamic solution of the form

$$v_m(s,t) = V(s)q_v(t)\,. \tag{3.36}$$

was assumed. This was substituted into Eq. 3.32 to obtain

$$\frac{\ddot{q}_v}{q_v} = -\frac{V''''}{V} = -\eta^2\,. \tag{3.37}$$

Here η is the dimensionless frequency of the time varying component. With this definition, the time varying part of the solution is

$$q_v(t) = A\cos\eta t\,, \tag{3.38}$$

where A is the dimensionless amplitude. Rearranging again, the fourth order spatial equation becomes

$$V'''' - \eta^2 V = 0\ . \tag{3.39}$$

This can then be solved for the mode shape expression as a function of the spatial coordinate s. Next, apply the clamped end boundary conditions of a fixed zero defection and zero spatial derivative to get a modified mode shape with two unknown constants

$$V(s) = A_V\left(\sin\sqrt{\eta}s - \sinh\sqrt{\eta}s\right) + B_V\left(\cos\sqrt{\eta}s - \cosh\sqrt{\eta}s\right)\ . \tag{3.40}$$

For a cantilever beam with no tip mass, the moment balancing boundary condition of Eq. 3.35 is used with $\Pi_1 = 0$ and $\Pi_3 = 0$ for

$$V(s) = A_V\left(\sin\sqrt{\eta}s - \sinh\sqrt{\eta}s - \frac{\sin\sqrt{\eta} + \sinh\sqrt{\eta}}{\cos\sqrt{\eta} + \cosh\sqrt{\eta}}\left(\cos\sqrt{\eta}s - \cosh\sqrt{\eta}s\right)\right)\ . \tag{3.41}$$

Note here that A_V scales the mode shape and is often set to a convenient value to normalize a mode by total mass or other methods. To find the dimensionless natural frequencies of the beam η, the shear balancing boundary condition of Eq. 3.34 is used with $\Pi_1 = 0$ yield the characteristic equation

$$1 + \cos\sqrt{\eta}\cosh\sqrt{\eta} = 0\,, \tag{3.42}$$

which can be solved for multiple values of η and thus multiple system natural frequencies.

A similar procedure is followed for the beam with tip mass. The moment balance boundary condition of Eq. 3.35 is first used to find the mode shape and takes the form

$$V'' = \eta^2 \Big(\Pi_1 \Pi_2 \left(V + \Pi_2 V' \right) + \Pi_3 V' \Big) . \tag{3.43}$$

The shear balance at $s = 1$ of Eq. 3.34 is then used to derive the characteristic equation, taking the form

$$V''' = \text{-}\eta^2 \Pi_1 \left(V + \Pi_2 V' \right) . \tag{3.44}$$

Figure 3.3 shows the first four modes for the four different cases with variations of the boundary conditions at the tip. Plots a)-d) show modes 1-4 for each case. A solid line represents the case of a cantilever beam with no tip mass. A dashed line represents an idealized tip mass that sits at the end of the beam with no offset or rotational inertia. The dotted line accounts for rotational inertia with the mass center at the beam tip, while a dash-dot line includes rotational inertia and mass offset. This figure illustrates the similarities and differences that different boundary conditions have on the mode shapes of the first four modes.

A few interesting patterns are shown in this figure. For the first mode in Figure 3.3a, the dotted line case is the only clear departure from the standard first mode behavior because the tip interaction is dominated by the rotational large rotational inertia. This rotational inertia almost acts as a pin for the next three modes, as shown by the near zero displacement at the free tip. Similarly, the other massed beam cases represented by the dashed line and the dash-dot line show a similar pinned shape for the higher modes as a result of the mass acting like a tip resistance to displacement. For the highest frequencies, it is interesting to note the near zero displacement effect that the offset mass and rotational inertia have on the mode shape as seen from the dotted line case and the dash-dot case. Noting the frequencies, there exists a huge discrepancy between the three massed setups (dashed, dotted, dash-dot) for each of

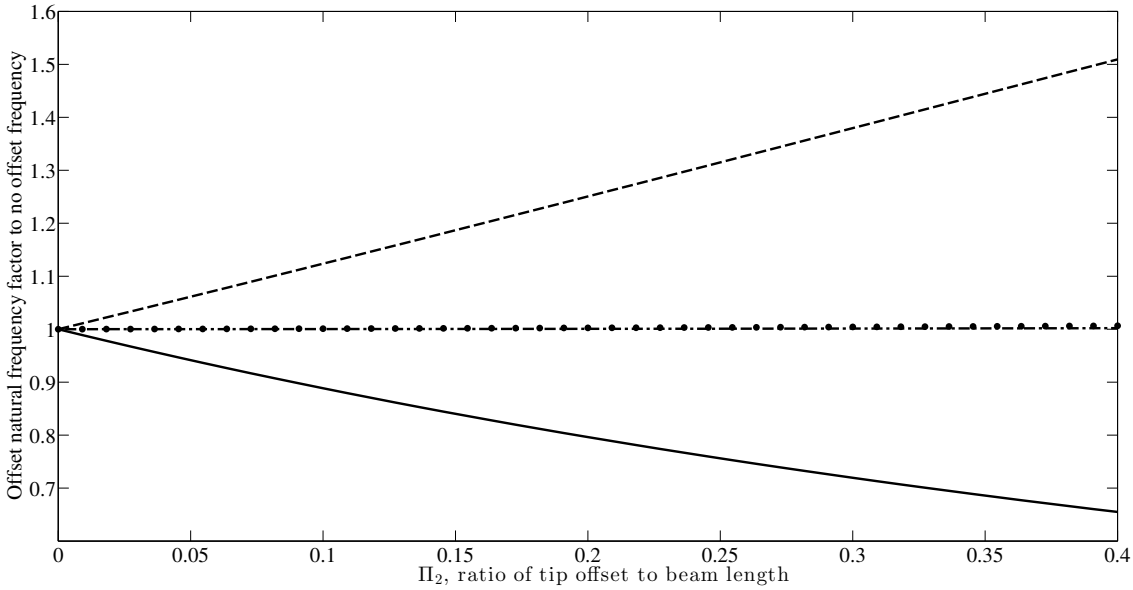

FIGURE 3.4: Shifting frequencies of the first four vibration modes (solid, dashed, dotted, dash-dot) for the linear case with rotational inertia and tip offset with changes to the dimensionless offset parameter Π_2. Dimensionless variables $\Pi_1 = 36.72$, and $\Pi_3 = 4.334$.

the modes, which points to the importance of tip offset and rotational inertia to the validity of the model.

To investigate the effect of a shifting center of mass, Fig. 3.4 shows the shifting natural frequencies of the first three modes for different values of Π_2. As the mass is centered farther from the tip, the first frequency is driven down as a result of the increase of the required tip shear and moment balancing. Interestingly, the second mode is driven up, while modes 3 and 4 show small, mostly insignificant increases in natural frequency. Shifting the center of mass slightly outward or inward from the tip can allow for tenability of the first second modes.

3.3.2 Approximate solutions

For the cantilever with nonlinear magnetic interactions, a direct analytical approach will fail to capture the full behavior potential of the problem. With the magnetic po-

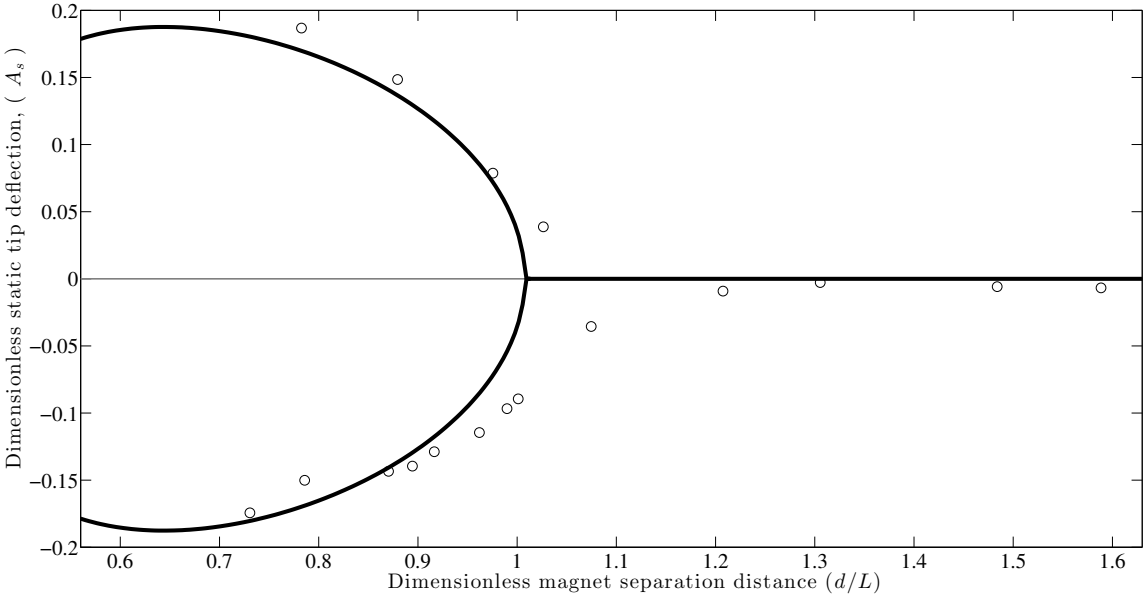

FIGURE 3.5: Bifurcation diagram for static tip deflection with a normalized tip distance as the bifurcation parameter. A thick line indicates a stable solution, thin line unstable. Circles indicate nondimensionalized experimental results.

tential energy included into the problem, the interaction can be made strong enough to induce a static deflection of the beam which will fall outside the linear approximations. Statically, the beam will deflect as the magnetic interactions grow larger than the elastic restoring force of the beam. First, this section solves for the static solution. Then approximate methods are used to solve for the dynamic solutions.

First it is necessary to solve the static solution by finding tip deflections with zero net force. This is done by finding the miminums of the potential energy of the system when expressed as a function of tip deflections. Using Eq. 3.24 for U_s', insert this into the static potential energy expression from Eq. 3.18 and 3.20 to find the potential system energy

$$V = \frac{1}{2}\int_0^1 V_s''^2\left(1 + V_s'^2\right) ds + V_M(V_s', V_s)\big|_{s=1}\,. \tag{3.45}$$

Considering the resulting mode shape equation is nonlinear with highly nonlinear

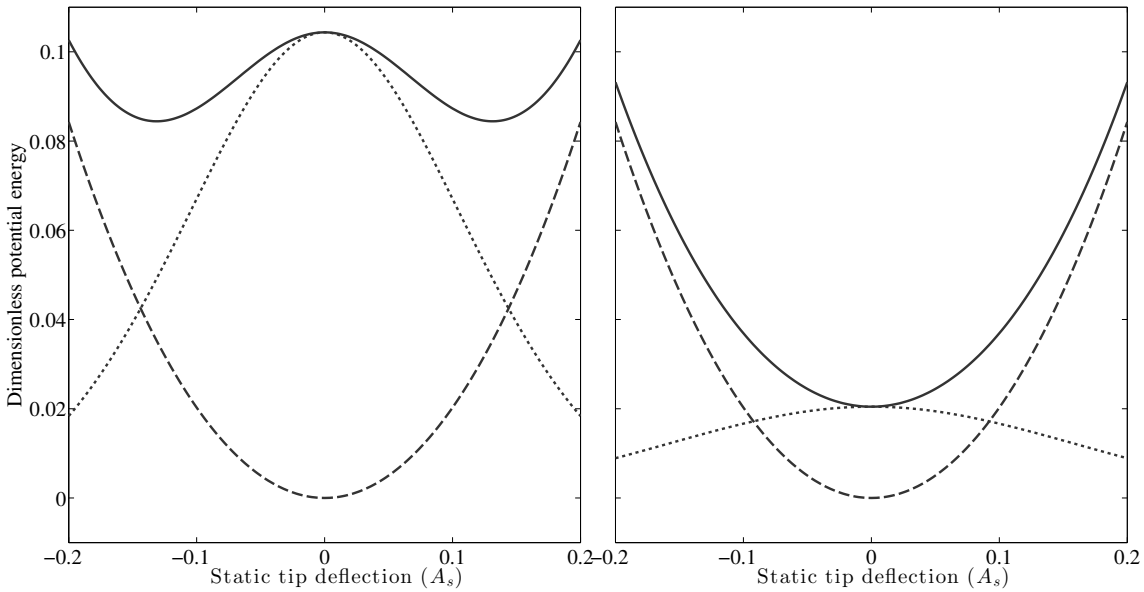

FIGURE 3.6: Dimensionless potential energy diagram for two normalized magnet spacing. The dotted line is magnet energy, the dashed line is beam energy, and the solid line is a summation of the two to illustrate fixed points minima and stability. The left graph is for normalized magnet spacing of 0.0308 and the right for 0.0489 (d/L).

magnetic tip interactions, the tip mode is assumed to be a summation of polynomials in the beam span variable s. For simplicity, the solution is only a single term, ensuring that the geometric boundary conditions for a cantilever are met. This gives a static mode equation

$$V_s(s) = A_s s^2 \,. \tag{3.46}$$

To solve for this expression, insert V_s and it's derivatives into the potential energy expression and minimize with respect to the static tip amplitude A_s. By doing so, the fixed point deflection of the system about which small oscillations can occur is estimated. Figure 3.5 shows a bifurcation of this static equilibrium with bifurcation parameter d scaled with the system length scale for d/L. Figure 3.6 shows the beam and magnetic energies at two illustrative scaled separation distances.

Given the complexities of the nonlinear PDE in Eq. 3.31, approximate solutions

were used for the dynamic equations. This approximate solution method is known as the Rayleigh-Ritz method and is detailed below. Before delving into the analysis, however, it is first necessary to demonstrate that such an analysis is valid. To do so, the linear operator associated with the elastic forces in the system is self-adjoint. Given the following system

$$\mathrm{L}v = Mv\,, \tag{3.47}$$

where L is a differential operator, it follows that if the differential operator is self-adjoint, the resulting eigenvalues of the problem are unique and the eigenfunctions orthogonal. To satisfy the self-adjoint condition, the inner product of the operator and it's adjoint must be equal such that

$$\langle \mathrm{L}v, v\rangle = \langle v, \mathrm{L}^*v\rangle \tag{3.48}$$

and $\mathrm{L} = \mathrm{L}^*$. Despite the addition of the static nonlinear deflection, the differential operator is simply

$$\mathrm{L}\,v_m = \frac{\partial^4}{\partial s^4} v_m\,. \tag{3.49}$$

It follows that this linear operator is provably self-adjoint, and thus the system satisfies the conditions for the use of the Rayleigh-Ritz method.

The Rayleigh-Ritz method works using the Rayleigh quotient, which is a ratio of potential energy to kinetic energy in the system with ignorance of time dependence. By eliminating the time varying elements and assuming maximum or reference energy [69], this quotient acts as a minimizable eigenvalue for the system being explored

$$R(v_m) \equiv \lambda \equiv \omega^2 \equiv \frac{V_{max}}{T_{ref}}\,. \tag{3.50}$$

For the case in this analysis, a separable solution is assumed

$$v_m(s,t) = V(s)q(t) \tag{3.51}$$

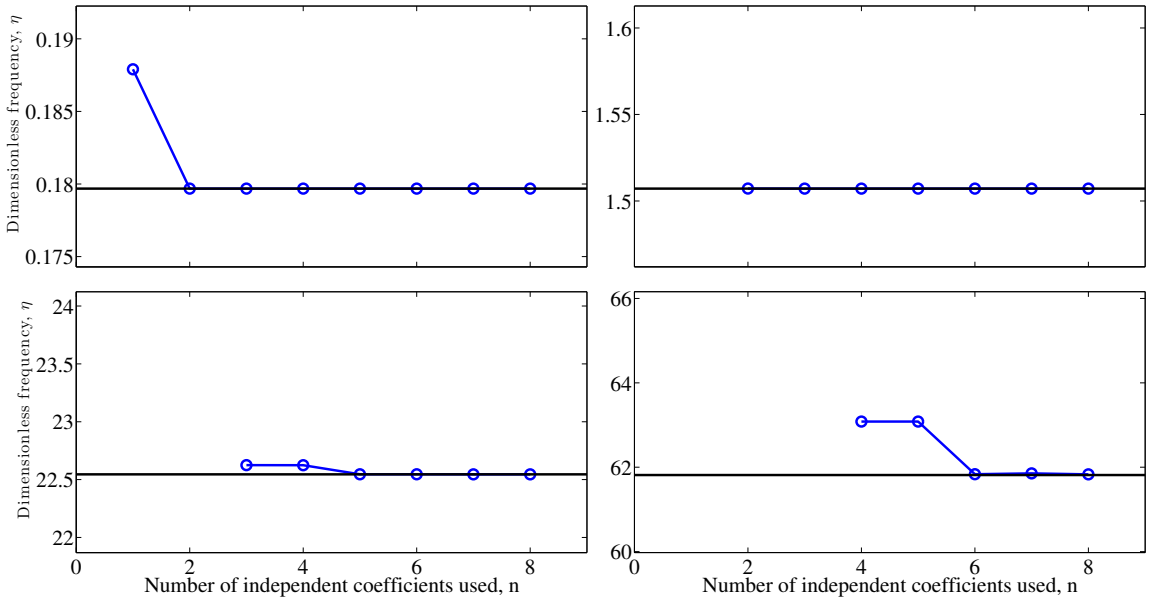

FIGURE 3.7: Rayleigh-Ritz results represented by lines with circles showing rapid convergence for the first four natural frequencies, indicated by a horizontal solid line, for the linear case with rotational inertia and tip offset .

where the mode shape is an n degree polynomial with independent coefficients that satisfies the geometric boundary conditions for the cantilever beam, $v_m = 0$ and $v'_m = 0$,

$$V(s) = a_1 s^2 + a_2 s^3 + a_3 s^4 + ... + a_{n-1} s^n \,. \tag{3.52}$$

Following the derivation in Meirovitch [69], a set of minimizing equations for each coefficient can be solved of the form

$$\frac{\partial N}{\partial a_i} - \lambda \frac{\partial D}{\partial a_i} \quad \text{for } i = 1, 2, ..., n-1 \,, \tag{3.53}$$

where N is the numerator of the Rayleigh quotient, D is the denominator, and in this section $\lambda = \omega^2$. Solving this nonlinear system of equations yields the eigenvalues and eigenvectors (and thus the mode shapes) of the system. The eigenvalue approximation value that the Rayleigh quotient finds acts as an upper bound. Use of an exact analytical solution for the mode shape yields the exact eigenvalues and func-

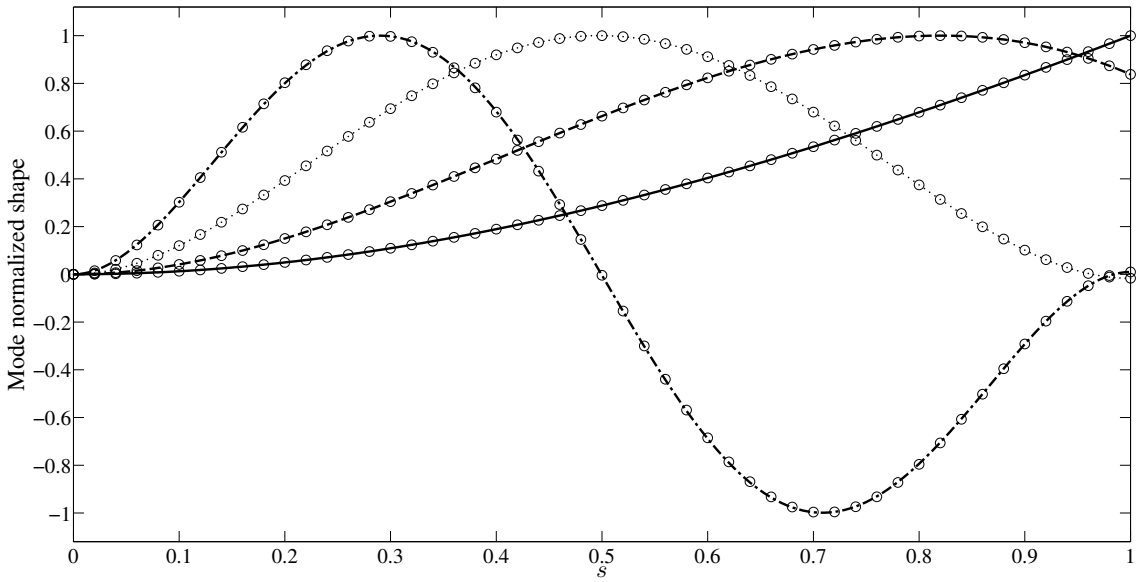

FIGURE 3.8: Comparison of the first four modes (solid, dashed, dotted, dash-dot lines) for the linear case with rotational inertia and tip offset with the exact analytical solution (lines) and the Rayleigh-Ritz polynomial approximation represented by circles.

tions. The use of a polynomial allows for emulation of this shape for lower frequency modes. By increasing the number of terms, the mode shapes are more appropriately matched and the eigenvalues become more accurate. As the terms increase, the calculation time increases along with accuracy as the solution converges to the natural eigenvalues of the system.

For this system, a polynomial with up to $n = 9$ is considered. As a proof of concept, consider the beam frequency for a beam with a tip mass that is offset and has rotational inertia and with no nonlinear magnetic tip interactions (and thus no static deflection). Following Figure 3.7, the trend shows that as n increases, the Rayleigh-Ritz method approaches the exact analytical expressions for small oscillations. Because the polynomials act as such great approximations of the modes, the convergence is very quick, requiring very few terms to match the behavior. Figure 3.8 illustrates the accuracy of this energy based approximate method for the linear case.

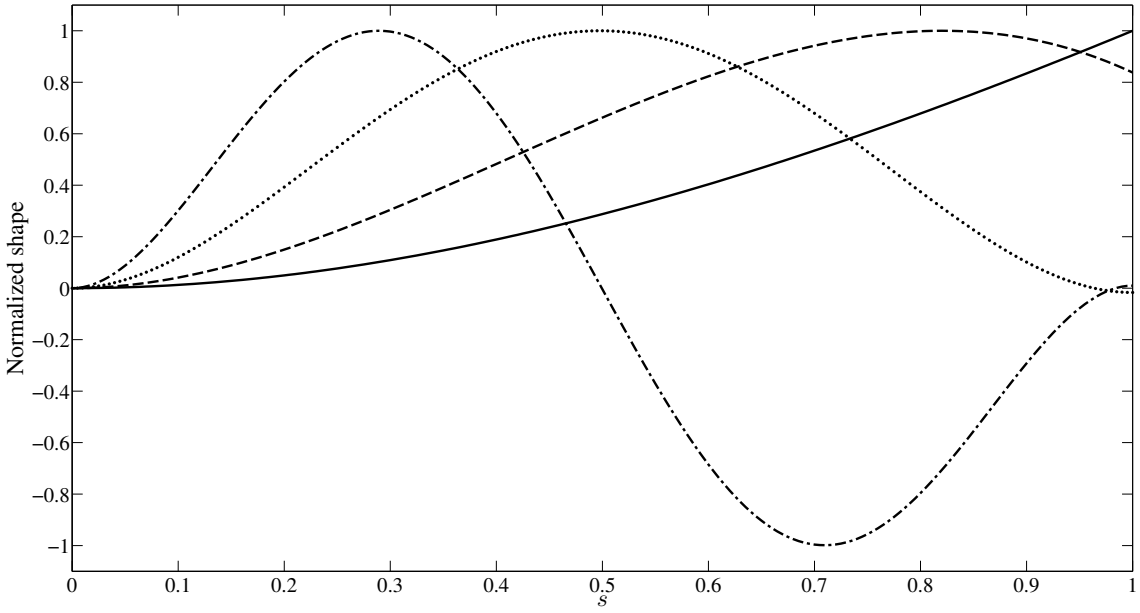

FIGURE 3.9: Rayleigh-Ritz mode shapes about static deflected geometry with $n = 9$ for the first four modes for the cantilever with nonlinear magnetic tip interactions. Dimensionless frequencies for the first four modes are 0.0903, 0.4292, 3.138, 9.595.

The circle symbols of the Rayleigh-Ritz approximation are almost exactly aligned with the analytical solutions for the first four modes.

Expanding this method to the nonlinear partial differential equations that take into account static deflection gives the mode shapes about the deflected beam geometries. The first case, shown in Figure 3.9, comes from the same static deflection and parameters as the potential energy function on the left in Figure 3.6. The validity of this method as it relates to actual experimental systems is examined in the next section.

3.4 Experimental demonstration

This section describes a series of experiments performed to validate the theoretical analyses of the previous sections. These actions were designed to characterize this particular system and connect with the phenomenological results of the numerical

Table 3.1: System parameters for experimental studies.

Parameter	Value	Units
Carbon fiber modulus of elasticity, E	65	GPa
Linear mass density, m_l	11.0	g/m
Beam length, L	39.3	mm
Second moment of inertia, I_ζ	0.458	mm^4
Beam tip to center of tip mass, d_t	12.1	mm
Beam tip to center of magnet, d_m	13.2	mm
Tip mass rotational inertia, $I_{\zeta\zeta}$	2890	g/mm^2
Magnetization, $\|M\|$, Br/ μ_0	$1.32/(4\pi \times 10^{-7})$	T / (H/m)
Magnet volume, $\hat{v}_1$, $\hat{v}_2$	1608.8	mm^3
Beam separation distance, d	28.6	mm

and theoretical exploration. The experimental system used to replicate the theoretical results of the previous sections is shown in Figure 3.1.

First, the validity of the static beam deflection approximations was examined. Figure 3.5 shows the experimental measurements as circles overlaid onto the theoretical approximation for the deflection of the beam tip. One important feature of this overlay is the asymmetry in the bifurcation towards the negative deflection branch. The theoretical system is idealized as a straight line with perfect symmetry, however in practice a slight imperfection can cause the symmetry breaking bifurcation shown in the the experimental bifurcation result [71].

Next, selected separation distance configurations were tested for their first natural frequencies. Figure 3.10 shows the physical, dimensionless results, overlaid on top of a theoretical approximation from the Rayleigh-Ritz method. Discrepancies between the theoretical and experimental results are the result of slight asymmetry in the system and the limitations of a local linearization near the bifurcation point. Near this point, the local stiffness linearization of the magnet interactions approaches infinity. This leads to negative approximation values for λ and non-real natural frequencies. The slight underestimation of the natural frequencies points to a slight

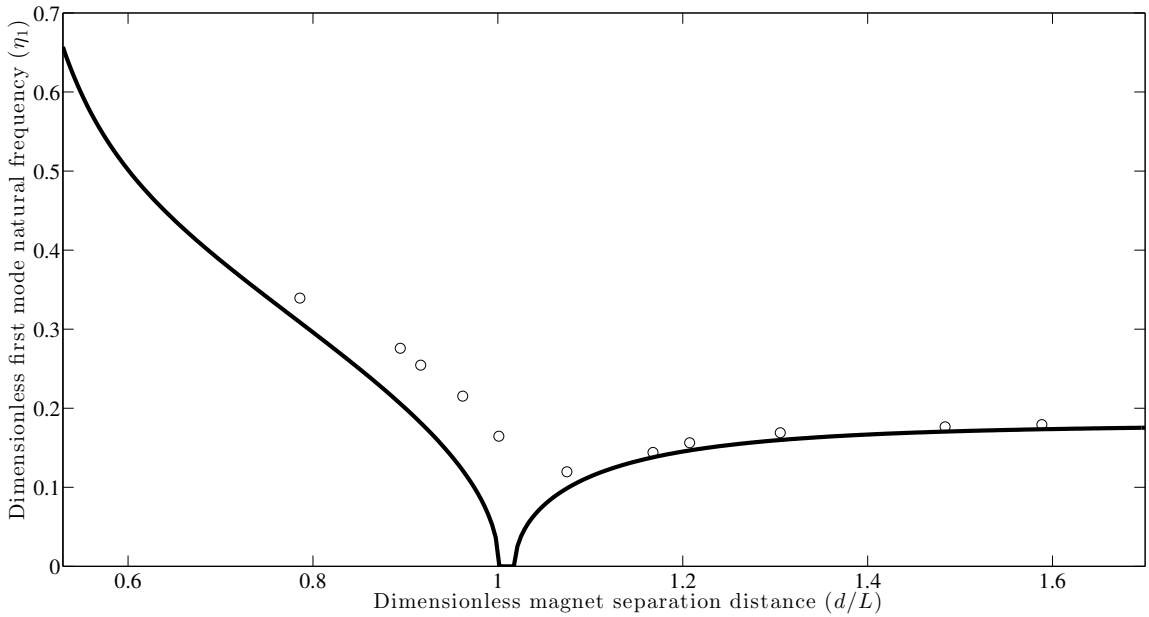

FIGURE 3.10: First mode natural frequencies for different dimensionless separation distances using Rayleigh-Ritz method with $n = 9$ as lines and an overlay of the experimental results as circles.

underestimation of the magnet strength or beam stiffness, possibly due to symmetry breaking bifurcations resulting from an asymmetric experimental setup.

The last experimental consideration are the mode shapes themselves. Figure 3.11 illustrates both the static and the dynamic test results. Plot a) shows a static deflection configuration for the beam and magnet system. Circles show experimental tests derived from image processing, while the line represents the approximated shape. Plot b) illustrates the unity normalized mode shapes off of this static deflection. Using a PSV-400 scanning laser vibrometer, the first two experimental mode shapes were captured (circle with line, square with line) and are shown next to the Rayleigh-Ritz derived approximate modes (black and grey lines) in Figure 3.11. Although the experimental results show considerable variation, the general shape is consistent with the approximate methods estimations. The top figure illustrates a likely overestimate of the nonlinear hardening behavior of moderately deflected

beams, resulting in an exaggerated restoration force and thus a beam showing less deflection than the experimental results. For the dynamic modes, the pre-deflected beam presented a challenge for the mode shape measurements because of the great curvature of the configuration.

3.5 Conclusions

The analysis of this chapter provides an exploration into the effects of highly nonlinear boundary interactions on beam dynamics in the context of a weakly nonlinear beam stiffness approximation. Exact analytical solutions provide accurate solutions for problems with small amplitudes, even with complex boundary conditions. These analytical expressions are used in the system with an atypical tip mass configuration to illustrate the changing beam dynamics for adjusts to tip mass, tip mass offset, and rotational inertia effects.

While exact analytical solutions are ideal for the less complex problems, the existence of highly nonlinear magnetic tip interactions and static deflections requires a more finesse approach. By using admissible functions and utilizing the principles of the Rayleigh-Ritz energy methods, convergent solutions are found for frequencies and mode shapes that mirror the actual physical behavior. In problems where nonlinearity prevents analytical methods, the numerical approximations of Rayleigh-Ritz act as an appropriate substitute, provided care is taken to understand the validity of the approximations and limitations of the approximations required to make the analysis admissible.

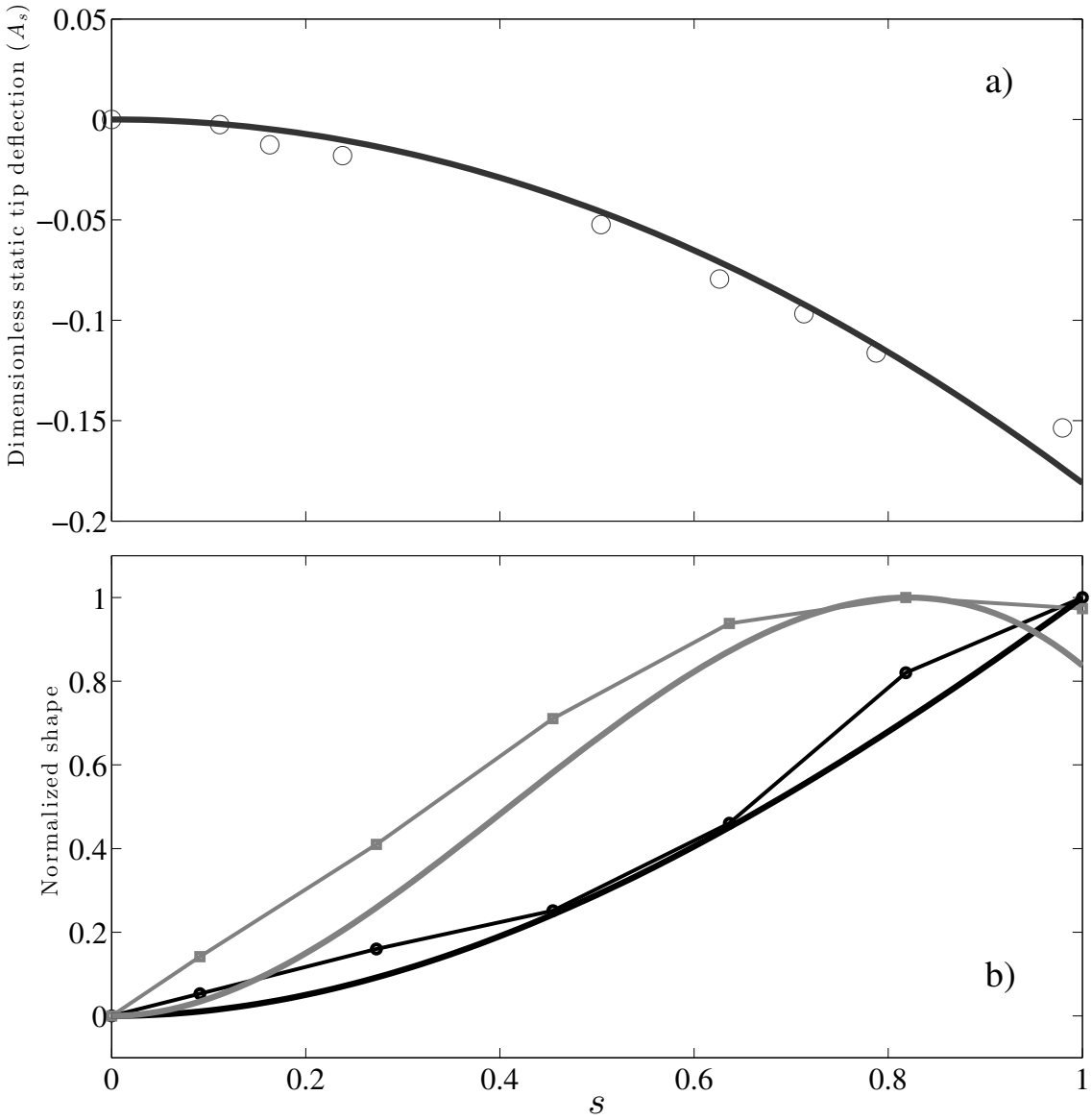

FIGURE 3.11: Static deflection a) and first two dynamic modes b). For the static deflection, a line represents the approximated shape and the circles are experimental tests. For the dynamic modes, the first mode is shown in black with theoretical shape (line) and experimental shape (line with circles) and the second is shown in grey with theoretical shape (line) and experimental shape (line with squares).

4

Linear and nonlinear coupling models

The use of environmental energy harvesters to augment or replace batteries [1, 3, 8, 9, 72] can be a valuable aspect to a remote sensing systems. While environmental energy comes in many forms, a large class of these harvesters are vibration-based, converting ambient environmental vibration into electrical energy, often through piezoelectric or electromagnetic transduction. Electromagnetic induction-based harvesters consist of a coil of wire surrounding a magnet; as the magnet (or coil) oscillates, the changing magnetic flux induces a voltage in the coil. A large portion of previous studies have described the electromagnetic coupling between the magnet and coil with a linear model [13, 73, 74]; however, others have recognized the nonlinearity of this coupling and its dependance on magnet positioning [3, 5, 75–77]. Similarly, in piezoelectric harvesters, the nonlinearities inherent in piezo-beams have been studied for effects on damping and piezoelectric coupling [78–81].

This chapter investigates a vibration-based harvester that uses electromagnetic induction for energy conversion. In addition to studying response behavior and power delivered to an electrical load for linear coupling, a unique feature of the

present study lies in the exploration of nonlinear coupling. To elaborate, the two types of electromagnetic coupling can be described as: 1) a nonlinear coupling model, where the magnetic flux gradient is dependent on the coil and magnet positioning, and 2) a linear coupling model, where the magnetic flux gradient is constant at all magnet positions. While the nonlinear model is based on an actual physical system, the linear model is hypothetical. The specific nonlinear model for this chapter is described in later sections and is based on a typical magnet-coil system, i.e., similar to those in Refs. [3, 13, 76, 82].

While most prior works have only considered the case of single-frequency excitation [3, 9, 13], many real-world excitation sources contain contain multiple frequencies, as recognized by Refs. [7, 83]. This highlights another unique feature of the present study, as we have compared the response behavior of the linear or nonlinear coupling models for multi-frequency excitation. This investigation, along with the studies of the single-frequency excitation with nonlinear coil coupling, provides a broader picture of benefits and detriments of linear and nonlinear coupling in a diverse excitation environment.

The work of this chapter is organized as follows. The next section develops a model for the nonlinear coupling by modeling the magnet as a dipole and applying the principles of magnetic induction. The governing equations are then derived from the energy relationships of the mechanical and electrical systems. These equations are then used in Section 4.2 to develop analytical solutions for the steady-state behavior with either nonlinear or linear coupling and various types of single-frequency excitation. The results from the approximate analytical solutions are then compared with numerical studies. In Section 4.3, the case of multi-frequency excitation is examined, requiring the application of different analytical approaches. This is done to show the differing behavior of the nonlinear coupling models with more complex multi-frequency excitation.

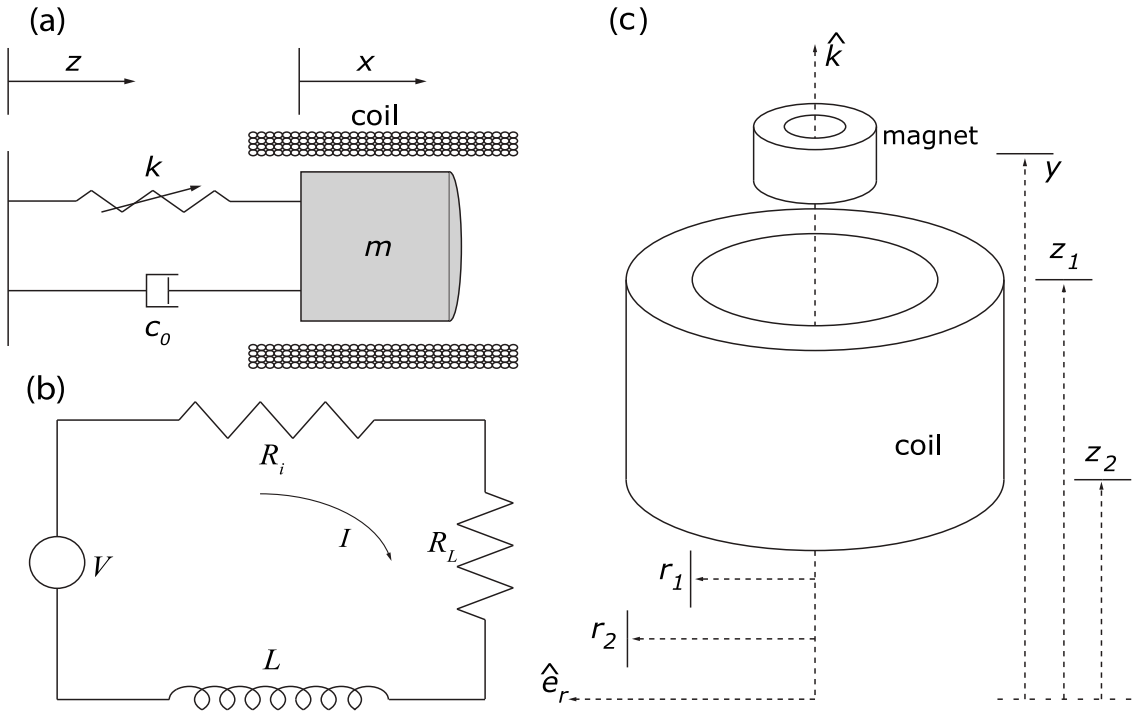

FIGURE 4.1: Mechanical system representation (a), electrical system circuit configuration diagram (b), and coil and oscillating magnet diagram with relevant parameters (c).

4.1 Energy Generator Model

The setup for the theoretical system explored in this chapter is shown in Fig. 4.1. The mechanical system in Fig. 4.1a consists of a modified mass-spring-damper where the spring and damper are attached to a magnetic proof mass and surrounded by a wire coil. Note that x is the position of the magnet, while z is the position of the base/coil. The electrical system Fig. 4.1b consists of the coil, with its associated inductance, internal resistance, and coupling voltage, and a resistive load. Fig. 4.1c shows relevant dimensions for the coil and the relative position y, where $y = x - z$, of the magnet with respect to the coil along the $\hat{k}$ axis.

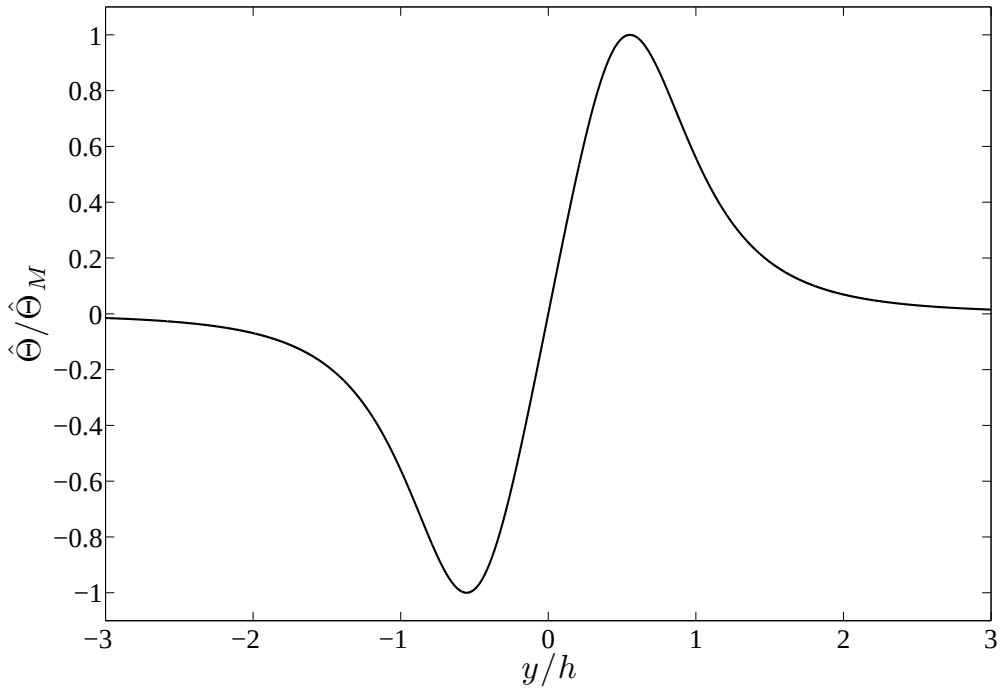

FIGURE 4.2: Dimensionless coil flux vs. distance ratio from coil center along oscillation axis with $\Delta x = 0.03$ m. Coil and magnetic parameters are in Tab. 4.1 and $\hat{\Theta}_M = 2.1079$ N/A.

4.1.1 Coil interactions

The magnet-coil interactions will be derived from two key principles: the dipole model for magnetic fields and Faraday's law of induction for a coil of wire (see Refs. [13, 40, 84, 85]), which will be used to model the electromagnetic coupling voltage.

First, the magnetic fields of the moving magnet will be modeled by a magnetic dipole. A magnetic dipole is a mathematical simplification of a magnet with a magnetic moment contained in an infinitesimal volume. The **B**-field generated by a dipole can be given by

$$\mathbf{B} = -\frac{\mu_0}{4\pi}\nabla\frac{\mathbf{m}_s \cdot \mathbf{r}_m}{|\mathbf{r}_m|^3} = -\frac{\mu_0}{4\pi}\left(\frac{\mathbf{m}_s}{|\mathbf{r}_m|^3} - (\mathbf{m}_s \cdot \mathbf{r}_m)\frac{3\mathbf{r}_m}{|\mathbf{r}_m|^5}\right), \tag{4.1}$$

where $\mu_0 = 4\pi \times 10^{-7}$ H/m is the permeability of free space, or magnetic constant, ∇ represents a vector gradient operation, and $\mathbf{r}_m = \mathbf{r}_p - \mathbf{r}_s$ is a vector from the magnetic dipole to a given point. The magnetic moment of the dipole magnet is given by

$$\mathbf{m}_s = \mathbf{M}_s v_s, \tag{4.2}$$

where v_s is volume of the source magnet, $\mathbf{M}$ is the magnetization vector. The magnitude of the magnetization vector is $|\mathbf{M}| = \frac{B_r}{\mu_0}$, where B_r is the residual magnetic flux density. For the system diagramed in Fig. 4.1, $\mathbf{r}_p = r\hat{e}_r + x\hat{k}$ and $\mathbf{r}_s = y\hat{k}$. Substitution of the moment and position vectors into Eq. 4.1 provides an equation for the B field at a point due to the magnet

$$\mathbf{B} = \frac{B_r v_s}{4\pi} \left(\frac{3r\,(x-y)\,\hat{e}_r - \left(r^2 - 2\,(x-y)^2\right)\hat{k}}{\left(r^2 + (x-y)^2\right)^{5/2}} \right). \tag{4.3}$$

To find the voltage resulting from electromagnetic coupling interactions, an expression for the magnetic flux of a single coil must next be derived. Magnetic flux, a measurement of magnetic field strength over a given area, is modeled by the dot product of a B-field and that area, or

$$\Phi = \oint_S \mathbf{B} \cdot \mathrm{d}\mathbf{A}\,, \tag{4.4}$$

where S is the surface of the given area and $d\mathbf{A}$ is an infinitesimal slice of this surface. Using the B-field expression given by Eq. 4.3 and taking the surface to be a circle enclosed by a single wire of our coil, the flux becomes

$$\Phi = \int_0^{2\pi}\int_0^{r} \mathbf{B} \cdot \left(r\,\mathrm{d}r\,\mathrm{d}\theta\,\hat{k}\right) = \frac{B_r v_s}{2} \frac{r^2}{\left(r^2 + (x-y)^2\right)^{3/2}}\,. \tag{4.5}$$

For the given system, it is necessary to obtain the average flux over the entire length and width of the finite coil. Integration over the length and width gives the average

Table 4.1: Electrical and mechanical system parameters for analytical and simulated studies for single and multi-frequency excitation.

Parameter	Value	Units
Coil inductance, L	0.08	H
Number of coil turns, N_c	1500	—
Fill factor, ξ	0.33	—
Length of coil, $\Delta x = x_2 - x_1$	0.03	m
Inside coil diameter, $2r_1$	0.0175	m
Outside coil diameter, $2r_2$	0.025	m
External load resistance, R_L	1200	Ω
Circuit resistance to inductance ratio, ρ	15000	Ω/H
Residual flux density, B_r	1.31	T
Magnet volume, v_s	5×10^{-6}	m^3
Magnet mass, m	0.04	kg
Natural frequency, $\omega_0/2\pi$	5	Hz
Damping coefficient, ζ	0.075	—

flux expression for a coil turn over its cross-section,

$$\Phi_a = \frac{1}{A_c} \int_{x_1}^{x_2} \int_{r_1}^{r_2} \Phi \, \mathrm{d}r \, \mathrm{d}x \,, \tag{4.6}$$

where the integration bounds coincide with Fig. 4.1 and A_c is the cross-sectional area. To find the total flux, the average is multiplied by the number of wire turns and a fill factor ξ, which represents the ratio of conductive cross-section to total cross-section in the coil, or $N_c A_w / A_c$, where N_c is the number of coil turns and A_w is the conductive area of a single wire cross-section.

With a representation of the total coil flux, Faraday's law is applied to find the voltage across the coil, ε. Faraday's law states that a potential difference is created as the result in a change in flux, thus

$$\varepsilon = -\frac{\mathrm{d}}{\mathrm{d}t} \left(\xi N_c \Phi_\mathrm{a} \right) \,. \tag{4.7}$$

In first evaluating the time derivative, note that only y will vary in time for the given

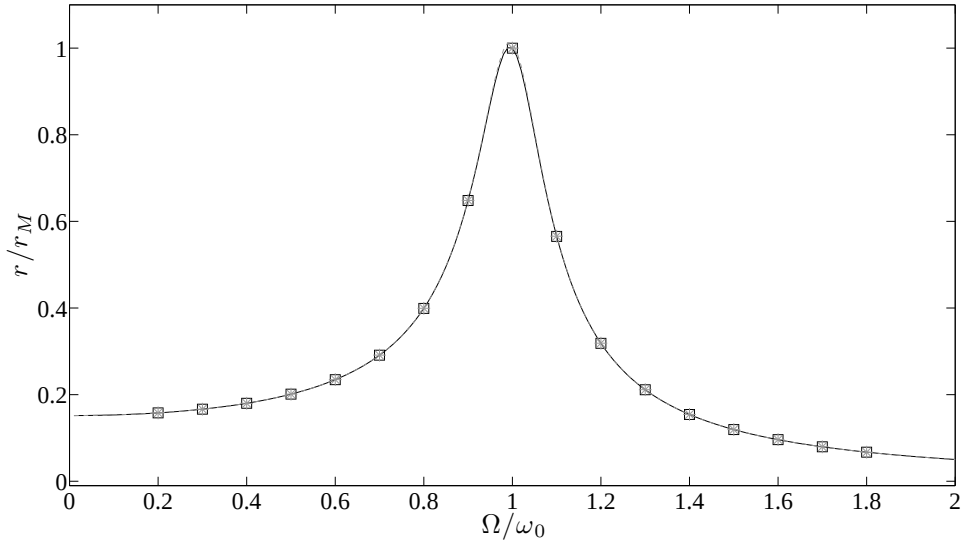

FIGURE 4.3: Dimensionless mechanical response vs. excitation frequency for single-frequency excitation with $r_M = 33.409$ mm. Lines (black for constant and grey dashed for nonlinear) are analytical solutions and symbols (black square for constant and grey asterisks for nonlinear) are numerical studies.

system. Therefore, the coupling voltage can be represented by

$$\varepsilon = \left(-\frac{3N_c B_r v_s \xi}{2A_c} \int_{x_1}^{x_2} \int_{r_1}^{r_2} \frac{r^2 (x-y)}{\left(r^2 + (x-y)^2\right)^{5/2}} \mathrm{d}r\mathrm{d}x \right) \dot{y} = \hat{\Theta}(y)\dot{y}\,, \tag{4.8}$$

where $\hat{\Theta}$ is the coupling term. Evaluating the integral portion of Eq. 4.8, $\hat{\Theta}$ becomes

$$\hat{\Theta} = \frac{N_c B_r v_s \xi}{2A_c} \sum_{i,j=1}^{2} (-1)^{i+j} \left(\ln(r_i + Z_{ij}) - \frac{r_i}{Z_{ij}} \right)\,, \tag{4.9}$$

where $Z_{ij}^2 = r_i^2 + (x_j - y)^2$ and $A_c = (r_2 - r_1)(x_2 - x_1)$. Fig. 4.2 shows the coil flux results for the system parameters in Table 4.1 at different magnet positions. This general form of the coil flux is consistent with other models in the literature [3, 75].

4.1.2 Governing equations

To derive the governing equations for the coupled electromechanical system, Lagrangian energy derived formulas are used. This requires the establishment of kinetic, potential, and dissipative energy functions [47]. The kinetic energy is a function of the translation of the magnetic mass, current flow through the inductor, and electromagnetic coupling and can be expressed as

$$T = \frac{1}{2}m\dot{x}^2 + \frac{1}{2}L\dot{q}^2 + T_{\mathrm{C}}\,, \tag{4.10}$$

where m is the mass of the oscillating magnet, L is the coil inductance, q is the charge coordinate, and T_{C} is the electromagnetic coupling term. To find the coupling term T_C, it is assumed that the coil interactions result in negligible energy losses from eddy currents and other effects and therefore the electrical and mechanical coupling energy are equal. To find this energy, the electrical power, $P_e = \varepsilon\dot{q}$, is integrated over time giving

$$T_{\mathrm{C}} = \int_0^t \varepsilon\dot{q}\,\mathrm{d}t = \int_0^t \dot{y}\,\hat{\Theta}(y)\dot{q}\mathrm{d}t = \dot{q}\int_0^y \hat{\Theta}(y)\mathrm{d}y\,. \tag{4.11}$$

These two energy expressions will later be used to derive the coupling terms for the equations of magnet motion and charge flow. Since the system has no capacitor for energy storage, the potential energy is simply

$$U = \frac{1}{2}ky^2\,, \tag{4.12}$$

where k is the spring constant. The last energy expression is for the non-conservative terms and is defined as

$$D = \frac{1}{2}c_0\dot{y}^2 + \frac{1}{2}(R_L + R_i)\dot{q}^2\,, \tag{4.13}$$

where c_0 is the viscous mechanical damping constant, R_i is the internal resistance of the coil, and R_L is the resistance of an external load.

For deriving governing equations of the mechanical and electrical system, one form of the generalized Lagrange equation is used,

$$\frac{\mathrm{d}}{\mathrm{d}t}\left(\frac{\partial T}{\partial \dot{q}_n}\right) - \frac{\partial T}{\partial q_n} + \frac{\partial D}{\partial \dot{q}_n} + \frac{\partial V}{\partial q_n} = Q_n \,, \tag{4.14}$$

where q_n is a generalized coordinate, Q_n is the generalized forcing, and T, D, and V are the system energies found in Eqs. 4.10–4.13. Choosing y as the generalized coordinate and using the relation $y = x - z$, the mechanical equation becomes

$$m\ddot{y} + c_0\dot{y} + ky - \hat{\Theta}I = -m\ddot{z} \,, \tag{4.15}$$

where I has been substituted for $\dot{q}$, and $\ddot{z}$ is the base acceleration. For the purposes of this chapter, $-m\ddot{z}$ has been chosen to be a single or multi-frequency oscillation of the form $\sum_{n=1}^{N} A_n \sin \Omega_n t$. Simplifying, Eq. 4.15 becomes

$$\ddot{y} + 2\zeta\omega_0\dot{y} + \omega_0^2 y - \frac{\hat{\Theta}}{m}I = \sum_{n=1}^{N} \Gamma_n \sin \Omega_n t \,, \tag{4.16}$$

where $\omega_0 = \sqrt{k/m}$ is the natural frequency, $\zeta = \frac{c_0}{2m\omega_0} = \frac{c_0}{2\sqrt{km}}$ is the damping coefficient, and $\Gamma_n = A_n/m$.

Next, q was chosen as the generalized coordinate to obtain the electrical differential equation,

$$L\dot{I} + (R_L + R_i)I + \hat{\Theta}\dot{y} = 0 \,, \tag{4.17}$$

where I and $\dot{I}$ have been substituted for $\dot{q}$ and $\ddot{q}$, respectively. As with the mechanical equation, Eq. 4.17 is simplified and becomes

$$\dot{I} + \rho I + \frac{\hat{\Theta}}{L}\dot{y} = 0 \,, \tag{4.18}$$

where $\rho = (R_L + R_i)/L$ represents a ratio of circuit resistance to inductance.

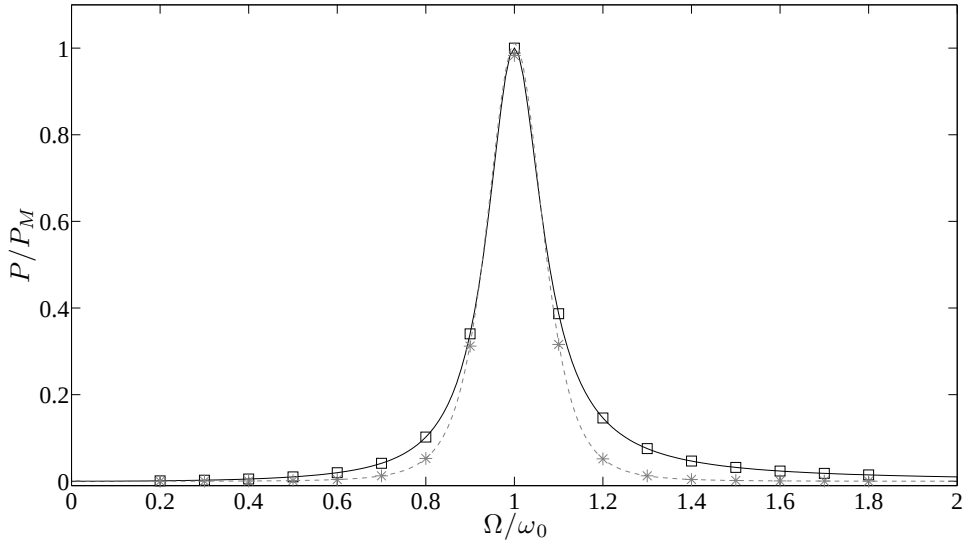

FIGURE 4.4: Dimensionless electrical power vs. excitation frequency for single-frequency excitation with $P_M = 1.1399$ mW. Lines (black for constant and grey dashed for nonlinear) are analytical solutions and symbols (black square for constant and grey asterisks for nonlinear) are numerical studies.

4.1.3 Average power

For comparison purposes between the different coupling models, an expression for the average power across the electrical load is found. Since instantaneous power is given by $P = R_L I^2$, it follows that the average power over the excitation period is

$$P_a = \frac{1}{T}\int_0^T R_L I^2 \, \mathrm{d}t \,, \tag{4.19}$$

where $T = 2\pi/\Omega$. For responses with incommensurate frequencies, the average power is given by

$$P_a = \lim_{T\to\infty} \frac{1}{T}\int_0^T R_L I^2 \, \mathrm{d}t \,. \tag{4.20}$$

Since it is impossible to allow $T \to \infty$, the asymptotic value of the time average power is calculated.

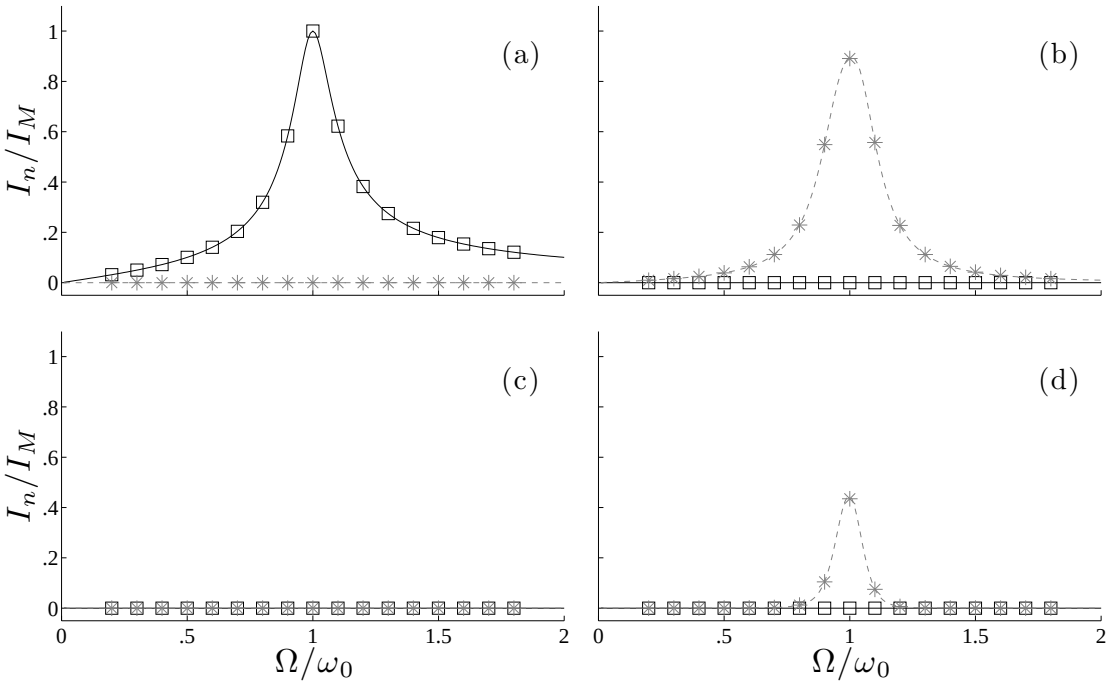

FIGURE 4.5: Dimensionless current for first four harmonics vs. excitation frequency for single-frequency excitation. Lines (black for constant and grey dashed for nonlinear) are analytical solutions and symbols (black square for constant and grey asterisks for nonlinear) are numerical studies. $I_M = 1.3784$ mA and the first to the fourth harmonics are shown in graphs (a) - (d).

4.2 Single frequency excitation

This section will use analytical and numerical techniques to investigate the harvester response behavior for single-frequency excitation. Separate variations of excitation amplitude and frequency will be explored. Results will be displayed in the form of the oscillator response amplitude, the harmonic content of the current in the electrical circuit, and the average power across the resistive load. Eqs. 4.16 and 4.18 will be solved analytically in two forms for comparison. The first will assume linear electromagnetic coupling with $\hat{\Theta}$ at a constant value, while the second will assume nonlinear coupling with $\hat{\Theta}$ in the form of Eq. 4.9 and thus dependent on y.

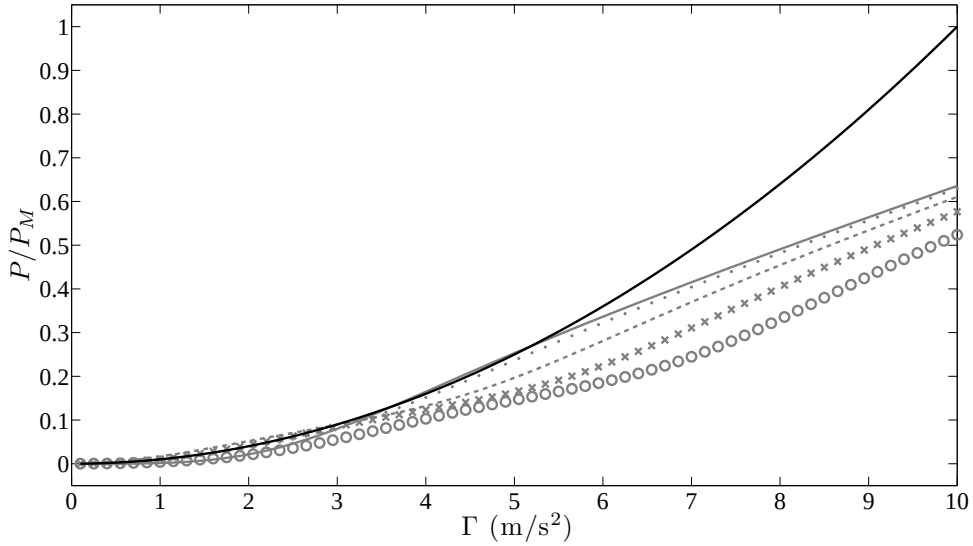

FIGURE 4.6: Dimensionless electrical power vs. excitation amplitude for single-frequency excitation with $P_M = 4.5596$ mW. Black represents linear coupling analytical solutions, while grey is nonlinear coupling. Solid, dotted, dashed, x's, and circles represent coil positioning at $y = 0$, 8.3, 16.6, 24.9, 33.2 mm, respectively.

4.2.1 Linear coupling response

This section examines the harvester's response when the coupling term is accurately modeled by a constant. Solutions are assumed to be in the form of a truncated Fourier series with $y = a\sin\Omega t + b\cos\Omega t$ and $I = c\sin\Omega t + d\cos\Omega t$. The corresponding first and second time derivatives become

$$\dot{y} = a\Omega\cos\Omega t - b\Omega\sin\Omega t\,, \tag{4.21}$$

$$\ddot{y} = -b\Omega^2\cos\Omega t - a\Omega^2\sin\Omega t\,, \tag{4.22}$$

$$\dot{I} = c\Omega\cos\Omega t - d\Omega\sin\Omega t\,. \tag{4.23}$$

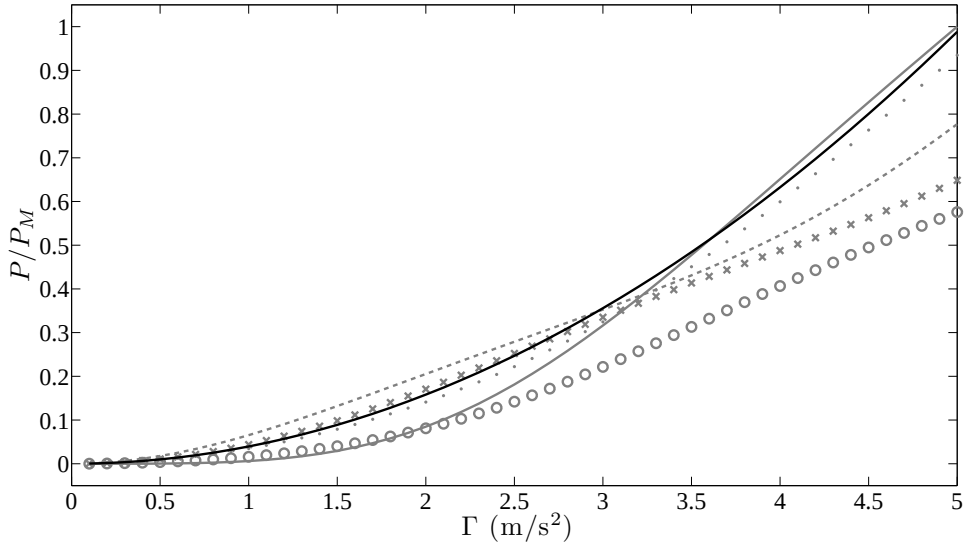

FIGURE 4.7: Dimensionless electrical power vs. excitation amplitude for single-frequency excitation at low amplitudes. Black represents linear coupling analytical solutions, while grey is nonlinear coupling. Solid, dotted, dashed, x's, and circles represent coil positioning at $y = 0$, 8.3, 16.6, 24.9, 33.2 mm, respectively and $P_M = 1.1534$ mW.

With substitution of the time derivatives and balancing cosine and sine harmonics, Eqs. 4.16 and 4.18 produce four algebraic equations

$$-2\zeta\omega_0\Omega a + \left(\Omega^2 - \omega_0^2\right) b + \frac{\hat{\Theta}}{m} d = 0\,, \tag{4.24}$$

$$\left(\Omega^2 - \omega_0^2\right) a + 2\zeta\omega_0\Omega b + \frac{\hat{\Theta}}{m} c + \Gamma = 0\,, \tag{4.25}$$

$$-\frac{\hat{\Theta}}{L}\Omega a - \Omega c - \rho d = 0\,, \tag{4.26}$$

$$\frac{\hat{\Theta}}{L}\Omega b + \Omega d - \rho c = 0\,. \tag{4.27}$$

Coefficients c and d of the electrical response can then be found in terms of

coefficients a and b of the mechanical response and system constants,

$$c = \frac{\hat{\Theta}\Omega}{L\left(\rho^2 + \Omega^2\right)}\left(\rho b - \Omega a\right)\,, \tag{4.28}$$

$$d = -\frac{\hat{\Theta}\Omega}{L\left(\rho^2 + \Omega^2\right)}\left(\rho a + \Omega b\right)\,. \tag{4.29}$$

Substituting Eq. 4.28 and Eq. 4.29 back into Eq. 4.24 and Eq. 4.25 gives

$$\left(2\zeta\omega_0\Omega + \frac{\hat{\Theta}^2\Omega\rho}{Lm\left(\rho^2 + \Omega^2\right)}\right)a - \left(\left(1 - \frac{\hat{\Theta}^2}{Lm\left(\rho^2 + \Omega^2\right)}\right)\Omega^2 - \omega_0^2\right)b = 0\,, \tag{4.30}$$

$$\left(2\zeta\omega_0\Omega + \frac{\hat{\Theta}^2\Omega\rho}{Lm\left(\rho^2 + \Omega^2\right)}\right)b + \left(\left(1 - \frac{\hat{\Theta}^2}{Lm\left(\rho^2 + \Omega^2\right)}\right)\Omega^2 - \omega_0^2\right)a = -\Gamma\,. \tag{4.31}$$

By squaring and adding these two equations, an expression for the oscillator response amplitude is found

$$\left(\left(2\zeta\omega_0\Omega + \frac{\hat{\Theta}^2\Omega\rho}{Lm\left(\rho^2 + \Omega^2\right)}\right)^2 + \left(\left(1 - \frac{\hat{\Theta}^2}{Lm\left(\rho^2 + \Omega^2\right)}\right)\Omega^2 - \omega_0^2\right)^2\right)r^2 = \Gamma^2\,, \tag{4.32}$$

where $r^2 = a^2 + b^2$. Solving Eq. 4.32, this response amplitude is

$$r = \frac{\Gamma}{\sqrt{\left(2\zeta\omega_0\Omega + \frac{\hat{\Theta}^2\Omega\rho}{Lm(\rho^2+\Omega^2)}\right)^2 + \left(\left(1 - \frac{\hat{\Theta}^2}{Lm(\rho^2+\Omega^2)}\right)\Omega^2 - \omega_0^2\right)^2}}\,. \tag{4.33}$$

The electrical response is then derived from Eqs. 4.28 and 4.29 and given by

$$I = \sqrt{c^{\,2} + d^{\,2}} = \left(\frac{\hat{\Theta}\Omega}{L\sqrt{\rho^2 + \Omega^2}}\right)r\,. \tag{4.34}$$

From the electrical response, the average power across the resistive load, as presented by Eq. 4.19, is given by

$$P_a = \frac{\Omega}{2\pi}\int_0^{\frac{2\pi}{\Omega}} R_L I^2\,\mathrm{d}t = \frac{1}{2}R_L\left(c^{\,2} + d^{\,2}\right) = R_L\left(\frac{\hat{\Theta}^2\Omega^2}{2L\left(\rho^2 + \Omega^2\right)}\right)r^{\,2}\,. \tag{4.35}$$

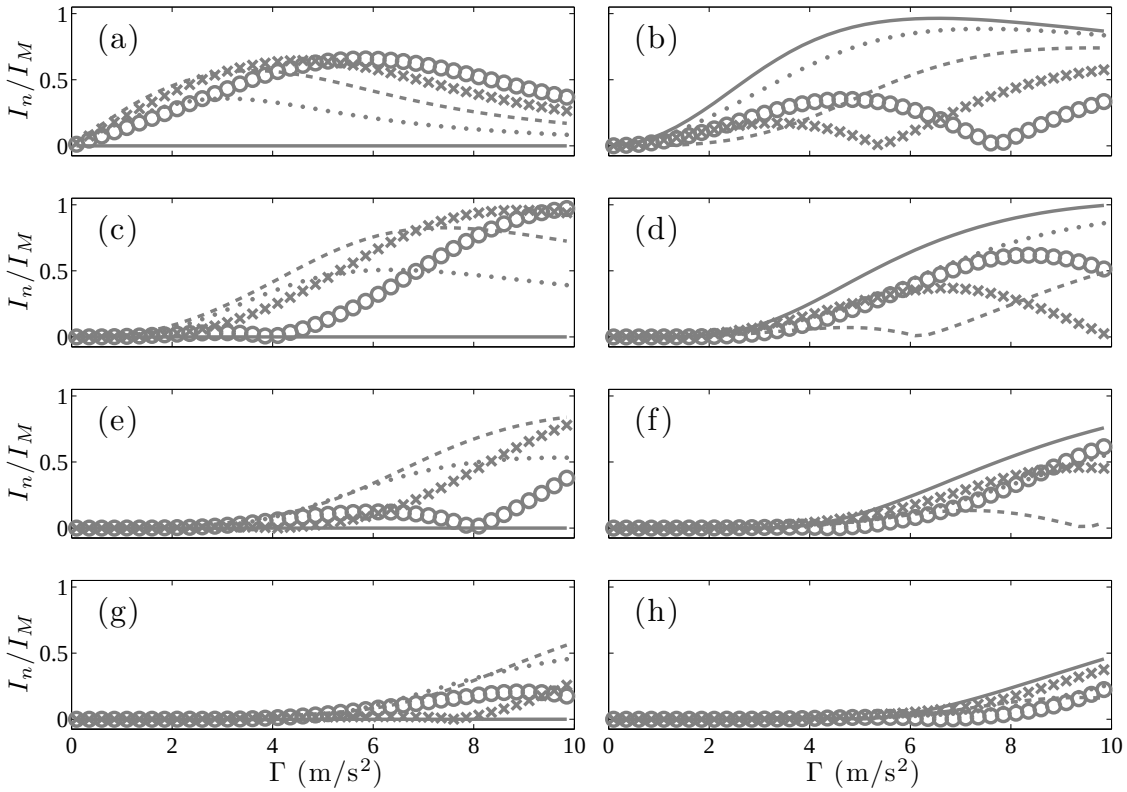

FIGURE 4.8: Dimensionless current for first eight harmonics vs. excitation amplitude for single-frequency excitation. Nonlinear coupling analytical results are represented by solid, dotted, dashed, x's, and circles for coil positioning at $y = 0$, 8.3, 16.6, 24.9, 33.2 mm, respectively. $I_M = 1.356$ mA and the first to the eighth harmonics are shown in graphs (a) - (h).

4.2.2 Nonlinear coupling response

This section examines the case of nonlinear coupling. First, it is assumed that the coupling term has a negligible effect on the response of the mechanical system. An analytical solution for the mechanical response can then be found as before, using a truncated Fourier series where $y = a \sin \Omega t + b \cos \Omega t$. Substitution of the first and second time derivatives from Eq. 4.21 and 4.22 into Eq. 4.16 and neglecting coupling

produces two algebraic equations

$$-2\zeta\omega_0\Omega a + \left(\Omega^2 - \omega_0^2\right) b = 0\,, \tag{4.36}$$

$$\left(\Omega^2 - \omega_0^2\right) a + 2\zeta\omega_0\Omega b + \Gamma = 0\,. \tag{4.37}$$

Next, the oscillator response amplitude is found by solving the above equations then squaring and adding the resulting equations. With simplification, the oscillator response amplitude of the system with ignored coupling is

$$r = \frac{\Gamma}{\sqrt{\left(2\zeta\omega_0\Omega\right)^2 + \left(\Omega^2 - \omega_0^2\right)^2}}\,. \tag{4.38}$$

Note that this expression is identical to Eq. 4.33 if $\hat{\Theta}$ is set to zero. This solution can now be broken down into a and b coefficient components,

$$a = -\frac{\left(\Omega^2 - \omega_0^2\right)\Gamma}{\left(2\zeta\omega_0\Omega\right)^2 + \left(\Omega^2 - \omega_0^2\right)^2}\,, \tag{4.39}$$

$$b = -\frac{\left(2\zeta\omega_0\Omega\right)\Gamma}{\left(2\zeta\omega_0\Omega\right)^2 + \left(\Omega^2 - \omega_0^2\right)^2}\,. \tag{4.40}$$

To find the electrical circuit response, Eq. 4.18 was rearranged such that the coupling term acts as a forcing term for the electrical circuit

$$\dot{I} + \rho I = -\frac{\hat{\Theta}}{L}\dot{y} = F_{\mathrm{E}}\,. \tag{4.41}$$

However, since $\hat{\Theta}$ is highly nonlinear, a partially numerical approach is most appropriate for finding the system response. First, as with the linear coupling, a solution in the form of a truncated Fourier series of N-terms is assumed,

$$I = \sum_{n=1}^{N} \left(c_n \sin n\Omega t + d_n \cos n\Omega t\right)\,. \tag{4.42}$$

Given this assumed solution form, analytical solutions for I are most easily found if a Fourier expansion is first computed of F_{E} in the form

$$F_{\mathrm{E}} = \sum_{n=1}^{N} \left(f_n \sin n\Omega t + g_n \cos n\Omega t \right) . \tag{4.43}$$

In order to find f_n and g_n, the orthogonal properties of cosine and sine functions are utilized. By multiplying both sides by $\sum_{m=1}^{N} \sin m\Omega t$ and then by $\sum_{m=1}^{N} \cos m\Omega t$ and integrating from 0 to $2\pi/\Omega$ with respect to time, all terms multiplying sine by cosine or where $m \neq n$ drop out. This creates two integral expressions which can be simplified to give symbolic values for the n^{th} Fourier expansion terms

$$f_n = \frac{\Omega}{\pi} \int_0^{\frac{2\pi}{\Omega}} F_{\mathrm{E}} \sin n\Omega t \, \mathrm{d}t \, , \tag{4.44}$$

$$g_n = \frac{\Omega}{\pi} \int_0^{\frac{2\pi}{\Omega}} F_{\mathrm{E}} \cos n\Omega t \, \mathrm{d}t \, , \tag{4.45}$$

where the integral functions are most easily computed numerically, using the analytically derived oscillator response. The final equation required to solve Eq. 4.41 is the first time derivative of I,

$$\dot{I} = \sum_{n=1}^{N} n\Omega \left(c_n \cos n\Omega t - d_n \sin n\Omega t \right) . \tag{4.46}$$

Substituting $\dot{I}$, I, and the Fourier expansion of F_{E} into Eq. 4.41, balancing harmonics, and then solving the resulting algebraic equations gives

$$c_n = \frac{\rho f_n + n\Omega g_n}{\rho^2 + (n\Omega)^2} \, , \tag{4.47}$$

$$d_n = \frac{\rho g_n - n\Omega f_n}{\rho^2 + (n\Omega)^2} \, , \tag{4.48}$$

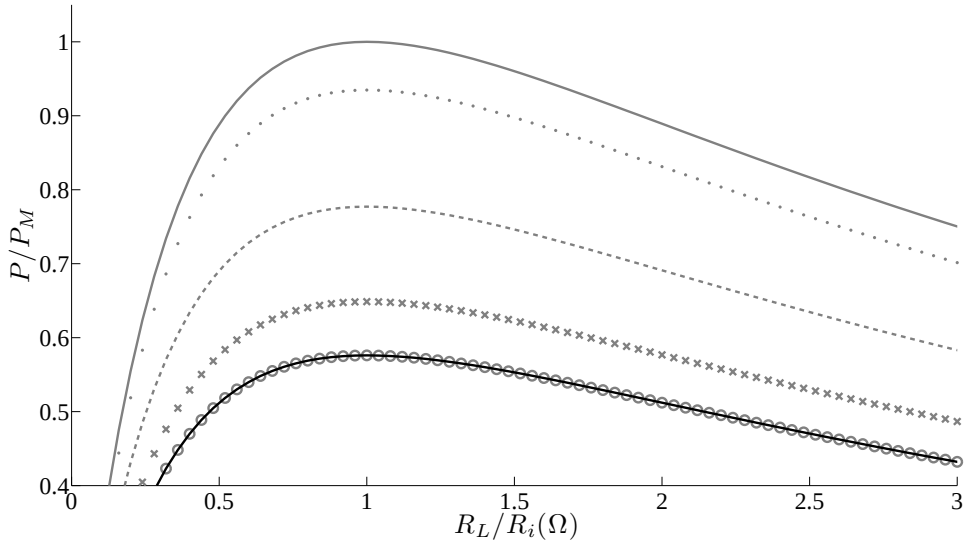

FIGURE 4.9: Dimensionless electrical power vs. resistive load normalized by internal resistance. Black represents linear coupling analytical solutions, while grey is nonlinear coupling. Solid, dotted, dashed, x's, and circles represent coil positioning at $y = 0$, 8.3, 16.6, 24.9, 33.2 mm, respectively. P_M and R_i are 2.7664 mW and 125 Ω.

for a given n^{th} harmonic of the mechanical forcing frequency. Using the current response, the power across the resistive load is found using Eq. 4.19 and is given by

$$P_a = \frac{\Omega}{2\pi}\int_0^{\frac{2\pi}{\Omega}} R_L I^2 \, \mathrm{d}t = \frac{1}{2}R_L \sum_{n=1}^{N}\left(c_n^2 + d_n^2\right) = \frac{1}{2}R_L \sum_{n=1}^{N}\left(\frac{f_n^2 + g_n^2}{\rho^2 + (n\Omega)^2}\right). \qquad (4.49)$$

4.2.3 Comparisons to Numerical Studies

To confirm the ability of the analytical approximations to predict the system response and expected power output, a series of numerical studies were performed. Simulations were run with linear and nonlinear coupling over a range of input frequencies about the natural frequency. Each simulation was executed with a single input frequency and amplitude until the responses reached a steady state. Fast Fourier transforms of position and current data at steady state were then calculated

to extract the frequency content. For the mechanical response r, only amplitude data at the excitation frequency was used in Fig. 4.3. Power across the resistive load in Fig. 4.4 was calculated as an average over an excitation period in accordance with Eq. 4.19. For the current data in Fig. 4.5, amplitudes of the first four frequencies were used.

The first set of plots in Figs. 4.3 - 4.5 show numerical studies overlaying analytically obtained results versus excitation frequency. For these figures, the coil was centered at $y = 0$ mm, base excitation was $\Gamma = 5$ m s^{-2}, and four harmonic terms were calculated, i.e., $N = 4$. The remaining system parameters can be found in Tab. 4.1. In examining the plots, first note that the analytical response curves match well with the simulated investigations for both coupling types. The mechanical response is similar regardless of the coupling model used due to the small effect of the coupling term for mechanical oscillations. This is illustrated by the negligible difference between results for linear and nonlinear coupling as shown in Fig. 4.3. For the dimensionless power results, Fig. 4.4 shows a wider peak power band with linear as opposed to nonlinear coupling at the given excitation amplitude and coil positioning. One difference is found in the harmonically dissected electrical response of Fig. 4.5. With linear coupling, the current response only contains the forcing frequency, however with the centered-coil nonlinear coupling, the current response contains the second and fourth harmonics.

The second set of plots, Figs. 4.6 - 4.8, show analytically obtained results versus excitation amplitude. For both figures, excitation frequency was held constant at the natural frequency, 5 Hz, and the different lines represent varying coil positions. Fig. 4.6 shows that power output for the theoretical linear coupling increases quadratically with excitation amplitude because of the squared electrical term. The nonlinear coupling response is much different, showing a trend towards linear power behavior for all five coil positions, with centered and 8.3 mm offset showing the highest peak

power output. Since power is proportional to squared voltage, this indicates a square-root voltage response and shows that the electrical system becomes saturated for larger mechanical motion. Fig. 4.7 shows a more detailed power response for the lower level excitation. At lower excitation amplitudes, the 16.6 mm offset shows the highest power output. This offset corresponds to the centering of magnet oscillations about the coil's flux peak. As excitation amplitude increases beyond 3 m s^{-2} however, the centered coil becomes more efficient as oscillations in non-peak regions for the offset coil mitigate gains. Fig. 4.8 shows the harmonic content of the electrical response. This illustrates the complexity of the electrical response for nonlinear coupling and mirrors some of the results in Ref. [75]. At low amplitudes, the current response contains only the first few harmonics. However, as amplitude increases, the number and level of harmonics present in the signal increases. This is due to the appearance of the signal as an impulse as the magnet moves quickly across the useful flux region. It is also interesting to note that the harmonics do not grow linearly with the increase in the excitation amplitude. For example, the content of the second harmonic in Fig. 4.8b has minimum and maximum values for the 24.9, 33.2 mm coil offsets, while the 0, 8.3, and 16.6 mm offsets show a saturation of their current level, basically leveling off beyond a certain amplitude.

4.2.4 Electrical circuit optimization

One area for improvement in both constant and nonlinear coupling is circuit optimization for maximum power. Assuming a given coil with given characteristics L, $\hat{\Theta}$, and R_i, the electrical system can be optimized by the resistive load for maximum power output. To find this ideal R_L value, first consider the power equations for linear and nonlinear coupling from Eqs. 4.35 and 4.49. To find the maximum, a

partial derivative with respect to R_L is taken and set to zero giving

$$\frac{\partial P_{\mathrm{L}}}{\partial R_L} = \left(\frac{(L\Omega)^2 + R_i^2 - \hat{R}_L^2}{2\left((L\Omega)^2 + \left(R_i + \hat{R}_L\right)^2\right)^2} \right) L\Omega r^2 = 0\,, \tag{4.50}$$

$$\frac{\partial P_{\mathrm{N}}}{\partial R_L} = \sum_{n=1}^{N} \left(\frac{(Ln\Omega)^2 + R_i^2 - \hat{R}_L^2}{2\left((Ln\Omega)^2 + \left(R_i + \hat{R}_L\right)^2\right)^2} \right) L^2 \left(f_n^2 + g_n^2\right) = 0\,, \tag{4.51}$$

where P_L and P_N are the linear and nonlinear power equations, and $\hat{R}_L$ is the optimum resistive load. Solving for $\hat{R}_L$ in the linear equation gives

$$\hat{R}_L = \sqrt{(L\Omega)^2 + R_i^2}\,. \tag{4.52}$$

Note that $\hat{R}_L$ is a function of the coil inductance, excitation frequency, and internal coil resistance. However, for the low frequency excitation and low coil inductance used for this system, it can be assumed that $R_i^2 >> (L\Omega)^2$, therefore, optimum load for the constant case is $\hat{R}_L \approx R_i$.

The nonlinear case requires a less direct method with similar assumptions. First, Eq. 4.51 can be simplified to

$$\hat{R}_L^2 = R_i^2 + \frac{(L\Omega)^2}{N} \sum_{n=1}^{N} n^2\,, \tag{4.53}$$

by noting that $\left(R_i + \hat{R}_L\right)^2 >> (Ln\Omega)^2$, allowing the denominator to be set as a constant and cancelled, and assuming $L^2\left(f_n^2 + g_n^2\right)$ is constant for all n and can thus be cancelled. Next, recognizing that $R_i^2 >> \frac{(L\Omega)^2}{N}$, the optimum load for the nonlinear circuit can be approximated $\hat{R}_L \approx R_i$. Based on Eq. 4.53 this approximation only deteriorates when N is on the same order of magnitude as the internal resistance.

This deterioration is mitigated by the fact that f_n and g_n generally decrease with increasing n. Figure 4.9 shows the relationship of dimensionless power to resistive load for linear coupling and nonlinear coupling at five coil offsets. The resistive load is normalized by the internal coil resistance $R_i = 125\ \Omega$. The constant and all five nonlinear curves have peak power values at or near one, which corresponds with the theoretical approximation.

4.3 Multiple frequency excitation

This section will examine analytical and numerical solutions for multi-frequency excitation. First, general analytical expressions for linear and nonlinear coupling models will be developed. This will proceed as in Section 4.2 for single-frequency excitation, however with multiple frequency input, i.e., $n > 1$, for Eq. 4.16. The linear coupling analytical methods for multi-frequency input are similar to those for single-frequency input and require only a couple additional steps. However, the nonlinear coupling model for multi-frequency input is more complicated, requiring a different solution form than the single Fourier series approximation used for single-frequency excitation. After the general forms of the solutions are developed, different forms of multi-frequency excitation will be examined. Results will be shown in the form of power to maximum power ratios, with one excitation form including a simulation study for analytical results verification.

4.3.1 Linear coupling

Solutions for linear coupling with multi-frequency input will be found using the principle of superposition. Since the system is linear, the separate excitation frequencies can be treated individually. This means that the stead-state mechanical response for

each frequency is

$$r_n = \frac{\Gamma_n}{\sqrt{\left(2\zeta\omega_0\Omega_n + \frac{\hat{\Theta}^2\Omega_n\rho}{Lm(\rho^2+\Omega_n^2)}\right)^2 + \left(\left(1 - \frac{\hat{\Theta}^2}{Lm(\rho^2+\Omega_n^2)}\right)\Omega_n^2 - \omega_0^2\right)^2}}\,, \tag{4.54}$$

where Ω and Γ have been replaced in the single-frequency case with Ω_n and Γ_n. This can likewise be done with the electrical response to give

$$I_n = \left(\frac{\hat{\Theta}\Omega_n}{L\sqrt{\rho^2+\Omega_n^2}}\right) r_n\,. \tag{4.55}$$

For the total steady-state electrical response, $\bar{I}_n$ is broken down into c_n and d_n components for each frequency, plugged back into the Fourier series for I, and summed to give

$$I = \sum_{n=1}^{N} c_n \sin\Omega_n t + d_n \cos\Omega_n t\,. \tag{4.56}$$

Since a given set of frequencies will not necessarily have an integer multiplicative relationship, average power is calculated by Eq. 4.20.

4.3.2 Nonlinear coupling

Solutions for nonlinear coupling with multi-frequency input will be found similarly to those for single-frequency with changes to account for the more complex electrical response. As with linear coupling, the linear mechanical system response (with the ignored coupling effects) will rely on superposition, treating each excitation function independently. This means that the steady-state mechanical response for each frequency is

$$r_n = \frac{\Gamma_n}{\sqrt{\left(2\zeta\omega_0\Omega_n\right)^2 + \left(\Omega_n^2 - \omega_0^2\right)^2}}\,, \tag{4.57}$$

which break down into a_n and b_n components,

$$a_n = -\frac{\left(\Omega_n^2 - \omega_0^2\right)\Gamma_n}{\left(2\zeta\omega_0\Omega_n\right)^2 + \left(\Omega_n^2 - \omega_0^2\right)^2}\,, \tag{4.58}$$

$$b_n = -\frac{\left(2\zeta\omega_0\Omega_n\right)\Gamma_n}{\left(2\zeta\omega_0\Omega_n\right)^2 + \left(\Omega_n^2 - \omega_0^2\right)^2}\,. \tag{4.59}$$

To find the electrical circuit response, Eq. 4.41 was used so that the coupling term acts as a forcing term for the electrical circuit. Since this forcing will be highly nonlinear, a numerical approach was also taken. For the multi-frequency input, a solution of the form of a truncated Fourier series with no relationship between frequencies is assumed,

$$I = \sum_{n=1}^{N} \left(c_n \sin\hat{\Omega}_n t + d_n \cos\hat{\Omega}_n t\right)\,. \tag{4.60}$$

It is important to note the distinction between the mechanical forcing Ω and the electrical forcing $\hat{\Omega}$, as these angular frequencies may have a limited relationship depending on the type of multi-frequency excitation. Given this assumed solution, analytical solutions for I are most easily found if a Fourier expansion is found of F_{E} in the form

$$F_{\mathrm{E}} = \sum_{n=1}^{N} \left(f_n \sin\hat{\Omega}_n t + g_n \cos\hat{\Omega}_n t\right)\,. \tag{4.61}$$

Since the excitation frequencies have undetermined relationships, f_n and g_n must be calculated using a fast Fourier transform (FFT) of the forcing signal. This FFT provides amplitude and phase information for all frequencies of the given signal. This information can then be deconstructed into f_n and g_n,

$$f_n = -A_{\mathrm{F}} \sin\phi_{\mathrm{F}}\,, \tag{4.62}$$

$$g_n = A_{\mathrm{F}} \cos\phi_{\mathrm{F}}\,, \tag{4.63}$$

where A_{F} and ϕ_{F} are the amplitude and phase of individual frequencies from the FFT data. With this data, the resulting c_n and d_n are found in the same form as the single-frequency case,

$$c_n = \frac{\rho f_n + \hat{\Omega}_n g_n}{\rho^2 + \left(\hat{\Omega}_n\right)^2}, \tag{4.64}$$

$$d_n = \frac{\rho g_n - \hat{\Omega}_n f_n}{\rho^2 + \left(\hat{\Omega}_n\right)^2}. \tag{4.65}$$

For the total steady-state electrical response, these components are plugged back into the Fourier series for I and summed to give

$$I = \sum_{n=1}^{N} c_n \sin \hat{\Omega}_n t + d_n \cos \hat{\Omega}_n t \tag{4.66}$$

. As with the linear case the given set of frequencies will not necessarily have an integer multiplicative relationship, therefore average power is calculated by Eq. 4.20.

4.3.3 Analytical and numerical comparisons

Analytical solutions were generated to investigate three different types of multi-frequency excitation. Simulations were also performed for one type of multi-frequency excitation to provide a basis of validity comparison for the analytical methods of the previous section. For high solution accuracy, the 150 frequencies in the FFT data that had the highest amplitudes were used to generate the solutions for the nonlinear coupling, i.e., $N = 150$ for the I expression. All other parameters used for the analytical and numerical solutions correspond with Tab. 4.1 unless otherwise noted.

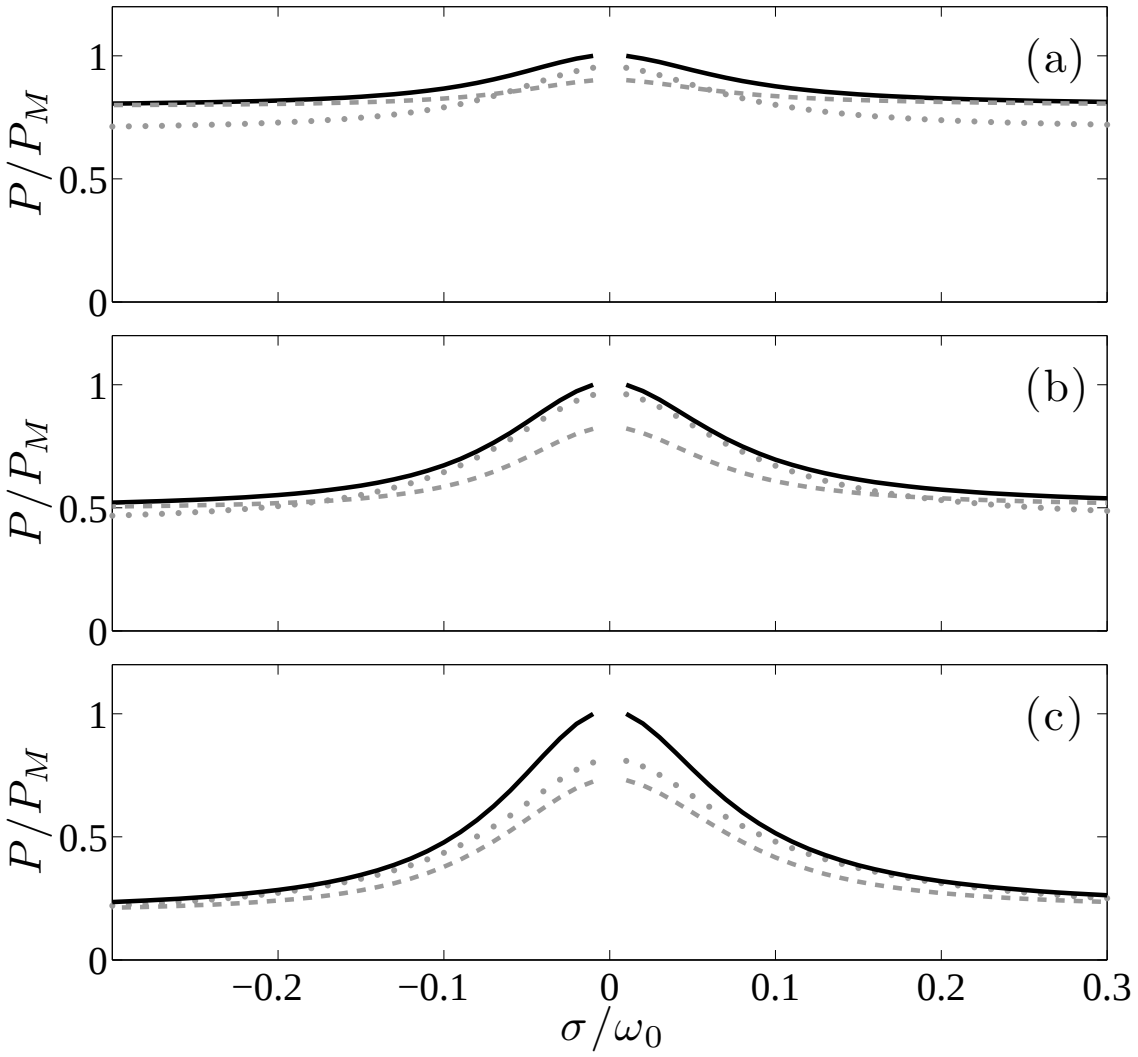

FIGURE 4.10: Dimensionless electrical power vs. offset frequency normalized by the natural frequency with excitation frequencies at the natural frequency and ± offset from the natural frequency. Black represents linear coupling analytical solutions, while grey dotted and dashed lines are nonlinear coupling with coil positioning at $y = 0$ and 16.6 mm, respectively. Offset frequency excitation amplitude = .5, 1, and 2 times the natural frequency excitation amplitude and $P_M = 0.501$, 0.799, and 1.983 mW for graphs (a) - (c).

Resonant and offset frequencies

The first type of excitation included excitation at the natural frequency of the mechanical system and at an offset from that natural frequency, taking the form,

$$\Gamma_1 \sin \omega_0 t + \Gamma_2 \sin (\omega_0 + \sigma) t \,, \tag{4.67}$$

where σ can be a positive or negative offset. For each of the three cases of this type of excitation, Γ_1 was held constant at 2.96 m s^{-2}. This corresponds to the excitation level that produces equal power with constant and nonlinear coupling. In order to look at different behavior, Γ_2 is $.5\Gamma_1$, Γ_1, and $2\Gamma_1$ were the three excitation amplitudes for the second frequency. Examining the results in Fig. 4.10, it is shown that as the amplitude of Γ_2 increases, it contributes more to the total power. For each of the three cases, constant coupling has a higher maximum power and wider effective bandwidth than either of the nonlinear cases.

Positive and negative offset frequencies

The second type of excitation had two frequencies equally offset from the natural frequency,

$$\Gamma_1 \sin (\omega_0 - \sigma) t + \Gamma_2 \sin (\omega_0 + \sigma) t \,. \tag{4.68}$$

For each case of this excitation type, Γ_1 was again held constant at 2.96 m s^{-2}, while the positive offset amplitude Γ_2 is $.5\Gamma_1$, Γ_1, or $2\Gamma_1$. Fig. 4.11 shows the results from this excitation form. Again, the linear case shows a higher peak amplitude at low σ values. However, as σ increases and the excitation frequencies move away from the natural frequency, the $y = 16.6$ mm offset nonlinear coupling has an advantage over the linear coupling for all three excitation levels, but most notably when $\Gamma_2 = .5\Gamma_1$.

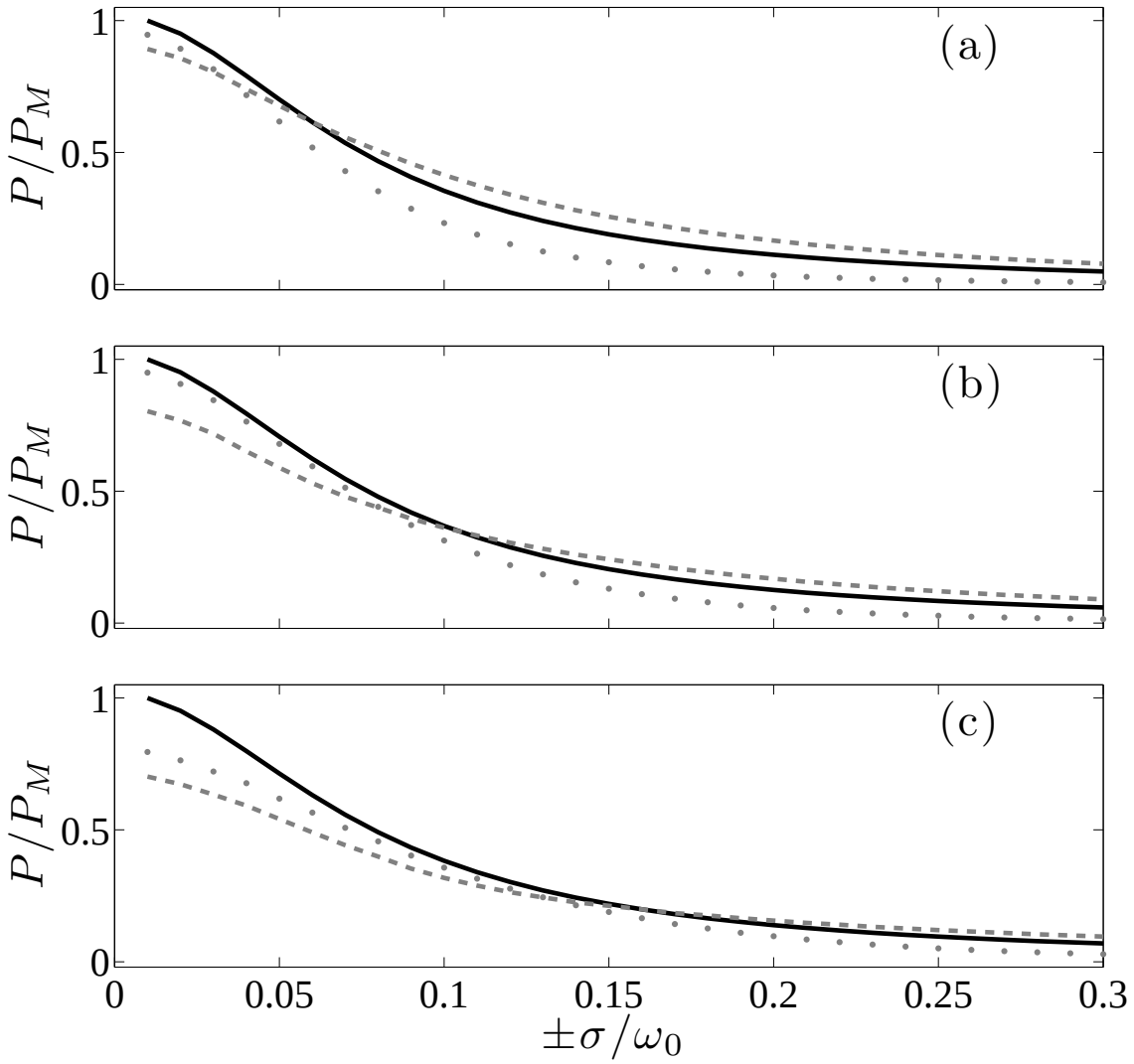

FIGURE 4.11: Dimensionless electrical power vs. offset frequency normalized by the natural frequency with excitation frequencies at a negative and positive offset from the natural frequency. Black represents linear coupling analytical solutions, while grey dotted and dashed lines are nonlinear coupling with coil positioning at $y = 0$ and 16.6 mm, respectively. Positive offset excitation amplitude = .5, 1, and 2 times the negative offset excitation amplitude and $P_M = 0.493$, 0.790, and 1.974 mW for graphs (a) - (c).

Negative offset and integer harmonic frequencies

The final type of excitation had two or three frequencies depending on the case with the first frequency at a negative offset for the natural frequency in both cases. For two frequency excitation, the second frequency was either a second or third harmonic of the resulting offset. The three frequency excitation had both the second and third harmonics of the negative offset frequency. This excitation took the general form

$$\Gamma_1 \sin\left(\omega_0 - \sigma\right) t + \Gamma_2 \sin 2\left(\omega_0 - \sigma\right) t + \Gamma_3 \sin 3\left(\omega_0 - \sigma\right) t\,, \tag{4.69}$$

where either harmonic or both harmonics are present in the excitation form. For each result generation, Γ_1 was held constant at 2.96 m s^{-2}.

For the second harmonic case shown in Fig. 4.12, Γ_2 is $.5\Gamma_1$, Γ_1, or $2\Gamma_1$, while $\Gamma_3 = 0$. Lines in this figure represent analytical results, while symbols represent numerical studies. First note the similarity of analytical and numerical solutions for all three plots and all three coupling models. This illustrates the validity of the analytical techniques used to derive the solutions. For all three graphs, the peak at $\sigma = -0.5$ corresponds to the second harmonic equalling the natural frequency. For the lowest Γ_2 level, the $y = 16.6$ mm offset nonlinear coupling shows the most gains over linear coupling across the entire offset range. As Γ_2 increases, linear coupling models produce more power when one of the frequencies is at or near ω_0, however the intermittent offset frequencies still show gains for the $y = 16.6$ mm offset nonlinear coupling.

For the third harmonic case shown in Fig. 4.13, $\Gamma_2 = 0$, while Γ_3 is $.5\Gamma_1$, Γ_1, or $2\Gamma_1$. This case shows similar results to the second harmonic, namely that peak power is produced when one or both of the excitation frequencies are near the mechanical system natural frequency. At low second frequency amplitude, the $y = 16.6$ mm offset nonlinear coupling shows improvement over the linear system across all offset frequencies, with the largest gains produced when one of the two frequencies is equal

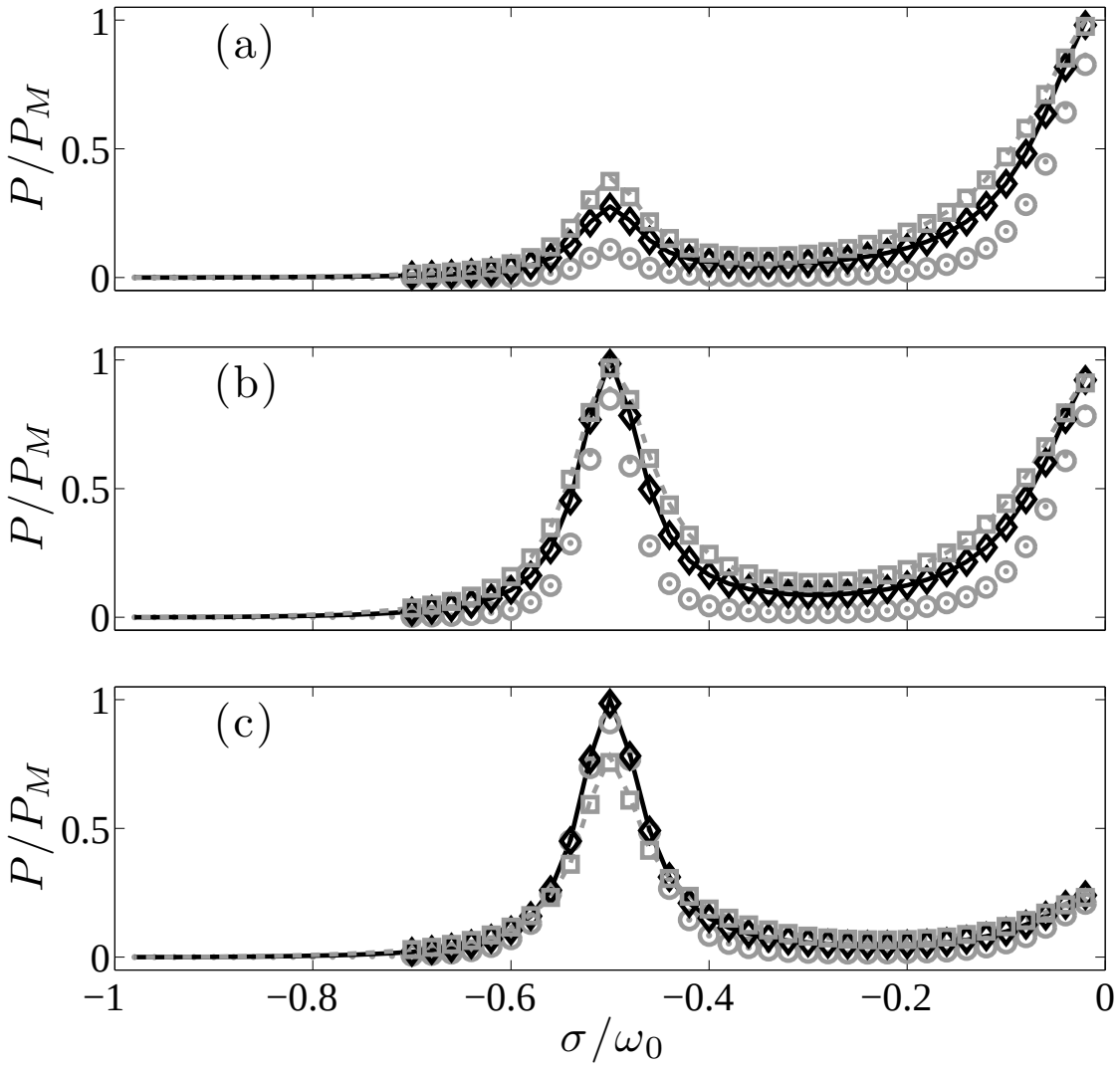

FIGURE 4.12: Dimensionless electrical power vs. offset frequency normalized by the natural frequency with excitation frequencies at a negative offset from the natural frequency and the second harmonic of the offset. Black represents linear coupling analytical solutions, while grey dotted and dashed lines are nonlinear coupling with coil positioning at $y = 0$ and 16.6 mm, respectively. Numerical simulations are represented by black squares and grey circles and squares for linear coupling and nonlinear coupling with coil positioning at $y = 0$ and 16.6 mm, respectively. Second harmonic excitation amplitude = .5, 1, and 2 times the negative offset excitation amplitude and $P_M = 0.376$, 0.404, and 1.602 mW for graphs (a) - (c).

to the natural frequency. Again, at larger Γ_3, the linear coupling produces more power, while the gains for nonlinear coupling are less in the intermittent frequencies than they were for the second harmonic case.

For the final case with both the second and third harmonics along with the offset, the system was explored with two different amplitude trends. The first has $\Gamma_2 = \Gamma_3 = .5\Gamma_1$, Γ_1, or $2\Gamma_1$. The results are shown in Fig. 4.14. For this case, the linear coupling model shows the highest power levels across all frequencies, with the $y = 16.6$ mm offset nonlinear coupling model having the lowest efficiency. The $y = 0$ mm offset model shows power levels near that of linear coupling for any of the excitation frequencies at or near the natural frequency and higher harmonic excitation amplitudes. The other trend explored in Fig. 4.15 shows cases where $\Gamma_2 \neq \Gamma_3$. The results here are similar to those in Fig. 4.14. Linear coupling has the highest power for all four amplitude configurations across all offsets and the $y = 16.6$ mm offset has the lowest power for all four. Likewise, the $y = 0$ mm offset has similar power levels to that of the linear coupling. This similarity is somewhat selective, as power levels are much closer for the higher excitation amplitudes in the lower plots and much farther for the lower excitation amplitude when the smaller of the two frequencies is near the natural frequency.

4.4 Conclusions

This chapter investigated the response behavior of an energy harvester that uses electromagnetic induction to convert ambient vibration into electrical energy. Furthermore, this chapter explored the system's response behavior when either a linear or a physically motivated form of nonlinear coupling was applied. The derived form of the nonlinear model was found to be consistent with those produced produced by other authors, such as Refs. [3, 75] with peak flux regions offset from the center. Approximate analytical solutions were derived for single-frequency excitation

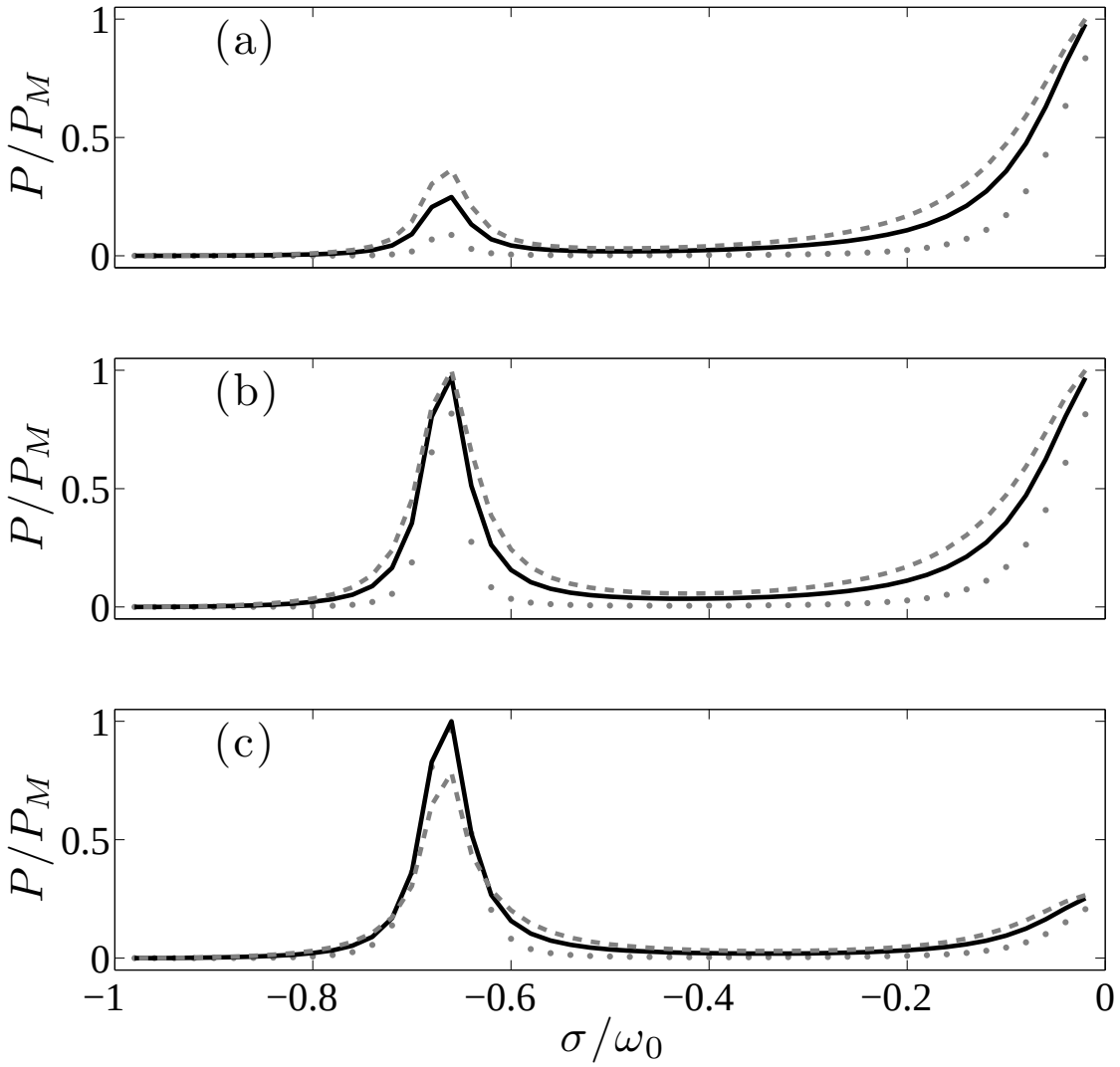

FIGURE 4.13: Dimensionless electrical power vs. offset frequency normalized by the natural frequency with excitation frequencies at a negative offset from the natural frequency and the third harmonic of the offset. Black represents linear coupling analytical solutions, while grey dotted and dashed lines are nonlinear coupling with coil positioning at $y = 0$ and 16.6 mm, respectively. Third harmonic excitation amplitude = .5, 1, and 2 times the negative offset excitation amplitude and P_M = 0.382, 0.387, and 1.497 mW for graphs (a) - (c).

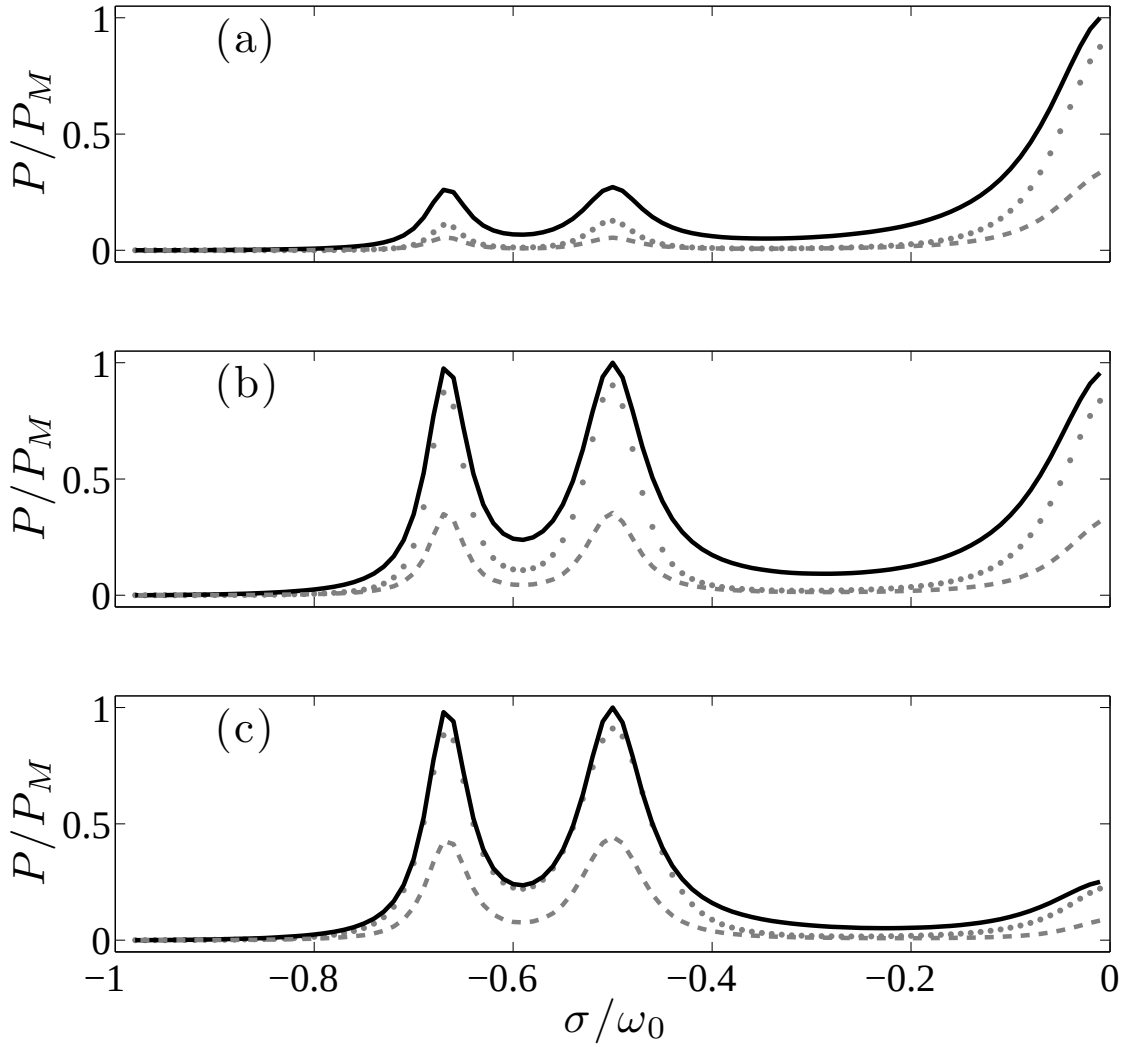

FIGURE 4.14: Dimensionless electrical power vs. offset frequency normalized by the natural frequency with excitation frequencies at a negative offset from the natural frequency and the second and third harmonic of the offset. Black represents linear coupling analytical solutions, while grey dotted and dashed lines are nonlinear coupling with coil positioning at $y = 0$ and 16.6 mm, respectively. Second and third harmonic excitation amplitude = .5, 1, and 2 times the negative offset excitation amplitude and $P_M = 0.394$, 0.417, and 1.654 mW for graphs (a) - (c).

using Harmonic Balance; the predictions from the approximate analytical solutions were found to favorably correlate with the results of numerical simulations. Linear coupling showed a theoretically higher peak (at mechanical resonance) power output over the nonlinear model for all coil offsets at excitation amplitudes above 5 m s^{-2}. This was the result of electrical system saturation for all nonlinear models as magnet oscillations increased into regions of negligible coil flux. While this points to the benefit of the linear coupling for single-frequency excitation, note that the linear model is physically unrealistic for this type of electromagnetic generator, i.e., due to space limitations. At lower excitation amplitudes (< 5 m s^{-2}), a coil offset, one that placed the peak flux at the oscillation center ($y = 16.6$ mm), was found to have the highest power output – illustrating its usefulness in applications where excitation amplitude is expected to be below a given level. Additionally, as Γ was increased, higher harmonics appeared in the current response, requiring more terms to accurately capture the true response of the system; this illustrates the more complex behavior that is an outcome of the nonlinear coupling model.

Electrical circuit optimization was also found to correlate well with the values obtained from the approximate analytical solutions. For the given system parameters, both the linear and all nonlinear coupling models showed that the peak power was produced when the resistance of the load matched the internal resistance of the coil.

Multi-frequency excitation was also investigated analytically – thus requiring a hybrid analytical/numerical approach to be taken for the nonlinear coupling model. Three different excitation types were explored with either two or three input frequencies. The first included excitation at the natural frequency and an offset from that frequency. For this excitation, the linear model showed a wider band of useful offset frequencies for all levels of the second frequency excitation. The second excitation type with both the first and second frequencies at an offset above and below the

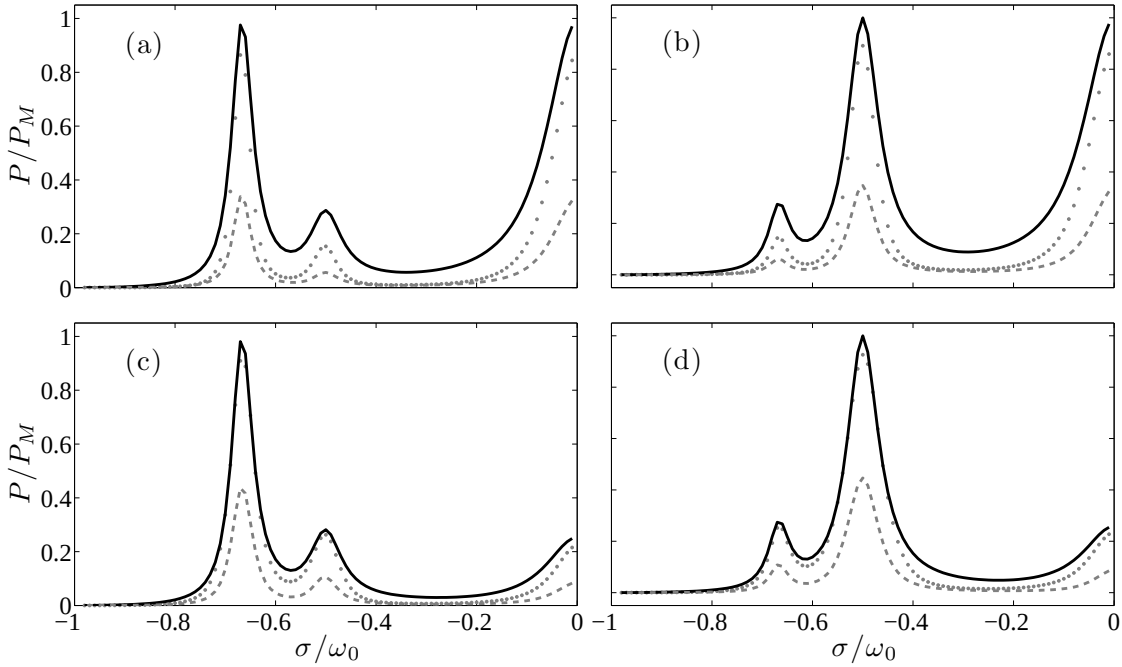

FIGURE 4.15: Dimensionless electrical power vs. offset frequency normalized by the natural frequency with excitation frequencies at a negative offset from the natural frequency and the second and third harmonic of the offset. Black represents linear coupling analytical solutions, while grey dotted and dashed lines are nonlinear coupling with coil positioning at $y = 0$ and 16.6 mm, respectively. For (a) $\Gamma_2 = \Gamma_1/2$ and $\Gamma_3 = \Gamma_1$, (b) $\Gamma_2 = \Gamma_1$ and $\Gamma_3 = \Gamma_1/2$, (c) $\Gamma_2 = \Gamma_1$ and $\Gamma_3 = 2\Gamma_1$, and (d) $\Gamma_2 = 2\Gamma_1$ and $\Gamma_3 = \Gamma_1$. $P_M = 0.407$, 0.407, 1.615, and 1.615 mW for graphs (a) - (d).

system natural frequency showed a similar linear coupling advantage however not over all frequencies. As the offset from ω_0 was increased, the $y = 16.6$ mm offset nonlinear coupling produced higher power levels, especially at lower excitation amplitudes. Although this increase is small, it shows potential for nonlinear coupling in systems where the dominant frequency has a high level of variability.

The last excitation type shows the most promise for nonlinear coupling over linear coupling. At low excitation amplitude for either the second or third harmonic of the offset frequency, nonlinear shows large gains over linear coupling for the $y = 16.6$ mm offset across all offset frequencies and most significantly when the second or

third harmonic is at ω_0. This power increase shows the benefit for nonlinear coupling in systems where one lower amplitude harmonic is likely to be present and the dominant frequency has a degree of uncertainty. However, for the cases where there is both the second and third harmonic present, these gains are eliminated for the $y = 16.6$ mm offset. However, for higher excitation levels, in the case where both harmonics are present, the centered-coil model provides similar power levels to that of linear coupling. One possible use for this behavior would be adjustable coils in an environment with many different harmonic excitation forms. At low amplitudes when only the second or third harmonic present, the coil would be most useful offset at $y = 16.6$ mm. As excitation amplitude increased or another harmonic became more prevalent in the environment, the coil positioning could switch, allowing for more efficient power generation. Numerical simulations, executed for the second harmonic case, also illustrated the accuracy of the analytical techniques used to find multi-frequency solutions. These investigations not only highlight the detriments and benefits of nonlinear electromagnetic coupling, but also form a base for further exploration of more diverse energy scavenging systems and complex vibration environments.

5

Two beam system with a bistability from magnetic coupling

Vibration energy harvesting has grown over the past decade with researchers exploring a variety of ideas to fulfill the need for small-scale, portable power generation [2, 68, 86–89]. Early research designed systems that had to be tailored to a specific environment, focusing on linear resonant optimization design [90–92]. Recent progress has been made in the way of broadband harvesters with stochastic, multi-frequency, and frequency shifting environments, paving the way for the emergence of nonlinear energy harvesters [9, 13, 16, 93] and multiple degree-of-freedom [19, 94, 95] harvesters alike.

One class of systems explored has been the bistable Duffing oscillator [13, 16]. This single degree-of-freedom oscillator has shown promise for broadband energy harvesting and efficacy in multi-frequency environments [66]. Oscillations have regions of high energy, well mixing chaotic behavior, as well as coexisting periodic well mixing solutions and low energy intrawell solutions. The intrawell behavior shows a softening dynamic, while the large, well mixing behavior has a hardening signature.

These well mixing transitions are high energy interactions, with larger velocity than the intrawell solutions.

Explorations of transduction methods, such as electromagnetic [9], and simple electrical harvesting circuits indicate that in the case of linear coupling, electrical circuitry driving voltage scales with the system velocity. Taking a step further, if the inductive effects of the coil are ignored, electrical power is proportional to the square of the velocity. Additionally, for low levels of coil induction, the electrical force on the mechanical system comes in the form of electrical damping, scaling with the velocity much like mechanical viscous damping. In this system, only the mechanical system is modeled, analyzed, and tested. Parallels to the energy harvesting potential of the device are derived from the assumption of linear transduction, low inductance in the proposed electrical system, and a combined electrical and mechanical viscous damping. To this end, the power comparison term will be the squared velocity of the oscillators. Additional considerations for a harvesting system such as voltage rectification are highlighted in the body of the chapter.

This chapter considers a two degree of freedom mechanical system with bistability created from the oscillator magnetic tip interactions or coupling. The investigation focuses primarily on the phenomenologically richness of the system with considerations for a theoretical power harvesting configuration. Magnetic tip masses are added to two cantilever beams and oriented so as to induce a magnetic repulsion force. This repulsion, given the proper parameters of the system, creates a mechanical dual-well potential energy. Exploration of the multiple attractors is detailed as they exist across the broad excitation parameter space.

First, governing equations modeled to mimic the physical behavior are derived from energy expressions. Numerical time-marching investigations are then used to discover the unique interwell and intrawell vibrations, period doubling cascades, subharmonic oscillations, in and out of phase oscillations, and chaotic behavior. This

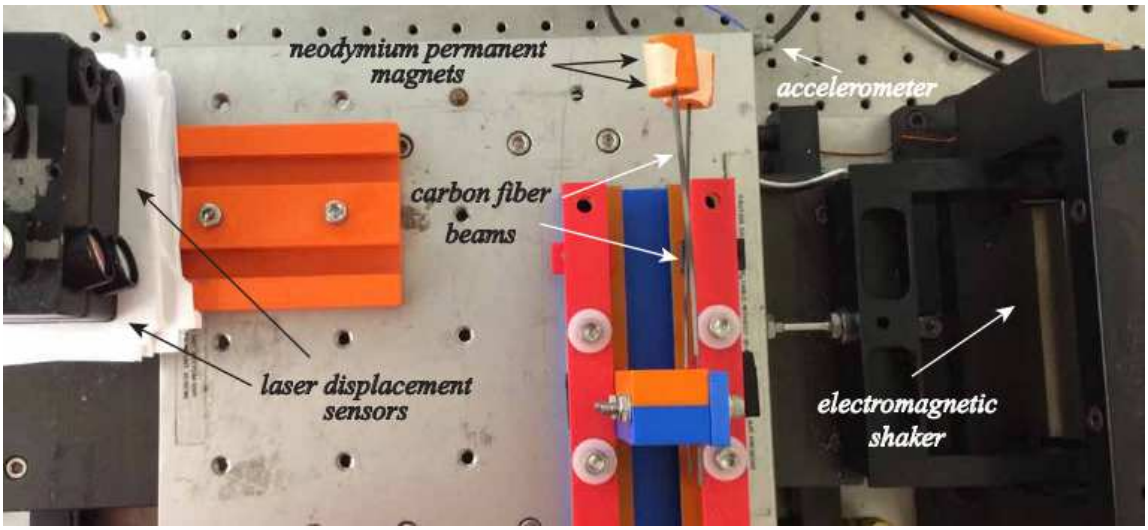

FIGURE 5.1: Experimental system image showing the measurement and excitation equipment. Beam displacements were measured with laser displacement sensors and the the shaker table acceleration was measured with a single-axis accelerometer.

behavior will also be viewed from a power harvesting perspective to draw realistic comparisons for the energy harvesting capability of the system. This exploration is then mirrored in the experimental system, serving to validate the existence of unique phenomenological behavior and validate the power considerations for energy harvesting.

This chapter is structured as follows. Section 5.1 illustrates the two degree of freedom bistable system and details the energy based equation of motion derivation. The next section discusses the numerical investigations from time-marching simulations, including parameter sweeps and specific phenomena demonstrations. Section 5.3 details experimental results to validate phenomenological existence. Conclusions and discussions are in the final section.

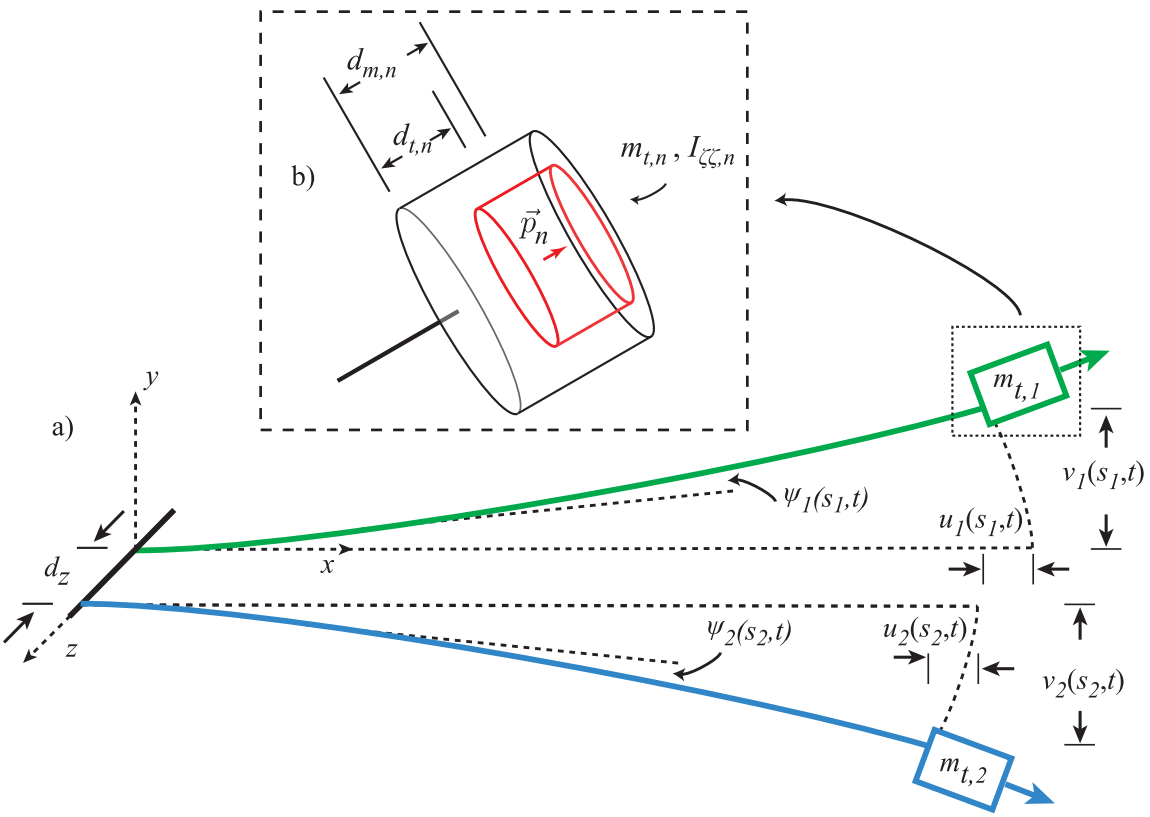

FIGURE 5.2: Schematic diagram of a two cantilever beam system with tip masses shown in a bistable configuration a) and a detailed diagram of the tip mass geometry (inset b).

5.1 Magnetically coupled two beam system

An image of the experimental apparatus is shown in Fig. 5.1. The system consists of two cantilevered carbon fiber beams with attached magnetic tip masses. The tip masses are made up of neodymium permanent magnets in a casing that offsets them from the tips of their respective beams. The magnets are oriented with aligned polarity so as to generate a nonlinear repulsive force. Inside a critical separation distance, this repulsive force overcomes the restoring force of the elastic beams and forces a static deflection of the beams in opposite directions. In this configuration, each beam is bistable with opposite directional stability. Figure 5.2 shows a diagram

of the experimental system along with the relevant dimensions. Parameters for the physical system are listed in Table 5.1. The beams were attached to a shaker table that provided the oscillatory environment. Also attached to the table were a set of laser displacement sensors (Microepsilon OptoNCDT LD 1605-100) was used to measure the oscillations of the beam tips and an accelerometer (PCB Piezotronics something or other) to measure the base acceleration. The signals then went through a high-pass filter to eliminate electrical signal noise from the surrounding electronics before being measured by the data acquisition equipment.

To develop an adequate model for the dynamic behavior of this bistable system, it is presumed that deflections are large enough to constitute a third order nonlinear beam approximation. This is derived primarily from Ref. [70].

5.1.1 Cantilever beam expressions

The n-th beam, where $n = 1$ represents the first beam and $n = 2$ the second, have kinetic energy

$$T_{B,n} = \frac{1}{2}\int_0^{L_n} m_{l,n}\left(\dot{u}_n^2 + (\dot{v}_n + \dot{v}_b)^2\right) ds_n \,. \tag{5.1}$$

where L_n is the length of the n-th beam, $u_n(s_n, t)$ is an axial oscillation in the global x direction, $v_n(s_n, t)$ is a transverse oscillation in the global y direction, $v_b(t)$ is the prescribed excitation of the base, $m_{l,n}$ is the mass per unit length, and s_n is the arc length coordinate along the beam. An overdot indicates a time derivative. The system also has kinetic energy associated with translations and rotations of the rigid body tip mass

$$T_{T,n} = \frac{1}{2} m_{t,n}\, \dot{\vec{r}}_{T,n} \cdot \dot{\vec{r}}_{T,n} + \frac{1}{2} I_{\zeta\zeta,n}\, \dot{\psi}_n(L_n, t)^2 \,, \tag{5.2}$$

where the rotational inertia of the mass about the tip of the beam is $I_{\zeta\zeta,n}$, the angular velocity at the tip is $\dot{\psi}_n(L_n, t)$, and the position vector $\dot{\vec{r}}_{T,n}$ is illustrated in Fig. 5.2

to be

$$\vec{r}_{T,n}(t) = \begin{bmatrix} L_n + u_n(L_n,t) + d_{t,n}\cos\psi_n(L_n,t) \\ v_n(L_n,t) + d_{t,n}\sin\psi_n(L_n,t) + v_b(t) \\ 0 \end{bmatrix}, \tag{5.3}$$

where the center of mass offset distance from the tip of the beam is $d_{t,n}$. The potential energy of the beam is the result of internal strain energy in the material and is an expression of the beam curvature

$$V_{B,n} = \frac{1}{2}\int_0^{L_n} EI_{\zeta,n}\psi_n'^2(s_n,t)\,ds_n\,, \tag{5.4}$$

where $\psi_n'(s_n,t)$ is the curvature or the spatial angle change over the length of the beam, E is the elastic modulus of the beam material, and $I_{\zeta,n}$ is the second moment of inertia for the beam cross-section about the central axis of bending.

Given the fully nonlinear beam expressions, simplification of the energies to fourth order allows for third order nonlinearities to persist in the equations of motion. First, it is assumed that the beams are inextensible such that

$$(1+u_n')^2 + v_n'^2 = 1\,, \tag{5.5}$$

where the prime ($'$) symbol is a spatial derivative. Given this condition, angular beam rotations are related to translational oscillations by

$$\tan\psi_n = \frac{v_n'}{1+u_n'}\,. \tag{5.6}$$

This constraint also allows for an approximation of the axial oscillations. First, consider transverse oscillations and first spatial derivatives to have order ϵ magnitude, where $\epsilon << 1$. With Eq. 5.5, ϵ^4 order substitutions are derived

$$u_n' \approx -\frac{1}{2}\epsilon^2\, v_n'^2 - \frac{1}{8}\epsilon^4\, v_n'^4 \quad \text{and} \quad u_n \approx -\frac{1}{2}\epsilon^2\int_0^{s_n} v_n'^2\,ds_n - \frac{1}{8}\epsilon^4\int_0^{s_n} v_n'^4\,ds_n\,. \tag{5.7}$$

With incorporation of angle and axial approximations into energy expressions in Eqs. 5.1 - 5.4 and elimination of higher order terms, the beam energy expressions become

$$T_{B,n} = \frac{1}{2}\int_0^{L_n} m_{l,n}\left(\frac{1}{4}\left(\frac{\partial}{\partial t}\int_0^{s_n} v_n'^2\, ds_n\right)^2 + \left(\dot{v}_n + \dot{v}_b\right)^2\right) ds_n\,, \tag{5.8}$$

$$T_{T,n} = \frac{1}{2}m_{t,n}\left(\left(\frac{1}{2}\frac{\partial}{\partial t}\int_0^{s_n} v_n'^2\, ds_n + d_{t,n}v_n'\dot{v}_n'\right)^2 + \left(\dot{v}_1 + \dot{v}_b + d_{t,n}\dot{v}_n'\right)^2\right) + \frac{1}{2}I_{\zeta\zeta,n}\left(\dot{v}_n'^2\left(1 + v_n'^2\right)\right), \tag{5.9}$$

$$V_{B,n} = \frac{1}{2}\int_0^{L_n} E\, I_{\zeta,n}\left(v_n''^2\left(1 + v_n'^2\right)\right) ds_n\,. \tag{5.10}$$

The last energy expression is the potential energy of the magnet interactions and is derived in the next subsection.

5.1.2 Magnetic potential energy

Figure 5.2 illustrates the important magnet variables and the geometry of the system. For a system of two magnets, modeled as dipoles with magnetization concentrated at a single point, the potential energy [40, 41] of magnet 1 as a result of the field generated by magnet 2 is

$$U_M = -\vec{p}_1 \cdot \vec{B}_{21} = \vec{p}_1 \cdot \left(\frac{\mu_0}{4\pi}\left(\frac{\vec{p}_2}{|\vec{r}_{21}|^3} - \left(\vec{p}_2 \cdot \vec{r}_{21}\right)\frac{3\vec{r}_{21}}{|\vec{r}_{21}|^5}\right)\right). \tag{5.11}$$

where $\vec{r}_{21}$ is a vector from magnet 2 to magnet 1, $\vec{p}_2$ is the magnetic moment of magnet 2, $\vec{p}_1$ is the magnetic moment of magnet 1 , and $\mu_0 = 4\pi \times 10^{-7}$ H/m is the permeability of free space. As shown in Fig. 5.2, in this system each magnet sits at the end of its beam with a center $d_{m,n}$ from the tip of the beam and the two beams

are separated d_z at their bases. The resulting position vectors are

$$\vec{r}_1(t) = \begin{bmatrix} L_1 + u_1(L_1,t) + d_{m,1}\cos\psi_1(L_1,t) \\ v_1(L_1,t) + d_{m,1}\sin\psi_1(L_1,t) + v_b(t) \\ 0 \end{bmatrix} \tag{5.12}$$

$$\text{and} \qquad \vec{r}_2(t) = \begin{bmatrix} L_2 + u_2(L_2,t) + d_{m,2}\cos\psi_2(L_2,t) \\ v_2(L_2,t) + d_{m,2}\sin\psi_2(L_2,t) + v_b(t) \\ d_z \end{bmatrix} . \tag{5.13}$$

With the inexstensible condition and the assumption that $d_{m,1} = d_{m,2}$, the separation vector between the two magnets becomes

$$\vec{r}_{21} = \vec{r}_1 - \vec{r}_2 = \begin{bmatrix} L_1 - L_2 + u_1(L_1,t) - u_2(L_2,t) + d_m\Big(\sqrt{1-v_1'(L_1,t)^2} - \sqrt{1-v_2'(L_2,t)^2}\Big) \\ v_1(L_1,t) - v_2(L_2,t) + d_m\Big(v_1'(L_1,t) - v_2'(L_2,t)\Big) \\ -d_z \end{bmatrix} . \tag{5.14}$$

The magnetization vectors are $\vec{p} = \vec{P}\hat{v}$ where $\hat{v}$ is volume of the magnet and $\vec{P}$ is the magnetization per unit volume vector. Figure 5.2 shows the magnetization vectors of the magnets in the direction of the beam tip angle $\psi_n(L_n,t)$. With substitution of the inexstensibility constraint, the two magnetization vectors are

$$\vec{p}_n = |P|\hat{v}_n \begin{bmatrix} \sqrt{1-v_n'(L_n,t)^2} \\ v_n'(L_n,t) \\ 0 \end{bmatrix} . \tag{5.15}$$

The substitution of Eqs. 5.14 and 5.15 into Eq. 5.11 results in a highly nonlinear expression for the magnetic energy between the two tip magnets.

5.1.3 Single mode equations of motion

From the energy expressions, the Lagrangian for the system is defined as a difference between the kinetic and potential energies

$$\mathcal{L} = T_B + T_T - V_B - U_M . \tag{5.16}$$

In order to find the set of governing equations for the two beam system, Hamilton's principle could be applied with variations of the transverse vibrations. Instead, it is simpler to presume that base excitation will be near the first mode natural frequencies of the beams. This allows for a modal expansion of the transverse vibrations into a single term

$$v_n(s_n, t) = V_n(s_n)\, q_n(t) \tag{5.17}$$

instead of a finite sum of N generalized coordinates and orthogonal modes. The generalized, time-varying coordinate is $q_n(t)$ and the mode shape is V_n. To computationally simplify the analysis, the assumed mode shape V_n is taken to be $V_n = (s_n/L_n)^2$, which satisfies the geometric boundary conditions of the cantilevered beams and is unity at $s_n = L_n$.

With substitution of Eq. 5.17 into energy expressions in Eqs. 5.8 - 5.10, lumped parameter equations for the beam energies are derived, starting with the kinetic energy of the beam,

$$\begin{aligned} T_B = &\frac{1}{2}M_{B,1}\dot{q}_1^2 + \frac{1}{2}N_{B,1}q_1^2\dot{q}_1^2 + F_{B,1}\dot{q}_1\dot{v}_b \\ &+ \frac{1}{2}M_{B,2}\dot{q}_2^2 + \frac{1}{2}N_{B,2}q_2^2\dot{q}_2^2 + F_{B,2}\dot{q}_2\dot{v}_b + \frac{1}{2}\left(Z_{B,1} + Z_{B,2}\right)\dot{v}_b^2\,, \end{aligned} \tag{5.18}$$

with parameters

$$M_{B,n} = m_{l,n}\int_0^{L_n} V_n^2 ds_n, \tag{5.19}$$

$$N_{B,n} = m_{l,n}\int_0^{L_n}\left(\int_0^{s_n} V_n'^2 ds_n\right)^2 ds_n, \tag{5.20}$$

$$F_{B,n} = m_{l,n}\int_0^{L_n} V_n ds_n \tag{5.21}$$

$$Z_{B,n} = m_{l,n}L_n\,, \tag{5.22}$$

and the kinetic energy of the rigid body tip mass

$$\begin{aligned} T_T = &\frac{1}{2}M_{T,1}\dot{q}_1^2 + \frac{1}{2}N_{T,1}q_1^2\dot{q}_1^2 + F_{T,1}\dot{q}_1\dot{v}_b \\ &+ \frac{1}{2}M_{T,2}\dot{q}_2^2 + \frac{1}{2}N_{T,2}q_2^2\dot{q}_2^2 + F_{T,2}\dot{q}_2\dot{v}_b + \frac{1}{2}\left(Z_{T,1} + Z_{T,2}\right)\dot{v}_b^2 \,, \end{aligned} \tag{5.23}$$

with parameters evaluated at $s_n = L_n$

$$M_{T,n} = m_{t,n}\left(V_n + d_{t,n}V_n'\right)^2 + I_{\zeta\zeta,n}V_n'^2 \tag{5.24}$$

$$N_{T,n} = m_{t,n}\left(\int_0^{s_n} V_n'^2\, ds_n + d_{t,n}V_n'^2\right)^2 + I_{\zeta\zeta,n}V_n'^4 \tag{5.25}$$

$$F_{T,n} = m_{t,n}\left(V_n + d_{t,n}V_n'\right) \tag{5.26}$$

$$Z_{T,n} = m_{t,n}\,, \tag{5.27}$$

and finally, the beam potential energy

$$V_B = \frac{1}{4}K_{A,1}q_1^4 + \frac{1}{2}K_{B,1}q_1^2 + \frac{1}{4}K_{A,2}q_2^4 + \frac{1}{2}K_{B,2}q_2^2\,, \tag{5.28}$$

using parameters

$$K_{A,n} = 2EI_{\zeta,n}\int_0^{L_n} V_n'^2 V_n''^2 ds_n \tag{5.29}$$

$$K_{B,n} = EI_{\zeta,n}\int_0^{L_n} V_n''^2 ds_n\,. \tag{5.30}$$

With substitution of Eqs. 5.18 - 5.28, Eq. 5.16 becomes the lumped parameter Lagrangian

$$\begin{aligned} \mathcal{L} = &\frac{1}{2}M_1\dot{q}_1^2 + \frac{1}{2}N_1q_1^2\dot{q}_1^2 + F_1\dot{q}_1\dot{v}_b + \frac{1}{2}M_2\dot{q}_2^2 + \frac{1}{2}N_2q_2^2\dot{q}_2^2 + F_2\dot{q}_2\dot{v}_b + \frac{1}{2}\left(Z_1 + Z_2\right)\dot{v}_b^2 \\ &- \frac{1}{4}K_{A,1}q_1^4 - \frac{1}{2}K_{B,1}q_1^2 - \frac{1}{4}K_{A,2}q_2^4 - \frac{1}{2}K_{B,2}q_2^2 - U_M(q_1, q_2) \end{aligned} \tag{5.31}$$

having combined constants $M_n = M_{B,n} + M_{T,n}$, $N_n = N_{B,n} + N_{T,n}$, $F_n = F_{B,n} + F_{T,n}$, and $Z_n = Z_{B,n} + Z_{T,n}$.

Table 5.1: System parameters for numerical studies.

Parameter	Value	Units
Carbon fiber modulus of elasticity, E	65	GPa
Linear mass density, $m_{l,1}$, $m_{l,2}$	7.52 , 9.88	g/m
Beam length, L_1 , L_2	103.3	mm
Beam natural frequency, ω_1, ω_2	10.94, 8.71	Hz
Viscous damping constant, Q_m	0.0289	N·s/m
Second moment of inertia, $I_{\zeta,1}$, $I_{\zeta,2}$	0.526, 0.335	mm^4
Beam tip to center of tip mass, $d_{t,1}$, $d_{t,2}$	12.1	mm
Beam tip to center of magnet, $d_{m,1}$, $d_{m,2}$	13.2	mm
Tip mass rotational inertia, $I_{\zeta\zeta,1}$, $I_{\zeta\zeta,2}$	2890	g/mm^2
Magnetization, $\|P\|$, Br/ μ_0	$1.05/(4\pi \times 10^{-7})$	T / (H/m)
Magnet volume, $\hat{v}_1$, $\hat{v}_2$	1608.8	mm^3
Beam separation distance, d_z	2.22	cm

The Euler-Lagrange equations with the two generalized coordinates q_1 and q_2 and form

$$\frac{d}{dt}\left(\frac{\partial \mathcal{L}}{\partial \dot{q}_1}\right) - \frac{\partial \mathcal{L}}{\partial q_1} = Q_1 \quad \text{and} \quad \frac{d}{dt}\left(\frac{\partial \mathcal{L}}{\partial \dot{q}_2}\right) - \frac{\partial \mathcal{L}}{\partial q_2} = Q_2 \tag{5.32}$$

are then applied to the Lagrangian to derive a system of ordinary differential equations. The generalized force terms Q_1 and Q_2 are defined by nonconservative work functions, which in this case is a combined modal damping force with linear viscous damping

$$Q_n = \text{-}Q_m \dot{q}_n \,. \tag{5.33}$$

With substitution of the Lagrangian and generalized force terms into Eq. 5.32, the fully dimensional governing equations are

$$M_1\ddot{q}_1 + N_1 q_1\left(\dot{q}_1^2 + q_1\ddot{q}_1\right) + Q_m\dot{q}_1 + K_{B,1}q_1 + K_{A,1}q_1^3 + \frac{\partial U_M}{\partial q_1} = -F_1\ddot{v}_b \tag{5.34}$$

$$M_2\ddot{q}_2 + N_2 q_2\left(\dot{q}_2^2 + q_2\ddot{q}_2\right) + Q_m\dot{q}_2 + K_{B,2}q_2 + K_{A,2}q_2^3 + \frac{\partial U_M}{\partial q_2} = -F_2\ddot{v}_b \,. \tag{5.35}$$

Note the third order nonlinearity for inertial, and elastic interactions. The magnetic forces add an additional nonlinearity that couples the two beams. This system has

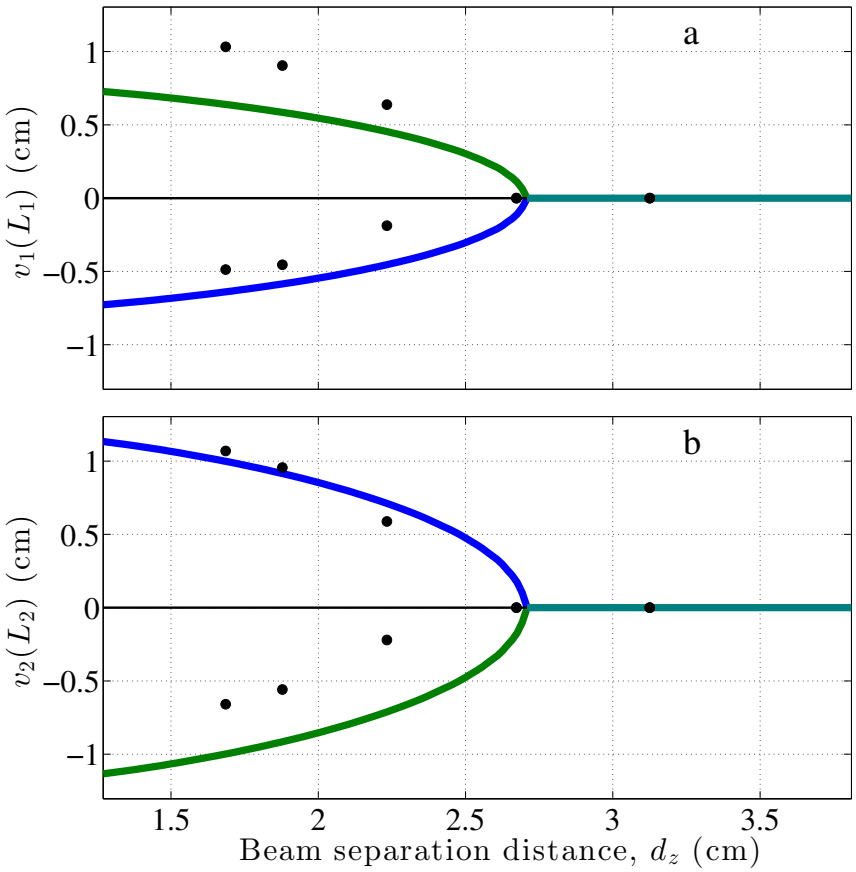

FIGURE 5.3: Bifurcation diagrams for static tip deflection of beam 1 a) and beam 2 b) with the beam separation distance d_z as the bifurcation parameter. The thick blue, green, and teal lines indicate different corresponding sets of stable solutions, while a thin (black) line indicates unstable solutions. Circles show symmetry breaking bifurcation of experimental results . The other system parameters used are in Table 5.1.

two dimensional deflections with q_1 and q_2, but is four dimensional in the state space $(q_1, q_2, \dot{q}_1, \dot{q}_2)$.

5.1.4 Unforced behavior

Using Eqs. 5.34 and 5.35 and the nonlinear magnetic interactions with system parameters in Table 5.1, fixed point bifurcation diagrams are generated in Fig. 5.3. In addition, the theoretical results are shown with experimental tests in order to compare the experimental and theoretical models. These diagrams show that changes

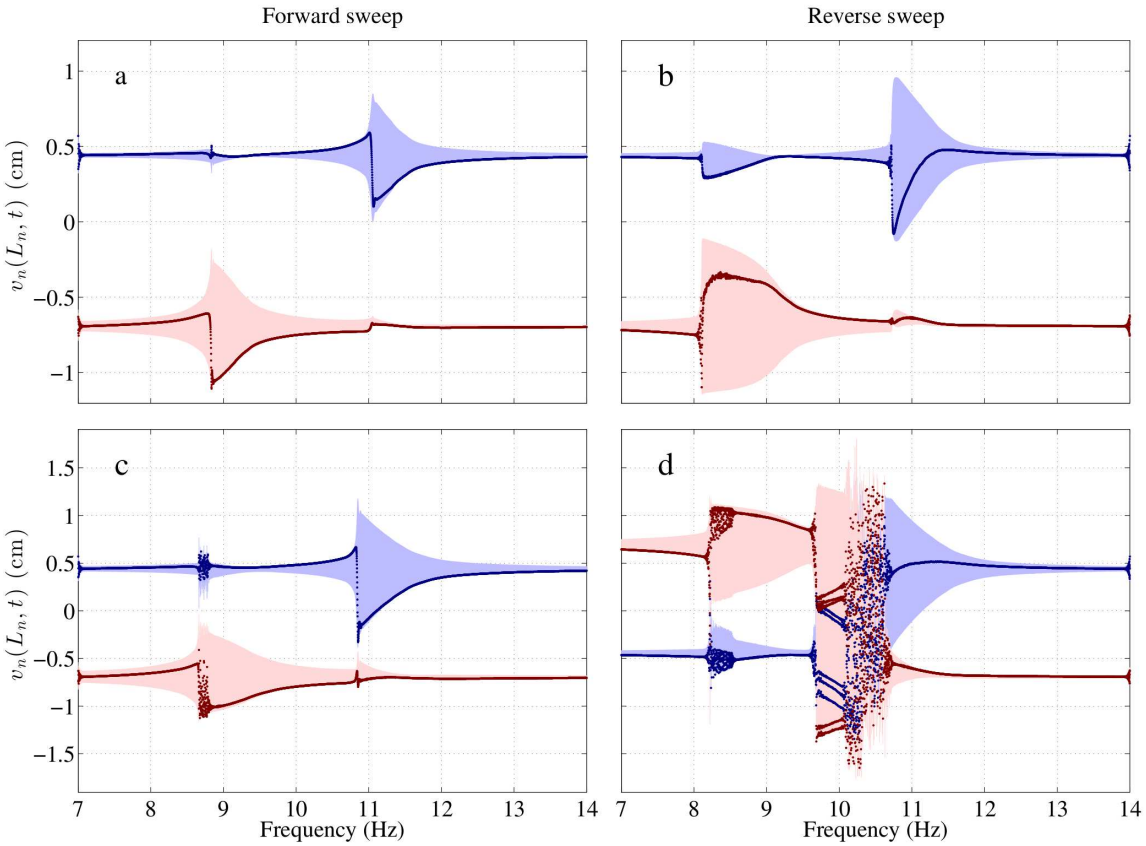

FIGURE 5.4: Tip displacement response to numerically simulated frequency sweeps for excitation amplitudes of $A = 0.05g$ (a,b) and $0.095g$ (c,d) and system parameters in Table 5.1. Plots (a,b) show softening intrawell oscillations, while plots (c,d) illustrate the start of diverse behavior at low excitation.

in the separation distance d_z result in changes in the static equilibrium points of the two beam system. The thick lines show stable solutions, with green indicating a beam 1 positive, beam 2 negative solution and blue the opposite and teal a zero deflection state. The thin black line is an unstable solution that is the result of the subcritical pitchfork bifurcation. Because of physical system imperfections such as magnet misalignment, the experimental equilibrium points shown as black circles indicate a symmetry breaking bifurcation, skewing the stable solutions to favor one side.

This chapter investigates the capability of the two beam oscillator to resonate for

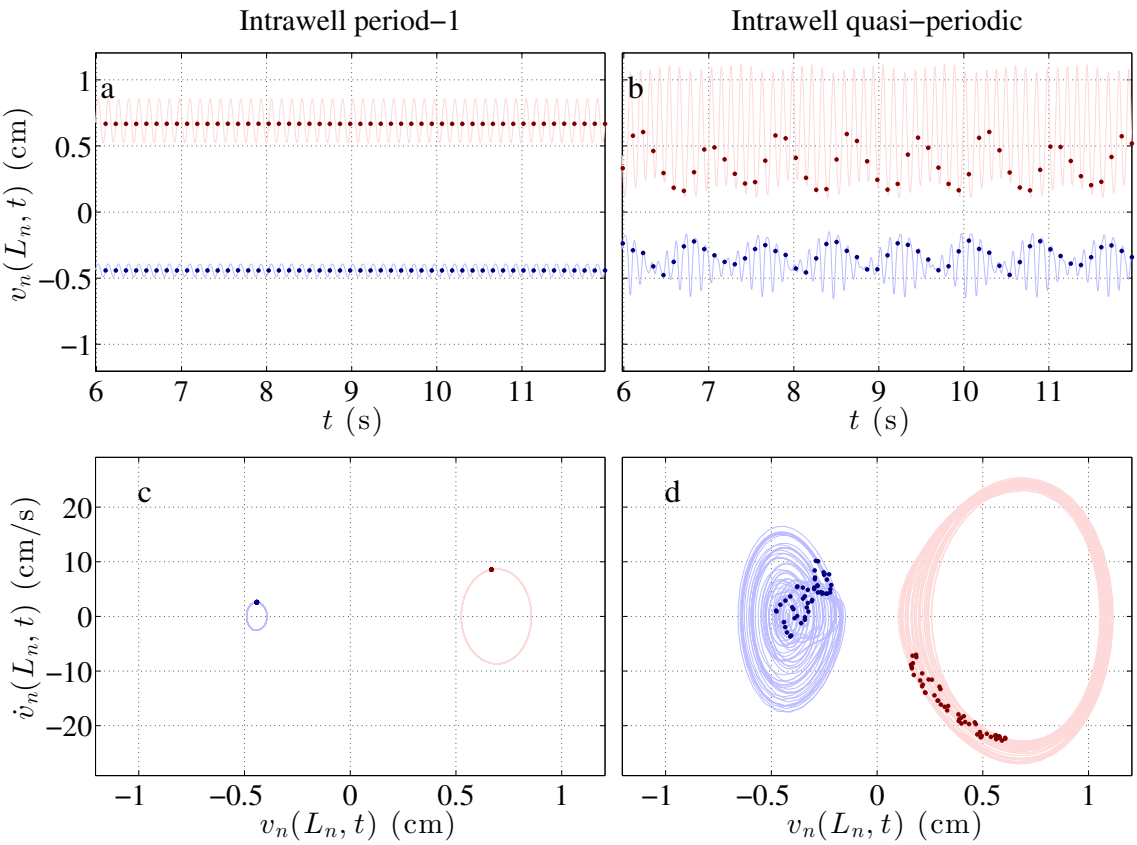

FIGURE 5.5: Coexisting solutions for $A = 0.095g$ and $f = 8.35$Hz from Fig. 5.4. Time series samples are in plots (a) and (b) and phase portraits are shown in plots (c) and (d) for intrawell period-1 solutions and quasi-periodic solutions, respectively.

a broader range of frequencies, beyond the capability of a linear system. To ensure a rich behavior profile, the beams were separated by a distance of 2.22 cm, which allowed for well escapes at low excitation amplitude.

5.2 Numerical investigations

This section explores the forced response of the nonlinear system. Figures show the amplitude of oscillation, instantaneous squared velocity, and average squared velocity to give an accurate picture of the energy harvesting potential since the energy converted into a coupled electrical circuit generally scales with velocity. Numerical

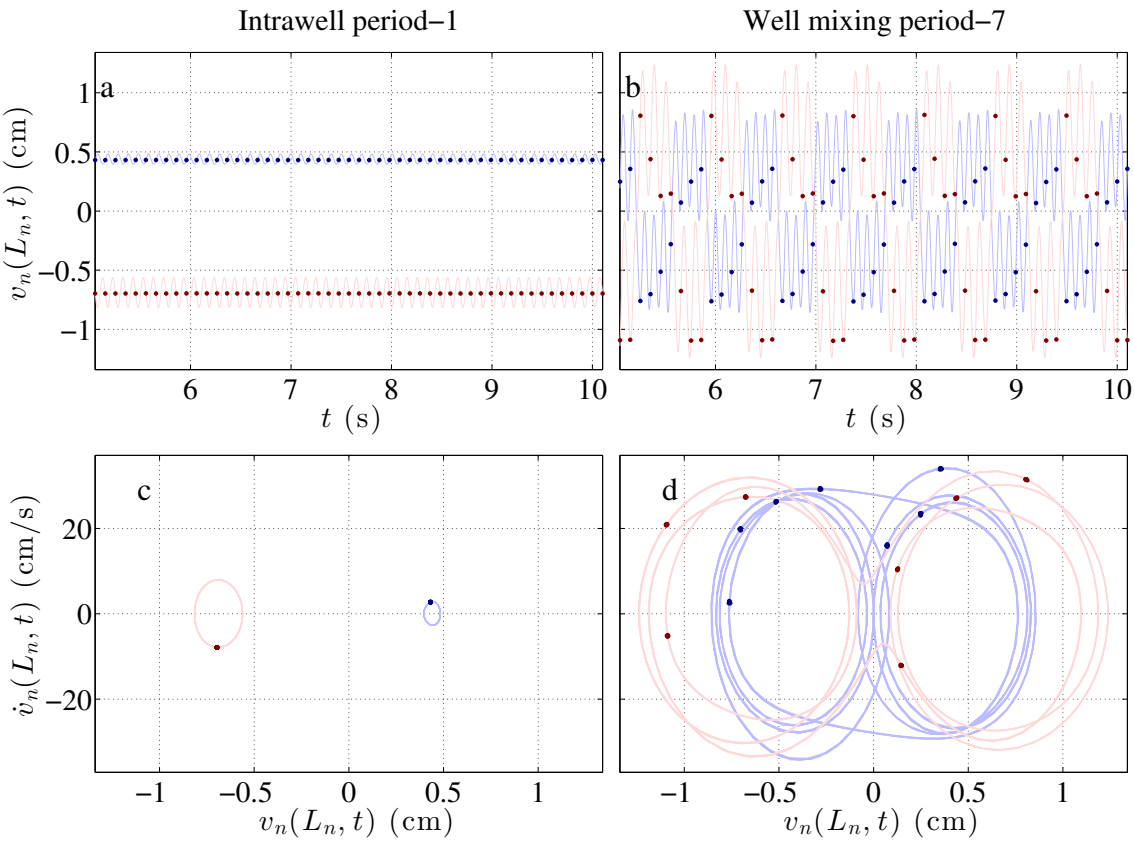

FIGURE 5.6: Coexisting solutions for $A = 0.095g$ and $f = 9.9$Hz from Fig. 5.4. Time series samples are in plots (a) and (b) and phase portraits are shown in plots (c) and (d) for intrawell period-1 solutions and well mixing period-7 solutions, respectively.

studies were simulated for forward and reverse frequency and amplitude sweeps. Individual parameter set spaces were selected as well for comparative simulations with varying initial conditions to illustrate coexisting oscillatory solutions. Figures below depict oscillations of the first and second oscillator in light blue and pink, respectively. Additionally, stroboscopicly sampled points taken at the beginning of each period are marked in blue or red for the first and second oscillator, respectively. The beam separation is $d_z = 27.4$ mm for all numerical studies and all other parameters are found in Table 5.1.

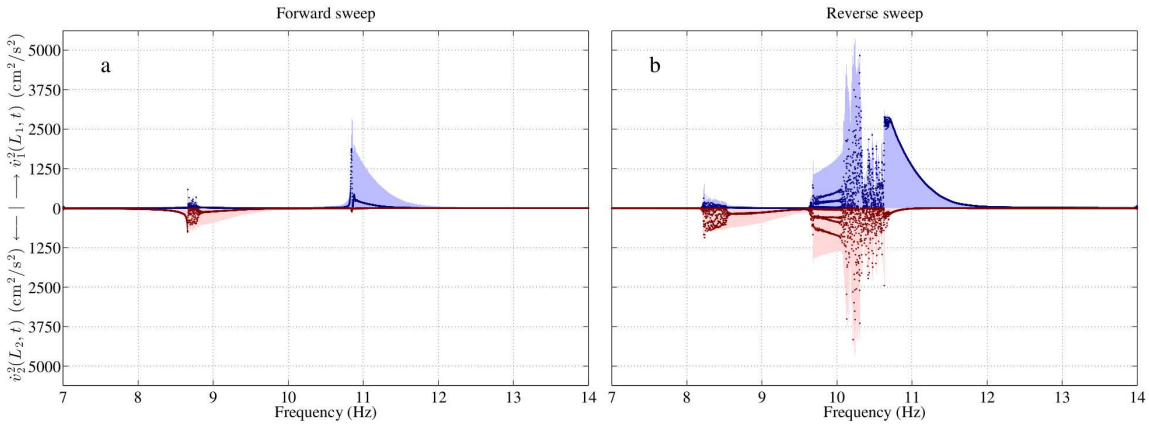

FIGURE 5.7: Tip velocity squared response to numerically simulated frequency sweep at excitation amplitude of $0.095g$ showing higher response for well mixing chaotic and periodic oscillations. This corresponds to Fig. 5.4c,d.

5.2.1 Broadband behavior

High energy oscillation for a wide band of frequencies is of particular interest. To illustrate this system's behavior, increasing and decreasing frequency sweeps were numerically simulated by time-marching algorithms. A linear frequency sweep was performed numerically by setting a base excitation with the form $\ddot{v} = -A\sin(2\pi[f_0 + \frac{1}{2}f_r t]t)$, with f_0 as the initial frequency and f_r as the frequency sweep rate. To accurately capture the nonlinear behavior as discussed in Ref. [96], the sweep rate was kept exceedingly slow to $f_r = \pm 0.01$ Hz/s.

The first set of frequency sweeps is shown in Figure 5.4 with forward sweeps on the left and reverse sweeps on the right. For very low amplitude excitation (0.05g, where g is 9.81 m/s^2) in Fig. 5.4a,b, the oscillator shows an intrawell solution with clear softening behavior. For a slightly higher amplitude (0.095g), the forward sweep shows a small band of transient single well chaos near the second oscillator natural frequency (8.713 Hz). For the reverse sweep in Fig. 5.4d, the behavior is more diverse. For lower frequencies (near 8.2-8.5 Hz), the oscillator undergoes an intrawell period doubling that often leads to chaotic solutions, however not in this case. This

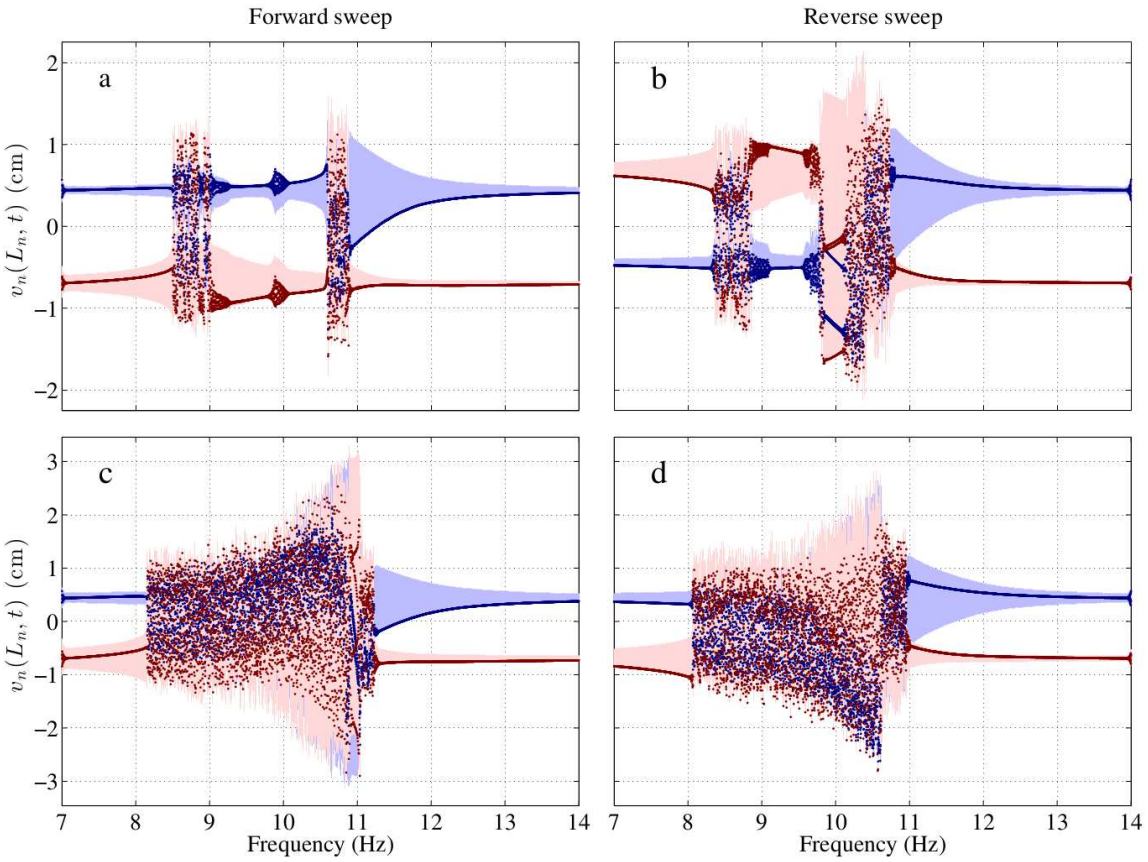

FIGURE 5.8: Tip displacement response to numerically simulated frequency sweeps for excitation amplitudes of $A = 0.15g$ (a,b) and $0.3g$(c,d) and system parameters in Table 5.1. Plots (a,b) show diverse intrawell and well mixing solutions, while plots (c,d) are dominated by chaotic well mixing.

doubling coexists with an intrawell low-amplitude solution. Figure 5.5 illustrates these solutions in a time series and phase portrait. The period doubling phenomena in the frequency sweep manifests as a quasi-periodic solution as shown in Fig. 5.5b,d. Additionally in Fig. 5.4d, a region of chaotic well mixing solutions (near 10.1-10.6 Hz) is apparent, as is a period-7 solution (near 9.7-10 Hz). These oscillations both coexist with small amplitude intrawell solutions. Coexisting at 9.9 Hz are a period-1 intrawell solution and period-7 well mixing solution as shown in Fig. 5.6.

Observing the velocity squared plot in Fig. 5.7 for the 0.095g sweep, an indication

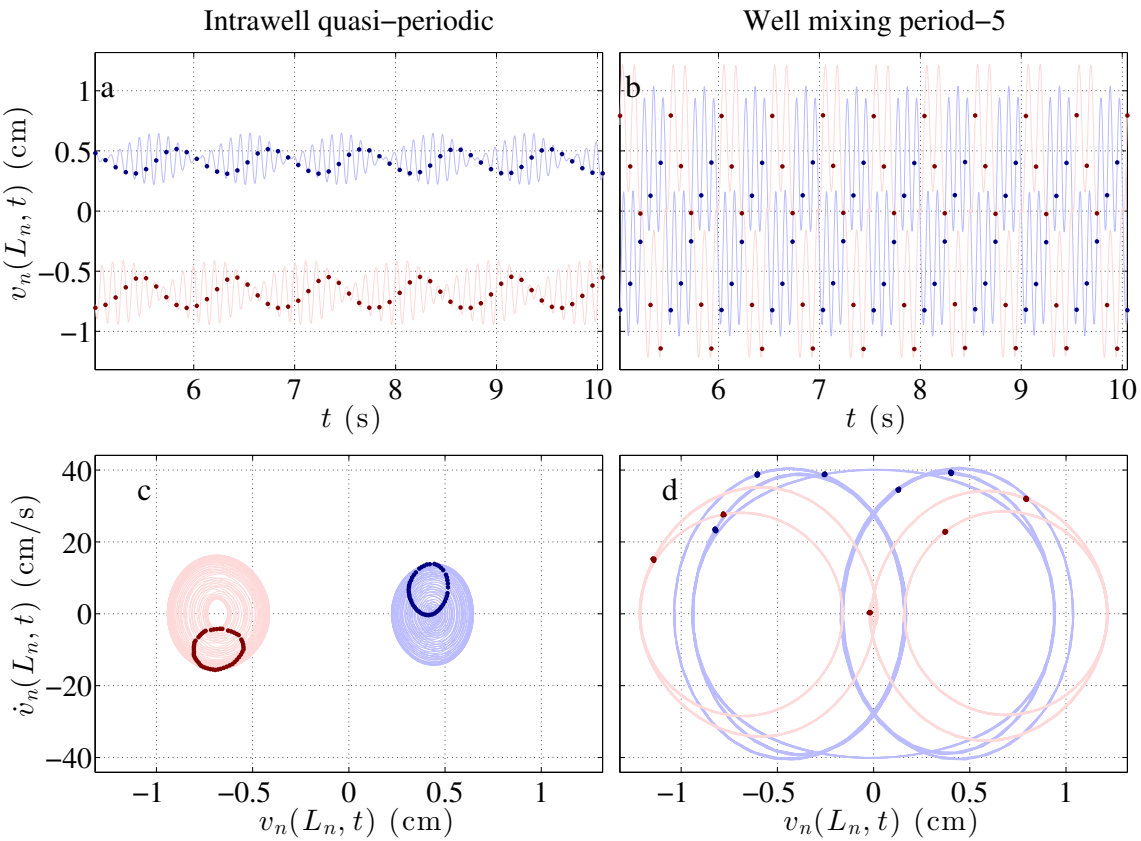

FIGURE 5.9: Coexisting solutions for $A = 0.15$ and $f = 9.95$Hz from Fig. 5.8. Time series samples are in (a) and (b) and phase portraits are shown in (c) and (d) for intrawell quasi-periodic solutions and well mixing period-5 solutions, respectively.

of the harvesting potential for different parameter spaces is evident. The reverse sweep reveals a rich power potential. Certain chaotic vibrations are high energy for both oscillators, but would require voltage rectification because of their out of phase oscillation. Also, while the first oscillator shows a higher intra well oscillation velocity at around 10.9 Hz than for the well mixing period-5 behavior near 9.9 Hz, the second oscillator has a very limited velocity at this higher frequency and would likely have a lower power output. When examining this power potential, the oscillatory phase between the two beams is important. In phase behavior means the voltages in a series connected system would add, thus increasing the power potential. This in-

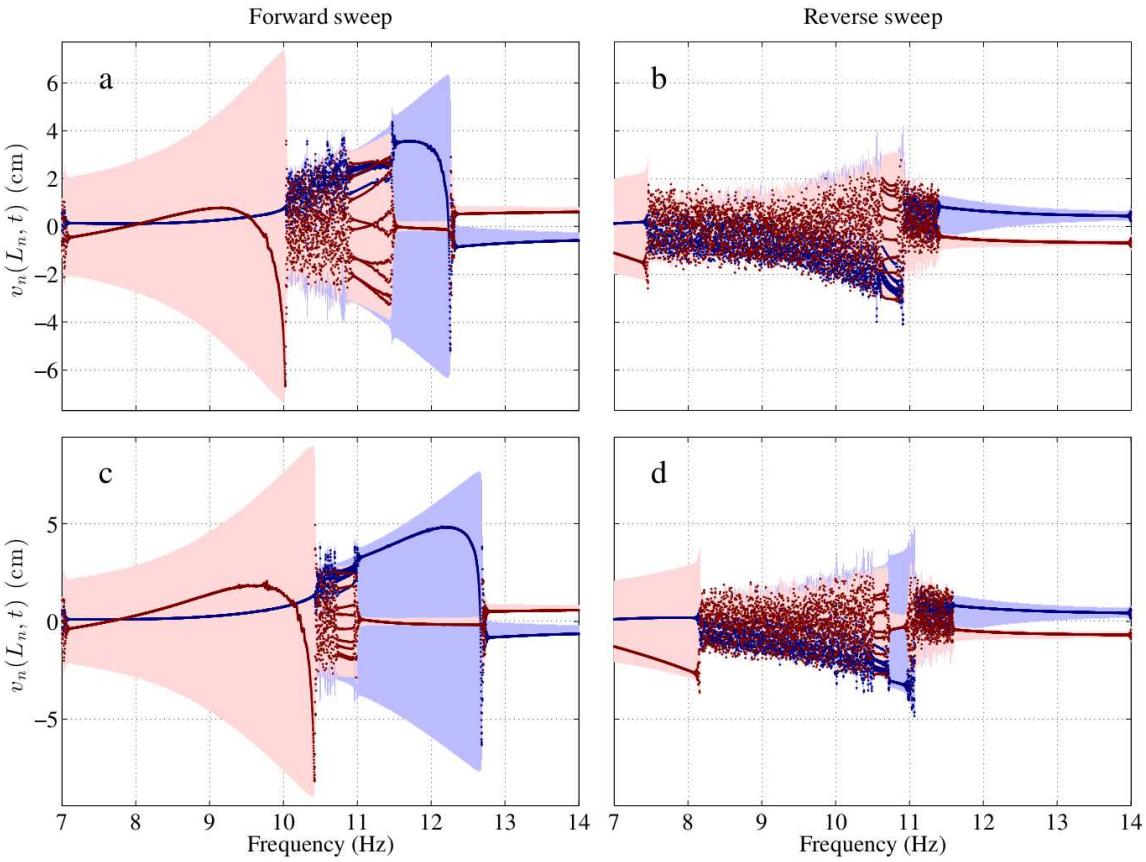

FIGURE 5.10: Tip displacement response to numerically simulated frequency sweeps for excitation amplitudes of $A = 0.7g$ (a,b) and $0.9g$ and system parameters are in Table 5.1. Both excitation amplitudes show coexisting chaotic and period-1 solutions for forward and reverse sweeps.

phase motion is shown in Fig. 5.5a,c. Conversely, out-of-phase motion (see Fig. 5.6) would require voltage rectification in the electrical system to fully utilize the voltage sources. Doing so would have a voltage cost due to the diode voltage thresholds that would need to factored into efficacy considerations.

Figure 5.8 plots the second set of sweeps with excitation amplitude of 0.15g and 0.3g for a,b and c,d, respectively. Of particular interest is the low intrawell period doubling near 9.95 Hz in subplot a that coexists with the period-5 well mixing solution of subplot b. The coexisting intrawell quasi-periodic and well mixing period-

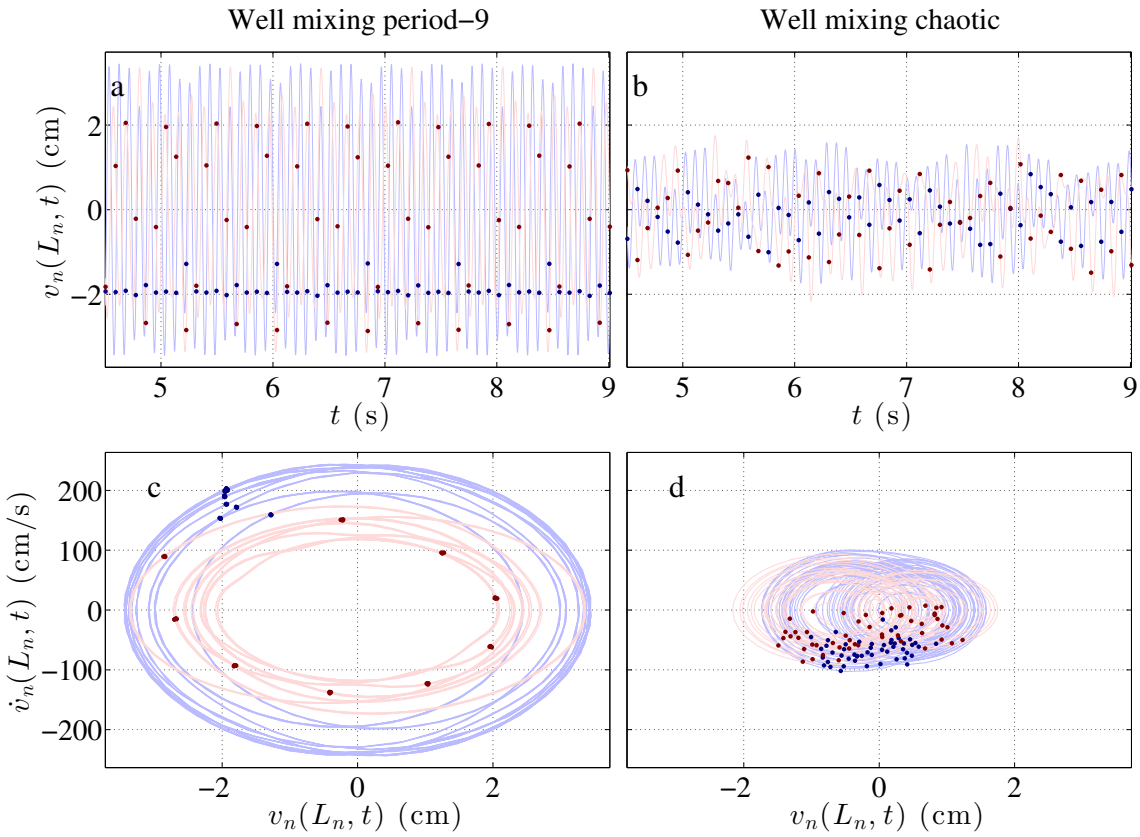

FIGURE 5.11: Coexisting solutions for $A = 0.7g$ and $f = 11.1$Hz from Fig. 5.10. Time series samples are in (a) and (b) and phase portraits are shown in (c) and (d) for well mixing period-9 solutions and chaotic solutions, respectively.

5 solutions at 9.95 Hz are shown in Fig. 5.9. Again, this out of phase motion would require rectification of the coupled voltage for an electrical system. Figure 5.8 c,d shows shifted regions of chaos between reverse and forward sweeps, as well as a unique, period-4 solution for a narrow band around 10.95 Hz.

The final set of frequency sweeps is at a higher amplitude excitation (0.7g and 0.9g). In Fig. 5.10, the hardening effect of the large, interwell potential energy is visible. For the forward sweeps in Fig. 5.10a,c, the large amplitude well mixing solutions extend over much wider frequency ranges (near 7-10 Hz and 11.5-12.2 Hz for a, and near 7-10.4 Hz and 11-12.6 Hz for c) than the reverse sweeps in b,d

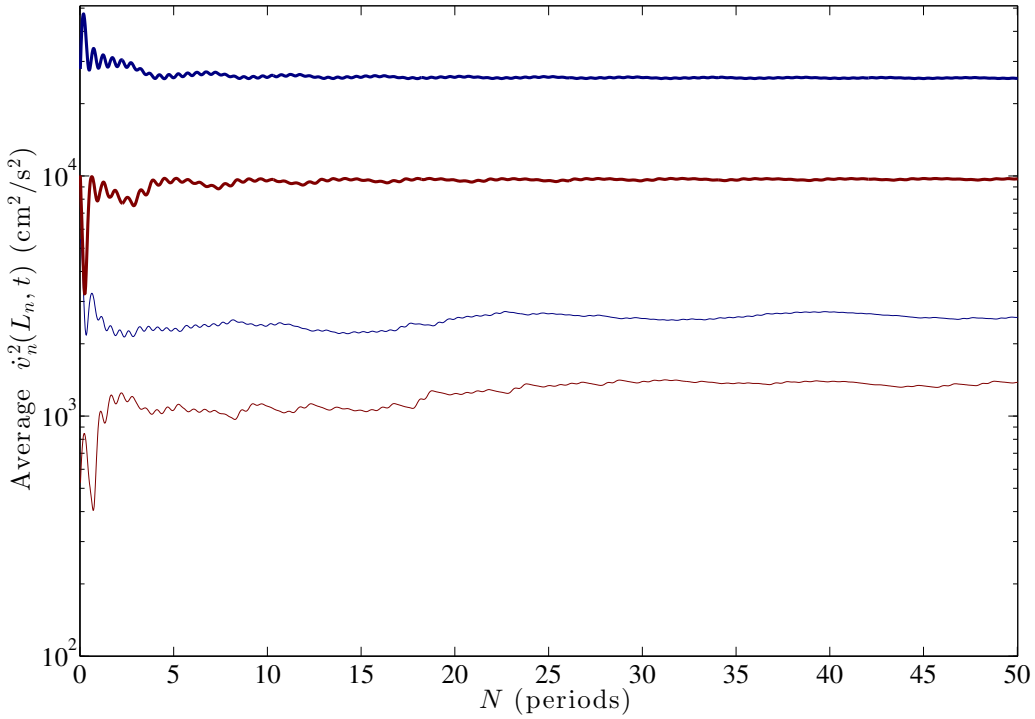

FIGURE 5.12: Asymptotic velocity squared average for beam tip 1 (blue) and 2 (red) at $A = 0.7g$ and $f = 11.1$ Hz excitation. Chaotic power is represented by thin lines and period-9 by thick lines. This corresponds to Fig. 5.11 and shows higher power for period-9 solutions.

(only near 7-7.4 Hz for b and near 7-8.1 Hz and 10.8-10.9 Hz for d). The reverse sweep case shows solutions with large amplitude oscillations and well mixing chaotic or small amplitude intrawell behavior. Both excitation amplitudes show period-9 behavior, while the reverse sweep for $A = 0.9$g has a brief region of period-7 oscillations that coexists with a chaotic region in the forward sweep. In Fig. 5.11, the coexisting period-9 and chaotic well mixing behavior for 11.1 Hz and 0.7g is shown. To illustrate the long term power potential, the asymptotic velocity for these two solutions is displayed in Fig. 5.12. The period-9 solution has a higher asymptotic average velocity and a more quickly converged value. In Fig. 5.13, the coexisting period-1 and chaotic well mixing behavior for 9.5 Hz and 0.9g is shown, while Fig. 5.14 shows the asymptotic velocity squared behavior. This figure illustrates the large

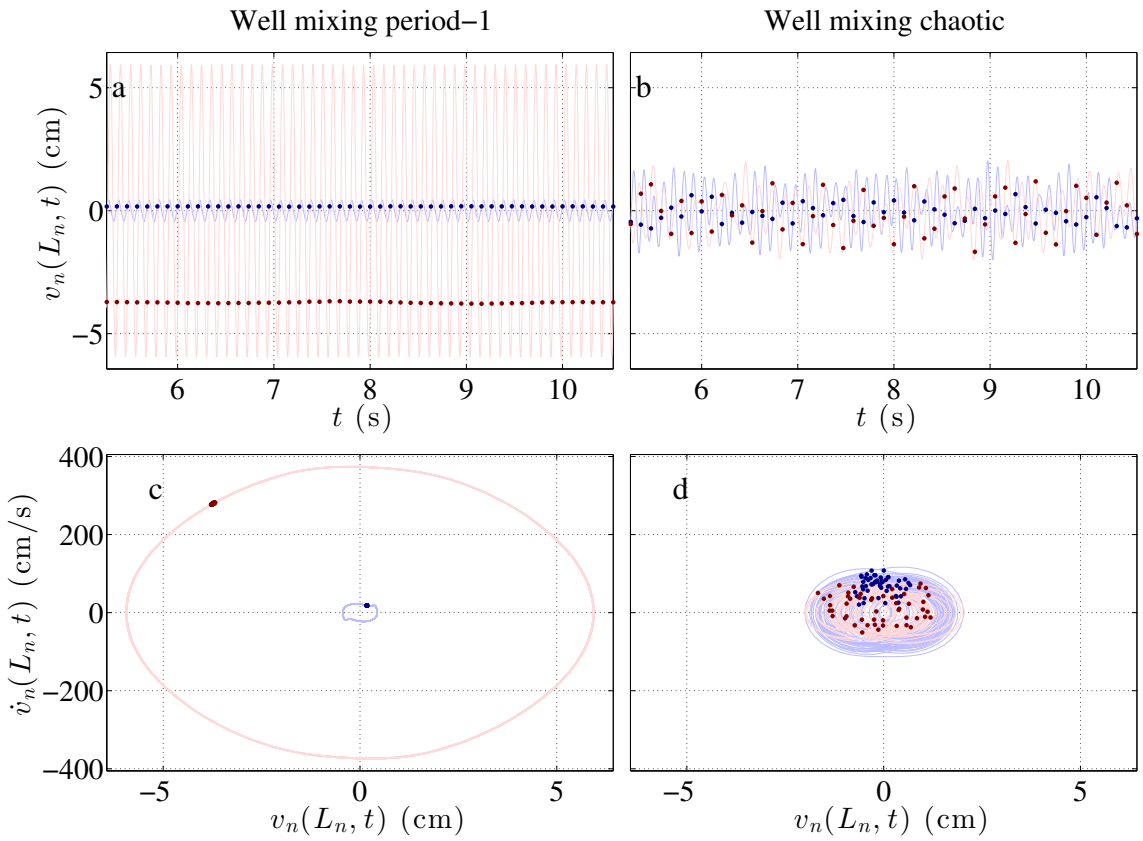

FIGURE 5.13: Coexisting solutions for $A = 0.9g$ and $f = 9.5$Hz from Fig. 5.4. Time series samples are in (a) and (b) and phase portraits are shown in (c) and (d) for well mixing period-1 solutions and chaotic solutions, respectively.

amplitude period-1 solution for the second oscillator and the small solution for the first, while the chaotic solutions have a similar velocity squared signature.

The velocity squared representation of the 0.7g frequency sweep in Fig. 5.15 highlights the velocity discrepancy between the periodic and chaotic well mixing solutions. Chaotic solutions have a much lower velocity and therefore smaller power potential than the much larger period-9 and period-1 well mixing solutions. Note however that period-1 behavior is dominated by a single oscillator. For lower frequencies, the second oscillator oscillates at much higher amplitude than the first, while for higher frequencies the opposite is true. The result of this behavior is a velocity profile

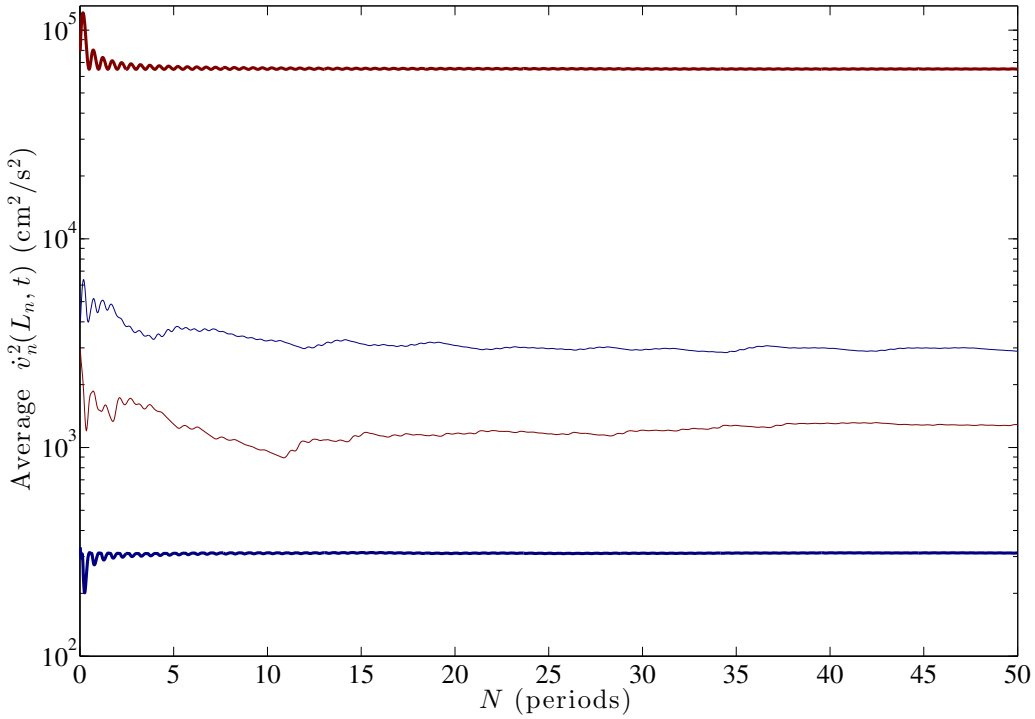

FIGURE 5.14: Asymptotic velocity squared average for beam tip 1 (blue) and 2 (red) at $A = 0.9g$ and $f = 9.5$ Hz excitation. Chaotic power is represented by thin lines and period-1 well mixing by thick lines. This corresponds to Fig. 5.13 and highlights the power difference between beams for the well mixing period-1 oscillations.

dominated by a single oscillator. In the case of the period-9 oscillations, however, both oscillators respond with similar velocities. This dual oscillation would be ideal for energy harvesting electrical systems that could take advantage of the additional voltage source.

5.2.2 Amplitude dependence

The chaotic, period-n, and period-1 oscillations either intrawell or well mixing are amplitude dependent, with hysteretic energy threshold levels dependent on initial conditions. To illustrate these coexisting and amplitude dependent oscillatory phenomena, amplitude sweeps were simulated with fixed excitation frequency and linear increasing or decreasing excitation acceleration amplitude. This excitation takes the

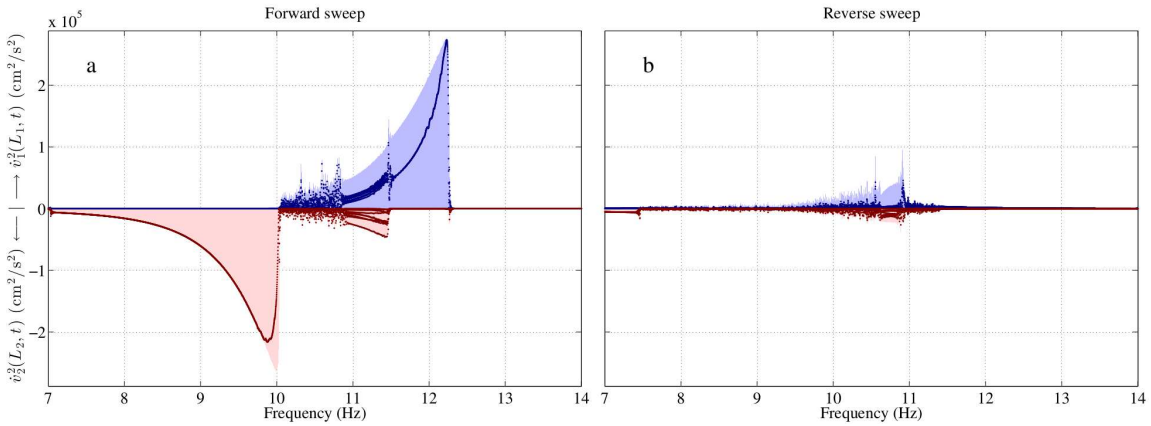

FIGURE 5.15: Tip velocity squared response to numerically simulated frequency sweep at excitation amplitude of $0.7g$ showing discrepancy between the periodic and chaotic well mixing solutions. This corresponds to Fig. 5.10a,b.

form $\ddot{v} = -(A_0 + A_r t)\sin(\Omega t)$, where Ω is the excitation amplitude, A_0 is the initial amplitude, and A_r is the rate of change. The rate of change is dependent on the excitation frequency $A_r = \pm 10^{-4}$ g / T where T is the excitation period.

Two sets of forward and reverse sweeps were simulated with one set at frequencies below the lower natural frequency of the second oscillator (red/pink) and the other above. The first set is shown in Fig. 5.16 with amplitude sweeps at 7.406 Hz for a-b and 8.1 Hz for c,d. Hysteresis is apparent for both frequencies with the intrawell to periodic well mixing at a much higher threshold for the forward sweeps than the reverse sweeps. In the case of Fig. 5.16c, this high amplitude solution is preceded by a chaotic well mixing band. The velocity squared signature in Fig. 5.17 for the 8.1 Hz amplitude sweeps again shows the level of the chaotic solution to be considerably lower than the period-1 well mixing solution for the high amplitude oscillator and much higher than the low amplitude oscillator.

The second set plots excitation amplitude sweeps for 9.824 Hz and 11.7 Hz in Fig. 5.18. For a,b, chaotic solutions coexist with small amplitude oscillations. The forward sweep transitions from low amplitude intrawell period-1 solutions to a har-

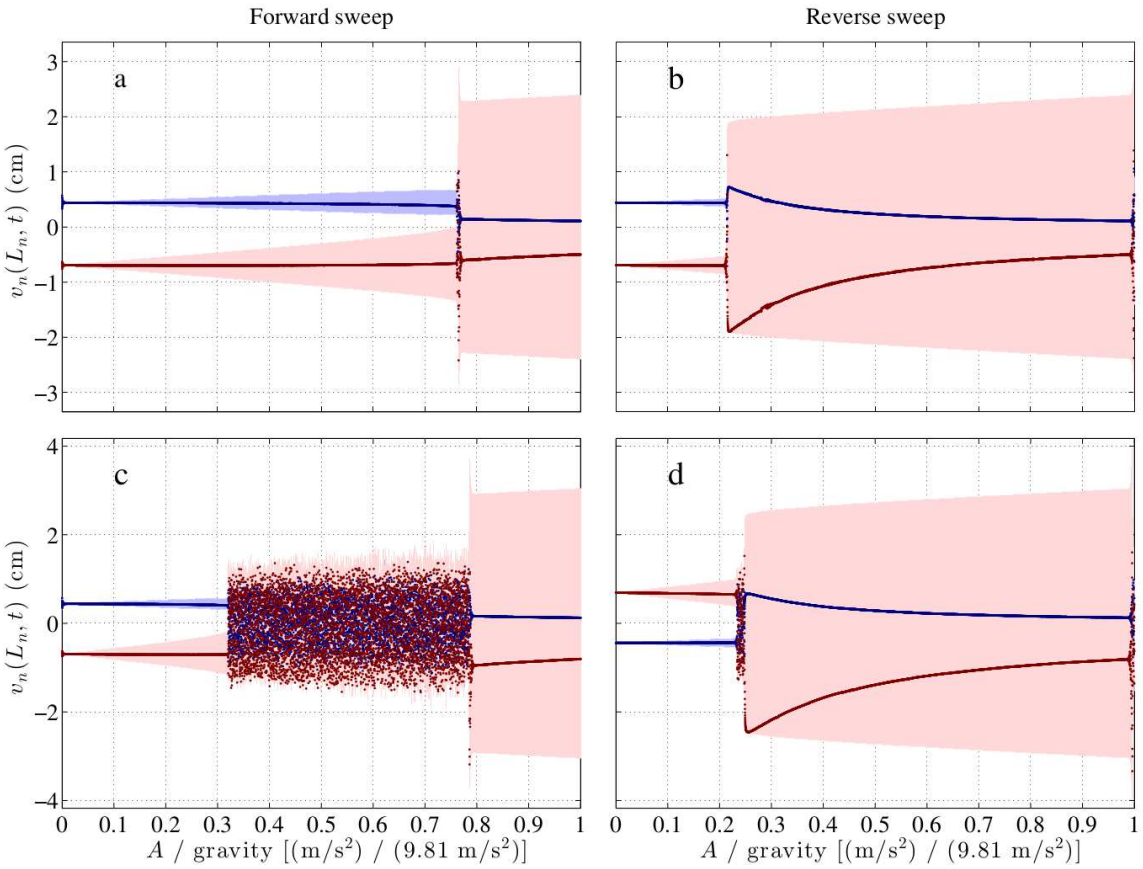

FIGURE 5.16: Tip displacement response to numerically simulated amplitude sweeps for excitation frequencies of $f = 7.406$ Hz (a,b) and 8.1 Hz (c,d) and system parameters are in Table 5.1. Plots (a,b) show coexisting period-1 intrawell and well mixing solutions, while plots (c,d) shows a band of chaotic solutions.

monic solution and back before jumping to chaotic well mixing, while the reverse sweep eliminates the second period-1 solution, skipping straight from harmonics to chaos. For c,d, the response increases linearly with the excitation in the forward sweep, but the reverse shows chaotic and subharmonic solutions at higher amplitudes.

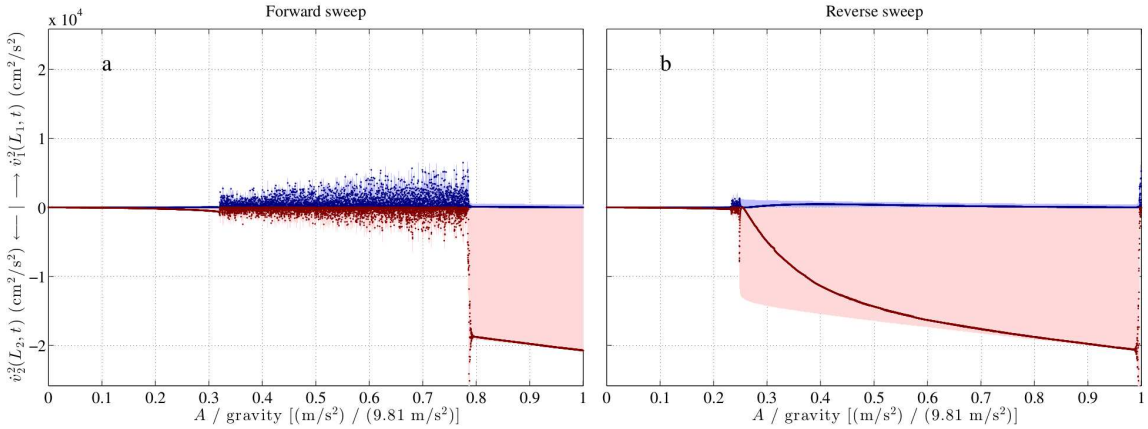

FIGURE 5.17: Tip velocity squared response to numerically simulated amplitude sweeps at excitation frequency of 8.1 Hz, corresponding to Fig. 5.16c,d. This illustrates the response difference between period-1 and chaotic solutions.

5.3 Experimental investigation

This section describes the tests performed to verify the qualitative, phenomenological behavior shown in the numerical investigation. In particular, excitation response with coexisting solutions was sought, as well as the other interesting phenomena such as subharmonic oscillations and well mixing chaotic responses.

5.3.1 Excitation results

A set of frequency sweeps and amplitude were performed to characterize the nonlinear behavior of the oscillators and correspond with the phenomenological findings of the numerical studies. The excitation profile used for the experiments was the same as the numerical simulations with linearly changing frequency at a rate of 0.01 Hz/s. Figure 5.20 shows forward and reverse frequency sweeps between 7 and 12 Hz at 0.1g excitation for a,b and 0.6g excitation for c,d. The rich behavior in the theoretical system is mirrored by the experimental results. Figure 5.20a,b shows softening behavior for the low frequency intrawell solutions and hysteretic region of chaotic oscillations. Figure 5.20c,d is for larger excitation and therefore has a

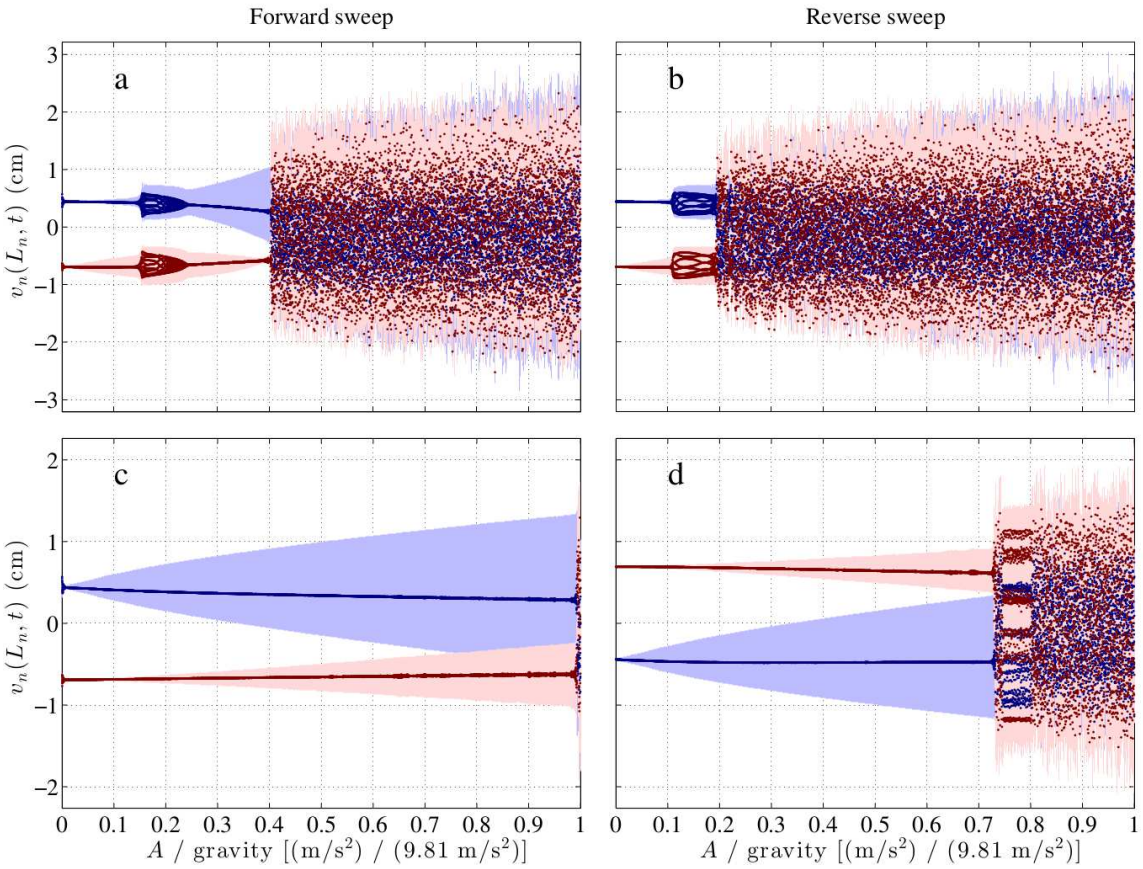

FIGURE 5.18: Tip displacement response to numerically simulated amplitude sweeps for excitation frequencies of $f = 9.824$ Hz (a,b) and 11.7 Hz (c,d) and system parameters are in Table 5.1. Coexisting solutions exist for sweeps at 9.824 Hz and 11.7 Hz.

larger frequency band of chaotic well mixing solutions. These solutions coexist with subharmonics and intrawell period-1 oscillations. Also of note are large amplitude intrawell solutions with in-phase oscillation. For energy harvesting purposes, this in-phase oscillation would allow for the corresponding transducer voltages to add, thus requiring now rectification.

Although the detailed frequency sweeps show no explicit evidence of high energy subharmonic responses, the theoretical investigations suggest these are possible. Figure 5.21 illustrates such a parameter set, with 0.6g excitation amplitude at 9.1 Hz.

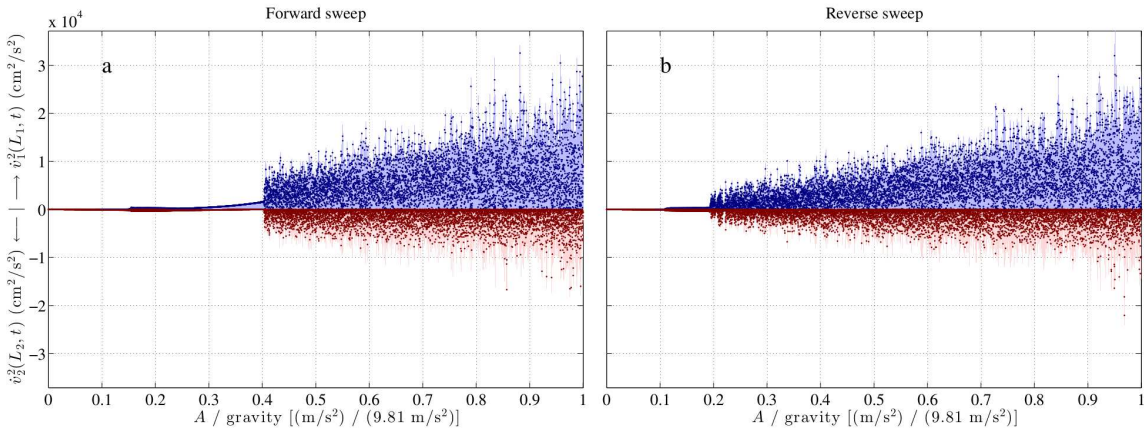

FIGURE 5.19: Tip velocity squared response to numerically simulated amplitude sweeps at excitation frequency of $f = 9.824$ Hz, corresponding to Fig. 5.18a,b. This highlights the response difference between chaotic and intrawell solutions.

Coexisting with the period-3 oscillation shown in the figure is a chaotic response with a similar energy profile. As in the theoretical investigations, it is best to compute the asymptotic squared velocity term for the two oscillators to explore the power harvesting potential. Figure 5.22 shows the velocities of both oscillators for both cases. The squared velocities of both cases are similar with oscillator 1 having a larger velocity squared.

5.4 Summary and conclusions

This chapter explored a two beam bistable system to illustrate the rich phenomenological behavior of the system and provide a baseline study for a potential two beam harvesting system. First, a detailed model was derived with large amplitude oscillation in mind including a magnetic potential model for the interaction between the two tip magnets. These tip magnets served to couple the beams together and create a potential energy profile with two distinct wells, giving each beam an individual bistability. By selecting a magnet distance so as to create shallow local wells, the system excitations both numerically and experimentally gave way to a wide array of

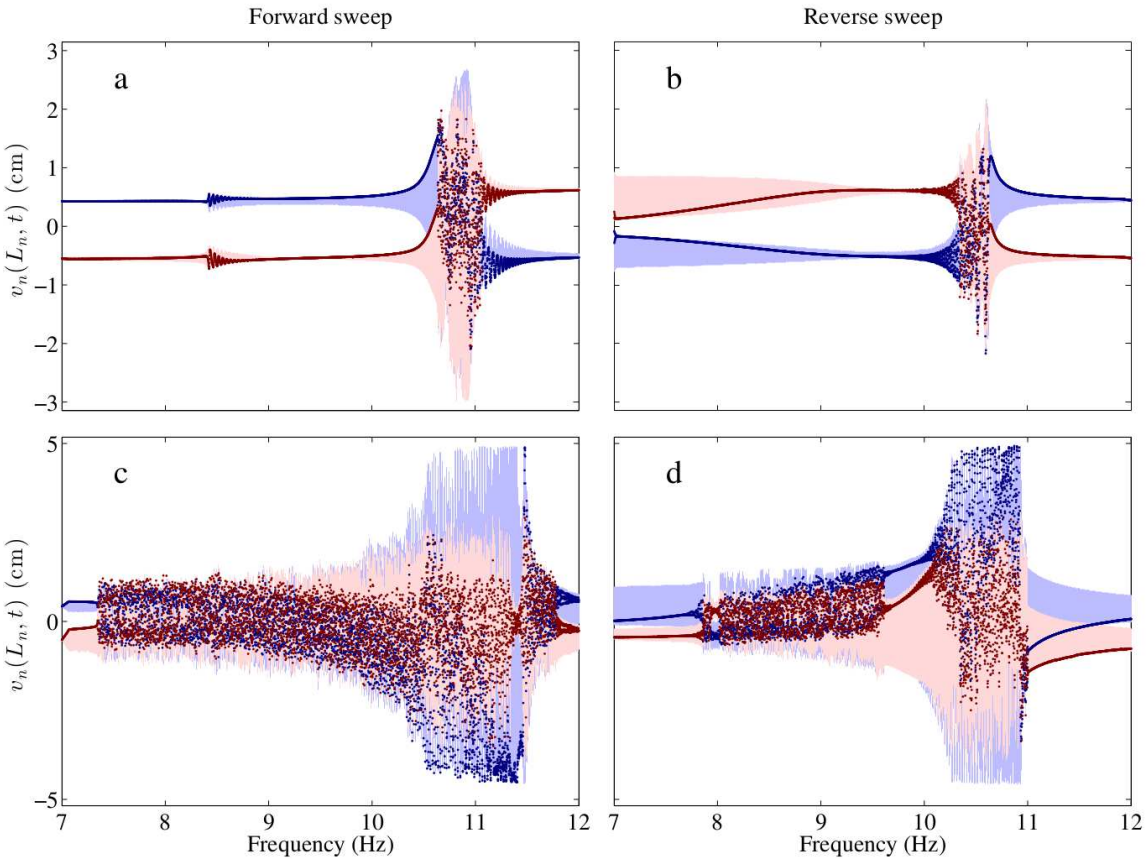

FIGURE 5.20: Experimental beam tip response to frequency sweeps for $A = 0.1g$(a,b) and $0.6g$(c,d). Plots (a,b) show the softening behavior and plots (c,d) shows chaotic well mixing behavior in the experimental system.

well mixing and intrawell oscillations.

The numerical simulations based on the theoretical model were shown to accurately mirror the phenomena seen in the experimental system. Chaotic solution spaces were found to coincide with periodic and subharmonic solutions with different initial conditions. Taking the analysis a step further, these chaotic solutions showed lower velocity squared values than periodic well mixing solutions, pointing to a higher energy potential for the periodically locked solutions. Additionally, the chaotic solutions (as well as out of phase periodic) would require voltage rectification to properly capture the generated electrical signals. The broadband behavior of the

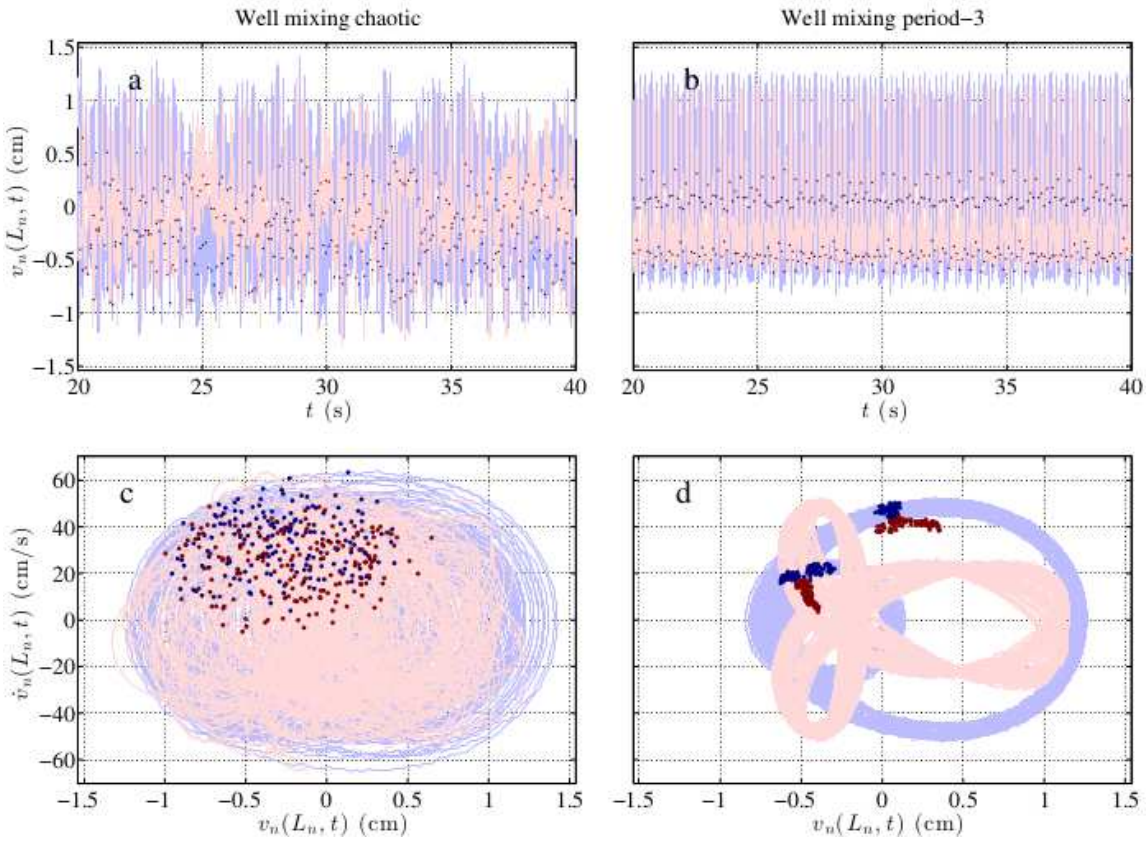

FIGURE 5.21: Experimental time series (a,b) and phase portrait (c,d) for coexisting well mixing chaotic and period-3 oscillations, respectively. Excitation parameters were $A = 0.6g$ and 9.1 Hz.

system further illustrated the usefulness of a two beam system with multiple natural frequencies. Instead of an uncoupled system, the resonant intrawell behavior serves to excite the non resonant beam and induce energetic solutions from both. It is these high energy, high velocity periodic solutions that show the most promise for useful conversion to electrical energy.

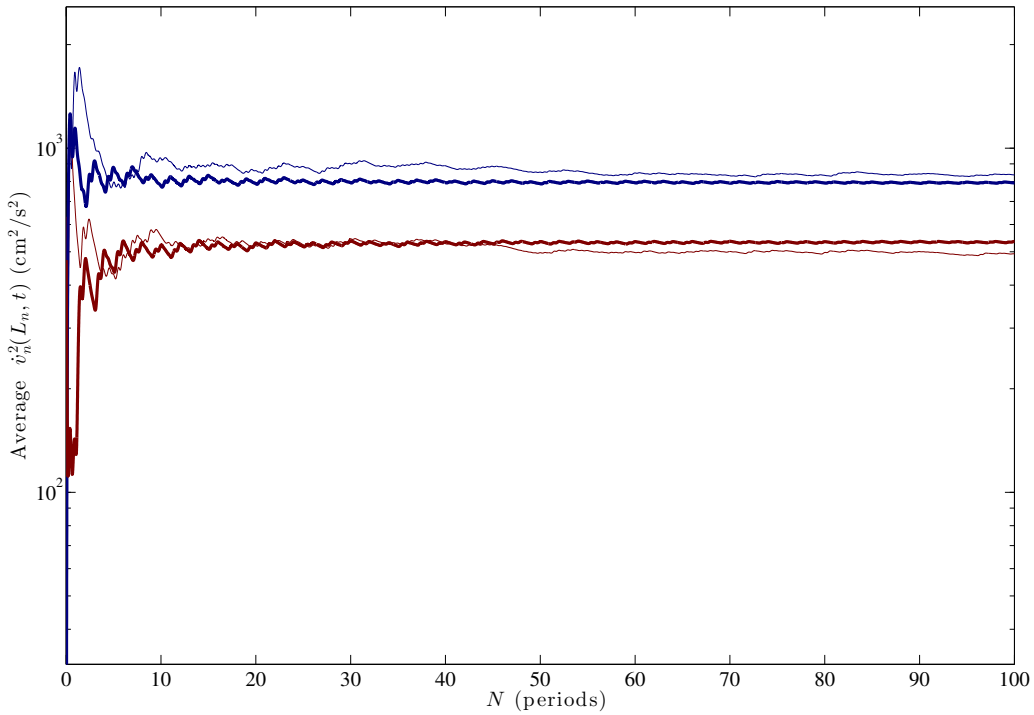

FIGURE 5.22: Asymptotic velocity squared average for beam tip 1 (blue) and 2 (red) at $A = 0.6g$ and $f = 9.1$ Hz excitation. Chaotic power is represented by thin lines and period-3 well mixing by thick lines. This corresponds to Fig. 5.21 and shows the power similarity of the solutions.

6

Two dimensional lattice of beams with magnetic tip masses

An understanding of the properties of periodic structures has been established in the literature with a focus on microscale structures consisting of two or more materials of different properties [24, 25, 31, 97]. Depending on the relationship between the two materials properties, there may exist frequencies where waves do not propagate throughout the structure [24, 25]. Likewise, similar research has also been done to explore the existence of structures that have a similar effect on elastic waves. These phononic structures have gained traction recently and the literature is rich with reviews of previous work, theoretical analysis for particular structure configurations, and experimental systems that show this behavioral response [30, 31]. These structures have found applications in sound filtering, acoustic cloaking, and other structural vibration areas [98–100]. However, the majority of work to this point has focused on small scale structures, using microscale periodicity of materials.

Additionally, the uncertainty inherent in physical systems has been explored for 1-D band gap systems [36]. Manufacturing uncertainty or material property variations

can drastically change the performance of a system. Using numerical methods such as Monte Carlo trials [101] or analytical methods [102, 103], the individual uncertainties of system materials and geometries can be quantified for their effect on the system behavior.

This chapter proposes a system that applies the principles of existing band gap theory to a larger scale system with periodicity on the order of centimeters, not micrometers. This hypothetical system is based on a system of plastic beam elements affixed with small magnets at their tips. Fixed upright into a large array made up of repeating unit cells, the magnet ends are given the same orientation across the array. The resulting opposite magnetic forces effectively creates nonlinear spring interactions in two dimensions within the array. This two dimensional oscillating system is explored first as an infinite array of repeating N x N unit cells. Varying the mass configuration in a simple 2 x 2 cell, the band structure for the periodically varying infinite lattice is explored for the existence of frequency gaps with no propagating waves. Uncertainty in this system is then explored by Monte Carlo simulations for situations with an assumed probabilistic uncertainty in the mass and magnetization properties. Additionally, the effects of boundary conditions associated with a finite manifestation of the array system, as well as physical damping are considered for periodically excited arrays of various sizes.

The chapter is organized as follows. Section 6.1 introduces the system and constructs the mathematical model for interactions of each oscillator, both from beam properties and magnetic interactions. The next section examines different configurations of an idealized, undamped, infinite system, before analyzing the propagation of uncertainty of one such configuration. Section 6.3 explores the damped, finite system. Conclusions follow in the final section.

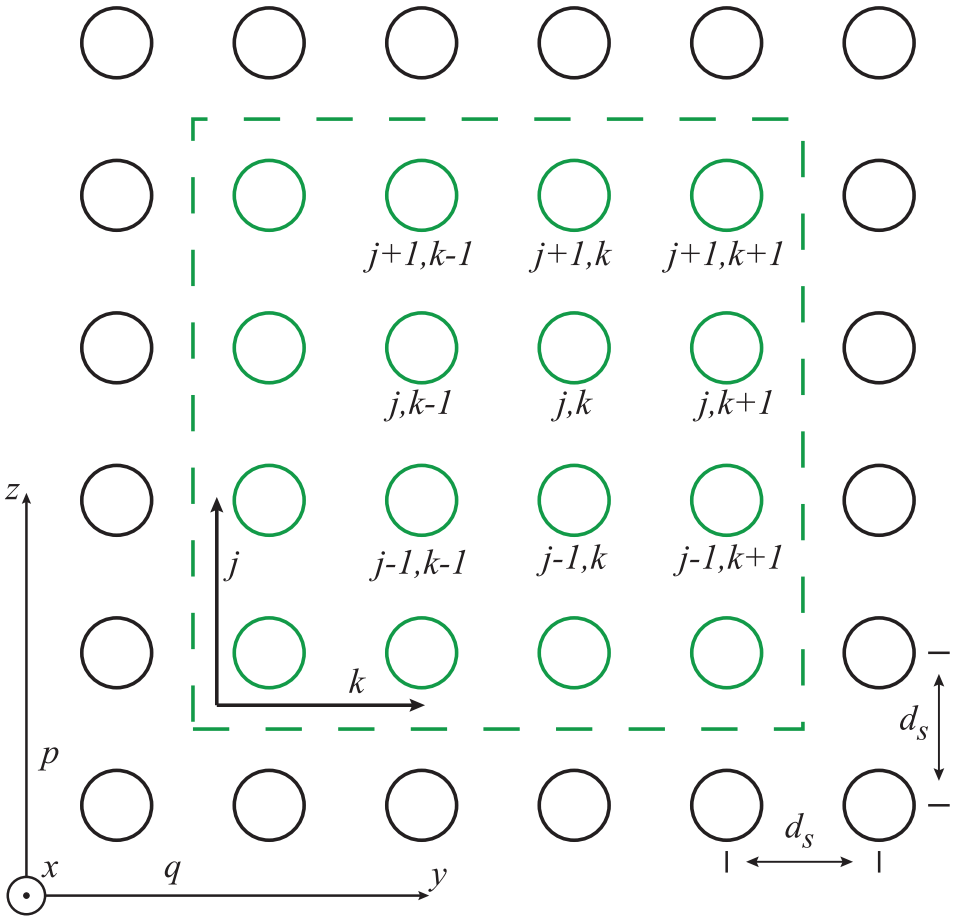

FIGURE 6.1: System model for a lattice of oscillators organized into periodically repeating cells as indicated by the dashed box. Each oscillator is separated by distance d_s. Local indices j and k indicate oscillators within each cell, while p and q represent cell indices.

6.1 System model

The hypothetical system consists of an array of beams organized into periodically repeating cells of N x N oscillators. The proposed system configuration is shown with overview of the array of oscillators in Figure 6.1 and a more detailed diagram of the geometry of individual beam pairs in Figure 6.2. Each oscillator consists of a uniform beam with a magnet fixed at the tip. All tip magnets are oriented such that their polarity points in the $+x$ direction, causing a nonlinear repulsive force between pairs. The beams are separated in both the y and z direction by a distance d_s.

To create a model of the system, both elastic beam and magnetic interactions must be considered. The relevant equations of motion for the system can be found by first forming the kinetic and potential energy equations from Euler-Bernoulli beam theory and a dipole model for the magnetic interactions.

6.1.1 Equations of motion

The kinetic energy of a single beam is a function of beam properties and can be written as

$$T_B = \frac{1}{2}\int_0^L m_l \left(\dot{\hat{v}}(s,t)^2 + \dot{\hat{w}}(s,t)^2\right) ds\,, \tag{6.1}$$

where $\hat{v}(s,t)$ is a transverse oscillation in the global y direction, $\hat{w}(s,t)$ is a transverse oscillation in the global z direction, m_l is the mass per unit length, and s is the arc length coordinate along the beam. An overdot indicates a time derivative. Likewise, the tip mass, taken to be a point mass at the beam tip, has kinetic energy

$$T_T = \frac{1}{2} m_t \left(\dot{\hat{v}}(L,t)^2 + \dot{\hat{w}}(L,t)^2\right)\,, \tag{6.2}$$

where $\hat{v}(L,t)$ and $\hat{w}(L,t)$ are transverse oscillations of the beam tip ($s = L$) and m_t is the tip mass. The potential energy of the beam is the result of internal strain energy in the material and is an expression of the beam curvature

$$V_B = \frac{1}{2}\int_0^L \left(EI_\zeta \hat{v}''^2(s,t) + EI_\eta \hat{w}''^2(s,t)\right)\, ds\,, \tag{6.3}$$

where a ($'$) symbol represents a spatial derivative along s, E is the beam modulus of elasticity, and I_ζ and I_η are the moment of inertia about the neutral axis of the beam in the global y and z axis, respectively. The final piece is the potential energy V_m which is a nonlinear function of the magnet interactions due to the surrounding magnets.

For simplicity, this system is assumed to be operational in frequency ranges about the dominant first frequencies of the beams. Solutions are thus presumed to be functions of the first oscillation mode and the generalized time coordinate for this mode

$$\hat{v}(s,t) = \psi(s)v(t) \text{ and } \hat{w}(s,t) = \psi(s)w(t)\,. \tag{6.4}$$

where the mode shape $\psi(s)$ is taken to be the same for both oscillation directions. This means the energy expressions for a single beam can be simplified to

$$T = \frac{1}{2}\left(m_t\psi(L) + \int_0^L m_l\psi(s)^2 ds\right)\left(\dot{v}^2 + \dot{w}^2\right) = \frac{1}{2}M_{v,w}\left(\dot{v}^2 + \dot{w}^2\right) \tag{6.5}$$

$$U = \frac{1}{2}\left(\int_0^L EI_B\psi''(s)^2 ds\right)\left(v^2 + w^2\right) + V_m = \frac{1}{2}K_{v,w}\left(v^2 + w^2\right) + V_m \tag{6.6}$$

where the beams are presumed to have circular cross-sections and $I_B = I_\zeta = I_\eta$ and V_m is the potential energy due to magnetic interactions of the eight surrounding magnets on the tip magnet under consideration. Assuming a polynomial mode shape for the first mode

$$\psi(s) = \left(\frac{s}{L}\right)^2\,, \tag{6.7}$$

the mass and spring constants are

$$M_{v,w} = \frac{m_l L}{5} + m_t \text{ and } K_{v,w} = \frac{4EI_B}{L^3}\,. \tag{6.8}$$

Applying Lagrange's equation with v and w as the generalized coordinates, the equations of motion for the two dimensional oscillation are

$$M_{v,w}\ddot{v} + K_{v,w}v + \frac{\partial V_m}{\partial v} = 0 \tag{6.9}$$

$$M_{v,w}\ddot{w} + K_{v,w}w + \frac{\partial V_m}{\partial w} = 0\,. \tag{6.10}$$

The following section will derive the energy expression for the magnetic interaction between two tip masses.

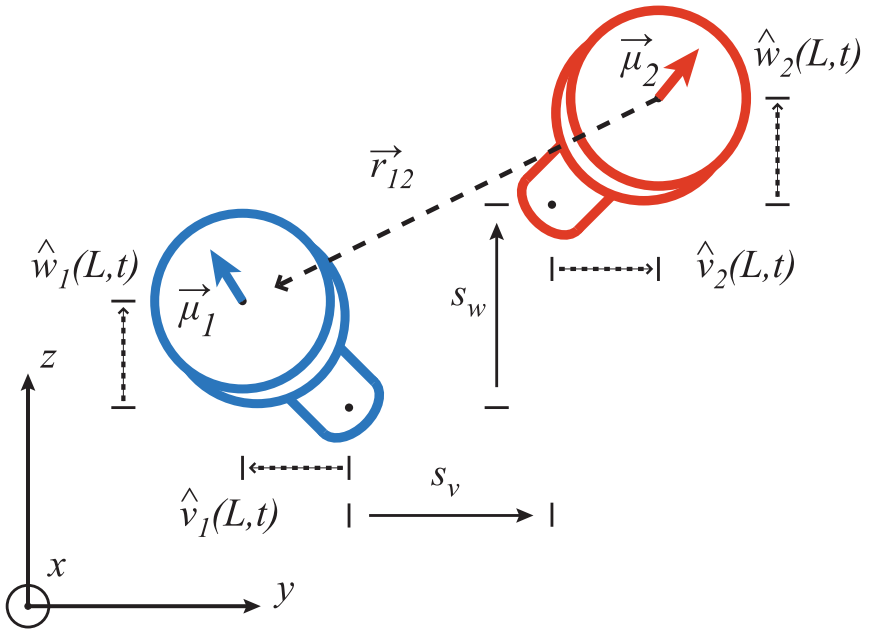

FIGURE 6.2: Diagram and parameters for interactions between two beams with magnetic tip mass.

6.1.2 Magnetic potential energy

This section derives the nonlinear interactions for a pairing of adjacent beams as diagrammed in Figure 6.2. Each magnet is modeled as a magnetic dipole concentrated at the tip of the beam with an appropriate magnetization strength and direction. Interactions between the two dipoles depend on the magnetization vectors of each and the separation vector $\vec{r}_{12}$ between the two. The magnetic field generated by the second magnet at the location of the first is defined

$$\vec{B}_{12} = -\frac{\mu_0}{4\pi}\left(\frac{\vec{p}_2}{|\vec{r}_{12}|^3} - (\vec{p}_2 \cdot \vec{r}_{12})\frac{3\vec{r}_{12}}{|\vec{r}_{12}|^5}\right), \tag{6.11}$$

where $\mu_0 = 4\pi \times 10^{-7}$ H/m is the permeability of free space, and $\vec{p}_2$ is the magnetization vector of the second magnet. This magnetization is represented by $\vec{p} = \vec{M}v_m$, where v_m is volume of the magnet and $\vec{M}$ is the magnetization per unit volume vector. The potential energy of the first magnet as a result of the magnetic interactions

of the second becomes

$$U_{12} = -\vec{p}_1 \cdot \vec{B}_{12}\,. \tag{6.12}$$

For the hypothetical system with the mode shape given in Eq. 6.7, the magnetization vector for either is written

$$\vec{p} = |\vec{M}| v_m \begin{bmatrix} 1 \\ \frac{2v}{L} \\ \frac{2w}{L} \end{bmatrix}. \tag{6.13}$$

The displacement vector is a function of the beam spacing and the relative deflection at the tip,

$$\vec{r}_{12} = \begin{bmatrix} v_1 - v_2 - s_v \\ w_1 - w_2 - s_w \\ 0 \end{bmatrix}, \tag{6.14}$$

with beam spacing $s_v, s_w = \pm d_s$ depending on the beam positioning relative to one another.

With substitution of Eqs. 6.13 and 6.14 into Eq. 6.12, an expression for the potential energy between a single set of beams is derived. The partial of this potential energy function can then be taken with respect to the oscillations of the tip in the y and z directions, $v(t)$ and $w(t)$, to arrive at nonlinear expressions for the forces due to magnetic interactions.

For the finite case, the nonlinear magnet expression is used to find the equilibrium deflections of the oscillators as well as the Jacobian about these equilibria. The negative of the Jacobian at the equilibria acts as the stiffness matrix for the analysis in Section 6.3. However, for the infinite system, oscillations are about the centered, zero-deflection equilibrium and a Taylor series approximation about this fixed point is used to derive linear expressions for the effective stiffness. Combining a central beam and magnet with the interactions from the eight surrounding beams and magnets and using the notation from Figure 6.1, the equations of motion for the (j,k)-th

beam element in the y direction are

$$
\begin{aligned}
M_{j,k}\ddot{v}_{Np+j,Nq+k} = & -K_{vw}v_{Np+j,Nq+k} \\
& + K_m\left(\left(1+C_m\right)v_{Np+j,Nq+k-1} - \left(1-\frac{1}{2}C_m\right)v_{Np+j,Nq+k}\right) \\
& + K_m\left(\left(1+C_m\right)v_{Np+j,Nq+k+1} - \left(1-\frac{1}{2}C_m\right)v_{Np+j,Nq+k}\right) \\
& + \frac{1}{4}K_m\left(1+2C_m\right)\left(v_{Np+j,Nq+k} - v_{Np+j+1,Nq+k}\right) \\
& + \frac{1}{4}K_m\left(1+2C_m\right)\left(v_{Np+j,Nq+k} - v_{Np+j-1,Nq+k}\right) \\
& + \frac{3}{32\sqrt{2}}K_m\left(\left(1+\frac{4}{3}C_m\right)v_{Np+j+1,Nq+k-1} - \left(1-\frac{8}{3}C_m\right)v_{Np+j,Nq+k}\right. \\
& \qquad \left. + \frac{5}{3}w_{Np+j,Nq+k} - \left(\frac{5}{3}+4C_m\right)w_{Np+j+1,Nq+k-1}\right) \\
& + \frac{3}{32\sqrt{2}}K_m\left(\left(1+\frac{4}{3}C_m\right)v_{Np+j-1,Nq+k+1} - \left(1-\frac{8}{3}C_m\right)v_{Np+j,Nq+k}\right. \\
& \qquad \left. + \frac{5}{3}w_{Np+j,Nq+k} - \left(\frac{5}{3}+4C_m\right)w_{Np+j-1,Nq+k+1}\right) \\
& + \frac{3}{32\sqrt{2}}K_m\left(\left(1+\frac{4}{3}C_m\right)v_{Np+j+1,Nq+k+1} - \left(1-\frac{8}{3}C_m\right)v_{Np+j,Nq+k}\right. \\
& \qquad \left. + \left(\frac{5}{3}+4C_m\right)w_{Np+j+1,Nq+k+1} - \frac{5}{3}w_{Np+j,Nq+k}\right) \\
& + \frac{3}{32\sqrt{2}}K_m\left(\left(1+\frac{4}{3}C_m\right)v_{Np+j-1,Nq+k-1} - \left(1-\frac{8}{3}C_m\right)v_{Np+j,Nq+k} + \right. \\
& \qquad \left. \left(\frac{5}{3}+4C_m\right)w_{Np+j-1,Nq+k-1} - \frac{5}{3}w_{Np+j,Nq+k}\right), \qquad (6.15)
\end{aligned}
$$

and the z direction,

$$
\begin{aligned}
M_{j,k}\ddot{w}_{Np+j,Nq+k} = & -K_{vw} w_{Np+j,Nq+k} \\
& + \frac{1}{4} K_m \left(1 + 2C_m\right) \left(w_{Np+j,Nq+k} - w_{Np+j,Nq+k-1}\right) \\
& + \frac{1}{4} K_m \left(1 + 2C_m\right) \left(w_{Np+j,Nq+k} - w_{Np+j,Nq+k+1}\right) \\
& + K_m \left(\left(1 + C_m\right) w_{Np+j+1,Nq+k} - \left(1 - \frac{1}{2} C_m\right) w_{Np+j,Nq+k}\right) \\
& + K_m \left(\left(1 + C_m\right) w_{Np+j-1,Nq+k} - \left(1 - \frac{1}{2} C_m\right) w_{Np+j,Nq+k}\right) \\
& + \frac{3}{32\sqrt{2}} K_m \left(\left(1 + \frac{4}{3} C_m\right) w_{Np+j+1,Nq+k-1} - \left(1 - \frac{8}{3} C_m\right) w_{Np+j,Nq+k}\right. \\
& \qquad \left. + \frac{5}{3} v_{Np+j,Nq+k} - \left(\frac{5}{3} + 4C_m\right) v_{Np+j+1,Nq+k-1}\right) \\
& + \frac{3}{32\sqrt{2}} K_m \left(\left(1 + \frac{4}{3} C_m\right) w_{Np+j-1,Nq+k+1} - \left(1 - \frac{8}{3} C_m\right) w_{Np+j,Nq+k}\right. \\
& \qquad \left. + \frac{5}{3} v_{Np+j,Nq+k} - \left(\frac{5}{3} + 4C_m\right) v_{Np+j-1,Nq+k+1}\right) \\
& + \frac{3}{32\sqrt{2}} K_m \left(\left(1 + \frac{4}{3} C_m\right) w_{Np+j+1,Nq+k+1} - \left(1 - \frac{8}{3} C_m\right) w_{Np+j,Nq+k}\right. \\
& \qquad \left. + \left(\frac{5}{3} + 4C_m\right) v_{Np+j+1,Nq+k+1} - \frac{5}{3} v_{Np+j,Nq+k}\right) \\
& + \frac{3}{32\sqrt{2}} K_m \left(\left(1 + \frac{4}{3} C_m\right) w_{Np+j-1,Nq+k-1} - \left(1 - \frac{8}{3} C_m\right) w_{Np+j,Nq+k}\right. \\
& \qquad \left. + \left(\frac{5}{3} + 4C_m\right) v_{Np+j-1,Nq+k-1} - \frac{5}{3} v_{Np+j,Nq+k}\right). \qquad (6.16)
\end{aligned}
$$

Magnetic constants are

$$K_m = \frac{3\mu_0 v^2 |\vec{M}|^2}{\pi d_s^5} \text{ and } C_m = \frac{2d_s^2}{3L^2}\,, \tag{6.17}$$

with the assumption that identical magnet volume and magnetization exists throughout the lattice.

6.2 Infinite lattice analysis

The hypothetical periodic array of beams under consideration is made up of a finite number of N x N unit cells. However, it is simplest and valuable to first analyze an infinite lattice made up of these N x N cells. Since the lattice is infinite, the assumed wave solution for v and w oscillations is that of a wave with the form

$$v_{Np+j,Nq+k}(t) = A_{j,k} e^{i((Np+j)\gamma_w + (Nq+k)\gamma_v - \omega t)} \tag{6.18}$$

$$w_{Np+j,Nq+k}(t) = B_{j,k} e^{i((Np+j)\gamma_w + (Nq+k)\gamma_v - \omega t)}\,, \tag{6.19}$$

where $A_{j,k}$ and $B_{j,k}$ are wave amplitudes, γ_v and γ_w represent components of the wavevector $\vec{\gamma}$, and ω is the frequency of oscillation. Substitution of the these waveforms for each oscillator within the cell creates a system of equations for vibration in each periodically repeating cell. To connect the effects between cells, periodic boundary conditions are applied such that

$$A_{j-1,k} = A_{N,k} \quad \text{for } j = 1 \quad \text{and} \quad A_{j+1,k} = A_{1,k} \quad \text{for } j = N\,, \tag{6.20}$$

with equivalent expressions for k periodic boundaries and wave amplitudes B. Applying the periodic boundary conditions to the system equations and simplifying, a corresponding eigenvalue problem emerges

$$\left(\mathbf{G}(\gamma_v, \gamma_w) - \omega^2 \mathbf{I}\right) \vec{A} = \vec{0} \tag{6.21}$$

where $\mathbf{G}$ is a function of the two wavevector components, $\vec{A}$ is a $2N^2$ x 1 solution vector including both v and w wave amplitudes, $\mathbf{I}$ is a $2N^2$ x $2N^2$ identity matrix,

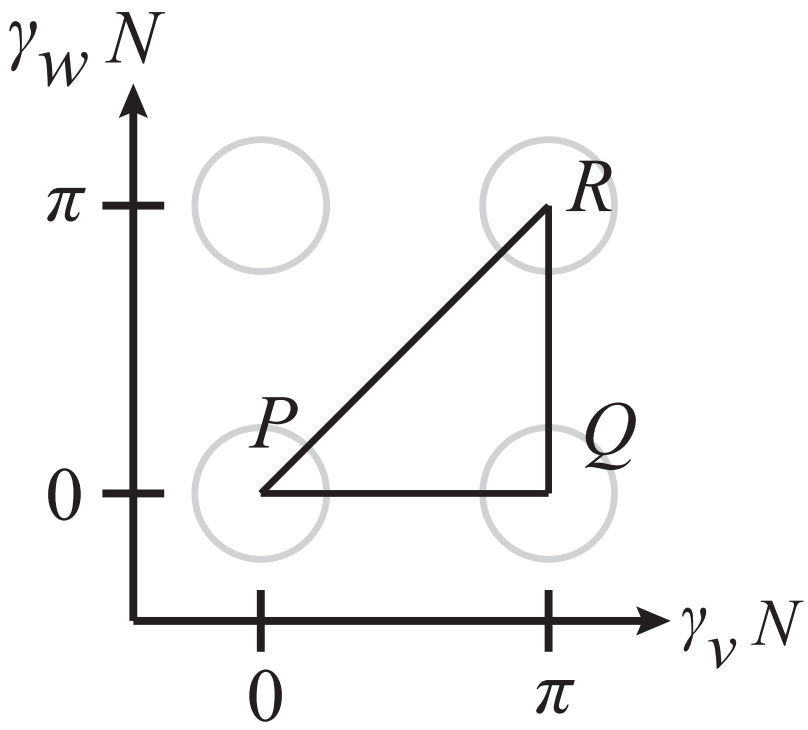

FIGURE 6.3: The Brillouin zone with boundary $P - Q - R - P$ for wavevector normalized by cell size N. It is along this path where extrema exist for the band structure.

and ω is the oscillation frequency. For these eigenvalue problems, analysis is not needed for all possible wavevectors. Figure 6.3 shows the two dimensional Brillouin zone, restricting the necessary analysis to the illustrated triangle for square unit cells as proven in Ref. [35]. Along the same lines, it has been shown that the eigenvalue problem only needs to be solved on the boundary encompassed by the triangle $P - Q - R - P$ where the wave propagation frequency extrema exist.

6.2.1 Exploration studies of the 2 x 2 unit cell

In this section, an infinite lattice made up of repeating 2 x 2 unit cells is explored. The homogeneous system of identical beams and tip masses with mass m_A creates a band structure with no gaps and propagation across a range of frequencies, as shown in Figure 6.4. The more interesting behavior occurs when the beam or mass

Table 6.1: Beam, magnet, and system parameters

Parameter	Value	Units
Linear mass density, m_l	8.23	g/m
Magnet volume, v	150.8	mm^3
Magnetization, $\|M\|$, Br/ μ_0	$1.32/(4\pi \times 10^{-7})$	T / (H/m)
Beam length, L	152.4	mm
Beam modulus of elasticity, E	2.3	GPa
Area moment, I_B	4.99	mm^4
Magnet plus additional tip mass A, m_A	1.3	g
Magnet plus additional tip mass B, m_B	2.3	g
Beam sparation distance, d_s	21.6	mm

properties are changed for varying configurations within the unit cell. For the case of this study, properties of the system are given in Table 6.1 with additional mass to the beam tips providing the periodic property variation.

In the first case, a single beam is given the larger mass m_B at its tip while the other three are given mass m_A. Figure 6.5 shows the resulting band structure for wave propagation as a function of the wavevector of the Brillouin zone boundary. Note the existence of a band gap in the frequency range 24.5 - 28.4 Hz.

The next configuration has the larger mass tips on two opposite corners of each cell. This propagation band structure is shown in Figure 6.6. Here the band gap has shifted to the frequency range 25.0 - 32.2 Hz for a larger frequency band gap.

The final configuration places the larger magnets next to one another in the unit cell. This periodicity creates the band structure for the propagation of waves shown in Figure 6.7. It is interesting to note the increase in propagation frequency bandwidth and decrease of the band gap to 27.3 - 28.4 Hz.

By varying the periodicity of the unit cell structure, different propagation patterns can be produced in the lattice. These patterns and resulting band gaps are sensitive to the parameters of the system. In the case of this magnet based system, variations in the tip mass and magnetization of the magnets can affect the band gap. The

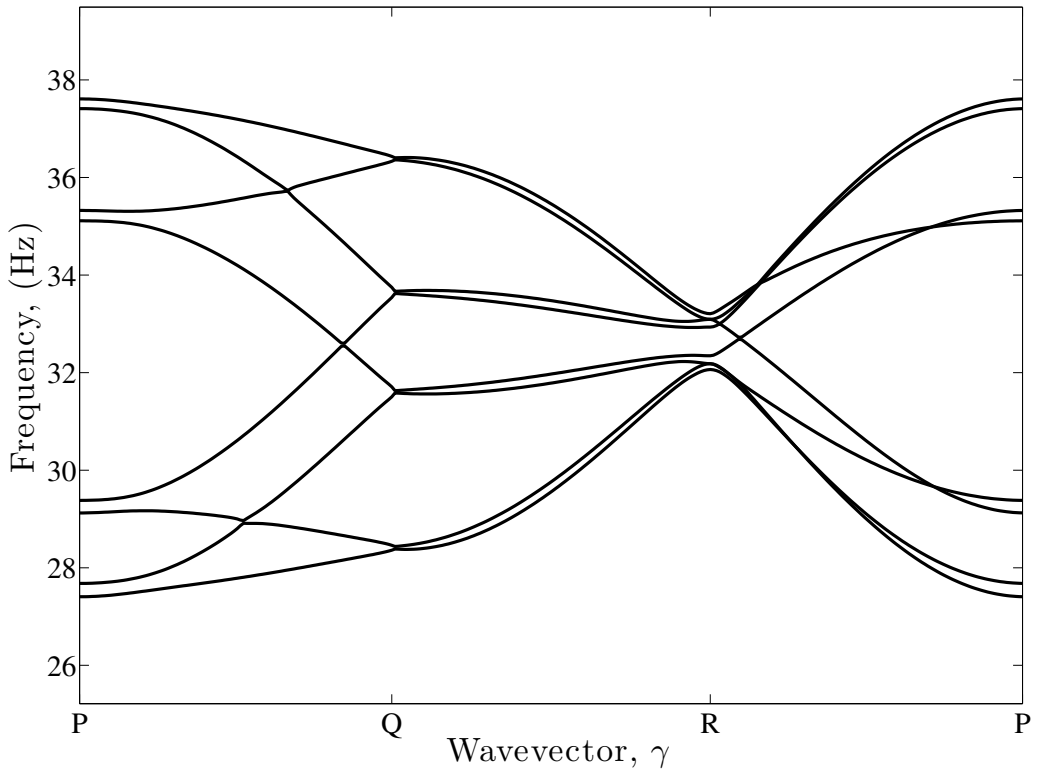

FIGURE 6.4: Band structure generated with system parameters given in Table 6.1 for a homogenous system with no property variation and tip mass m_A. This case provides a baseline structure for comparison with the periodically varied configurations.

propagation of this uncertainty is examined in the following section.

6.2.2 Uncertainty propagation

Variations in the tip mass and the remnant magnetization of the magnets can affect the band structure of the infinite lattice of 2 x 2 unit cells. For the sake of simplicity, this example assumes that the mass uncertainty manifests in a variation of the total effective mass $M_{v,w}$ multiplied by a factor. This factor has a Gaussian probability distribution

$$P_f(x) = \frac{1}{\sigma\sqrt{2\pi}} e^{-\frac{(x-\mu)^2}{2\sigma^2}}, \tag{6.22}$$

where x is the mass multiplying factor, σ is the standard deviation, and μ is the mean. For the multiplying factor, the mean $\mu = 1$ and the standard deviation is set

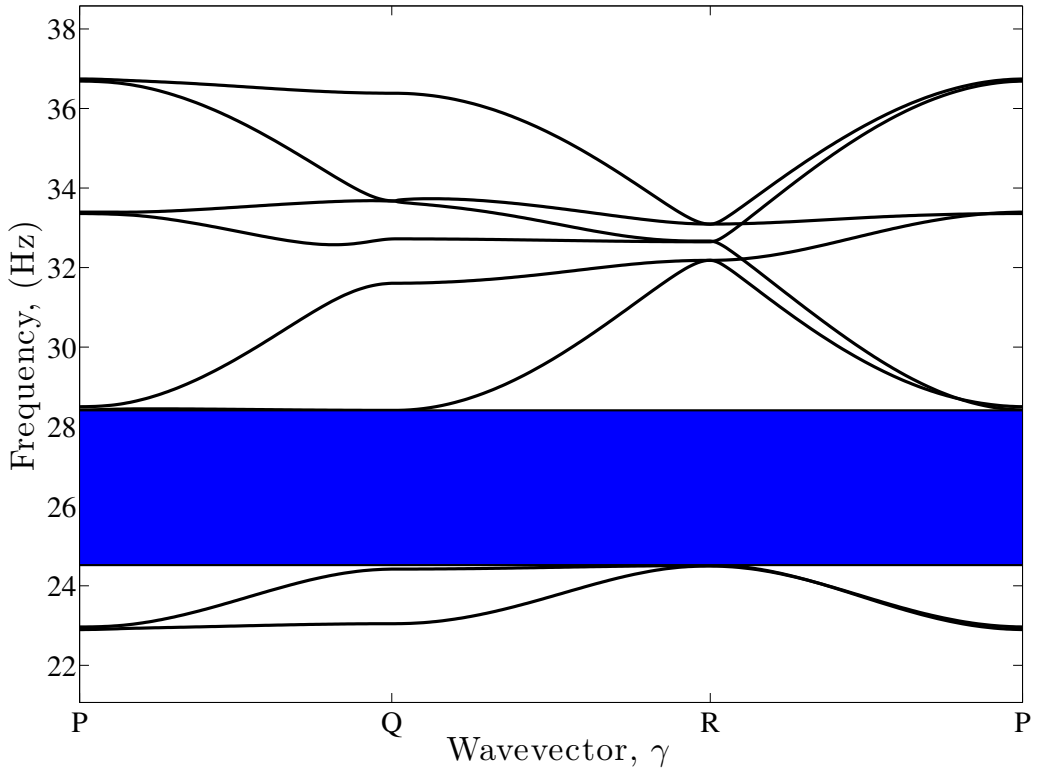

FIGURE 6.5: Band structure generated with system parameters given in Table 6.1 for a system with the larger tip mass m_B on a single beam and m_A on the other three. The region shaded in blue has no wave propagation at those frequencies.

to either $\sigma = 0.05$ or 0.075. The magnetization, however, is presumed to take on a more likely variation based on degradation of the magnetization of all magnets in the lattice system, perhaps due to temperature change [104]. For this uncertainty, it is assumed that the residual flux density Br of the magnets falls within a generalized extreme value (GEV) distribution having the form

$$P_f(x) = \frac{1}{\sigma}\left(1 + k\left(\frac{x-\mu}{\sigma}\right)\right)^{-1/k-1} \exp\left\{-\left(1 + k\left(\frac{x-\mu}{\sigma}\right)\right)^{-1/k}\right\}, \tag{6.23}$$

where x is the magnet Br, σ is the scale parameter, k is the shape parameter, and μ is the location parameter. This distribution allows for a maximum value and a leading tail distribution and is used to approximate the residual flux in an environment subjected to temperature increases that can cause magnetization degradation. The

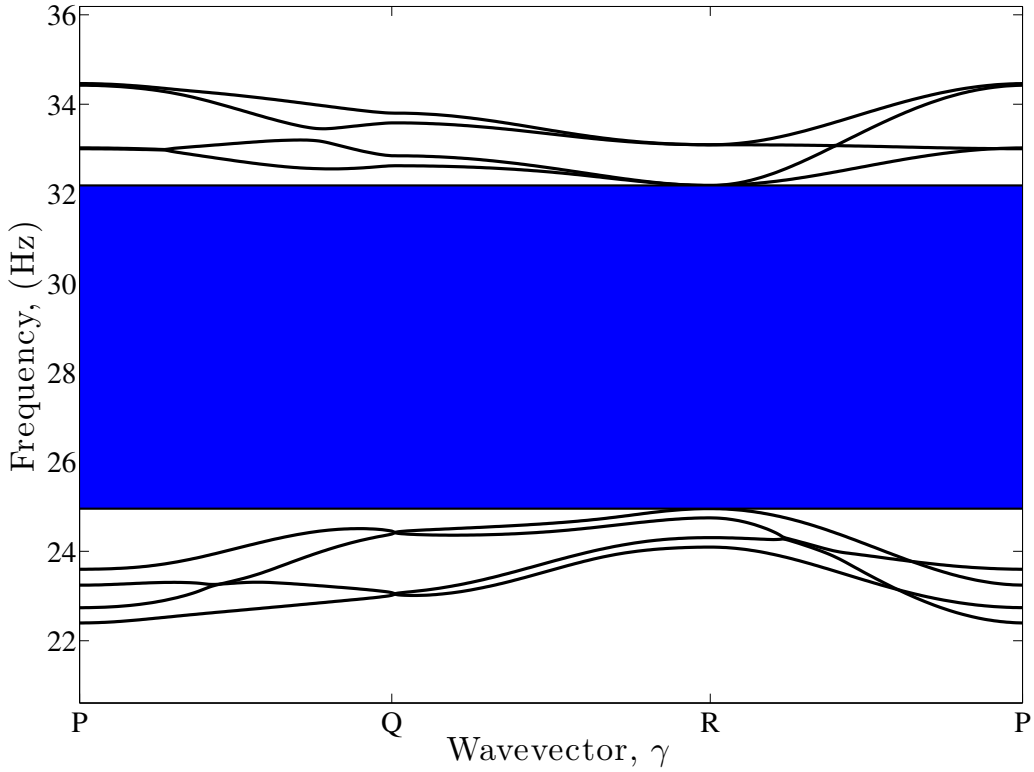

FIGURE 6.6: Band structure generated with system parameters given in Table 6.1 for a system with the larger tip mass m_B on two beams diagonally across the unit cell from one another. The region shaded in blue has no wave propagation at those frequencies.

maximum value is the result of the theoretical maximum residual flux output for the neodymium magnet material utilized by this device.

Two levels of uncertainty are used in this test in order to conduct a Monte Carlo simulation of 10000 trials. Using the given probability distributions, values for the residual flux density and the mass multiplying factor are chosen and the system solved for the wave response. This is repeated for 10000 trials. The mass multiplying factor distributions and residual flux density distributions are shown in Figure 6.8 for a small level (red) and a larger level (blue) of uncertainty. The first distribution uses a mass factor Gaussian distribution with mean factor 1 and a standard deviation of only 0.05, while Br has maximum value 1.32 T, and GEV distribution parameters for

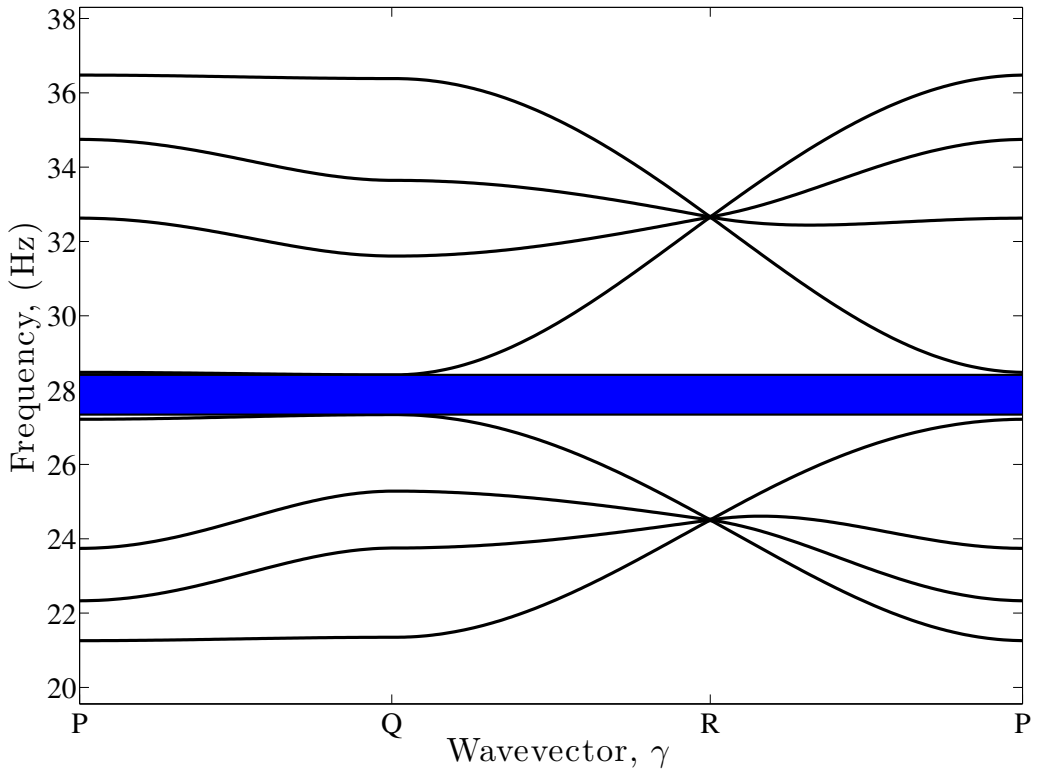

FIGURE 6.7: Band structure generated with system parameters given in Table 6.1 for a system with the larger tip mass m_B on two beams positioned on the same side of the cell. The region shaded in blue has no wave propagation at those frequencies.

the shape $k = -0.7$, scale $\sigma = 0.1$, and location $\mu = 1.18$. The second distribution has a larger level of uncertainty with a mass Gaussian distribution with mean factor 1 and a standard deviation of 0.075 and Br with maximum value 1.32 T, and GEV distribution parameters of $k = -0.6$, $\sigma = 0.15$, and $\mu = 1.07$.

Two different configurations shown previously were examined for uncertainty effects. The first was the configuration with a single m_B tip mass and three other m_A masses and had an idealized band structure shown in Fig. 6.5. Uncertainty in this system for the first level is shown in Figure 6.9 with the larger level shown in Figure 6.10. The larger uncertainty in parameters leads to a larger uncertainty and a more flat distribution of band gaps due a spreading of the distribution of the high and low frequency values for the band structure.

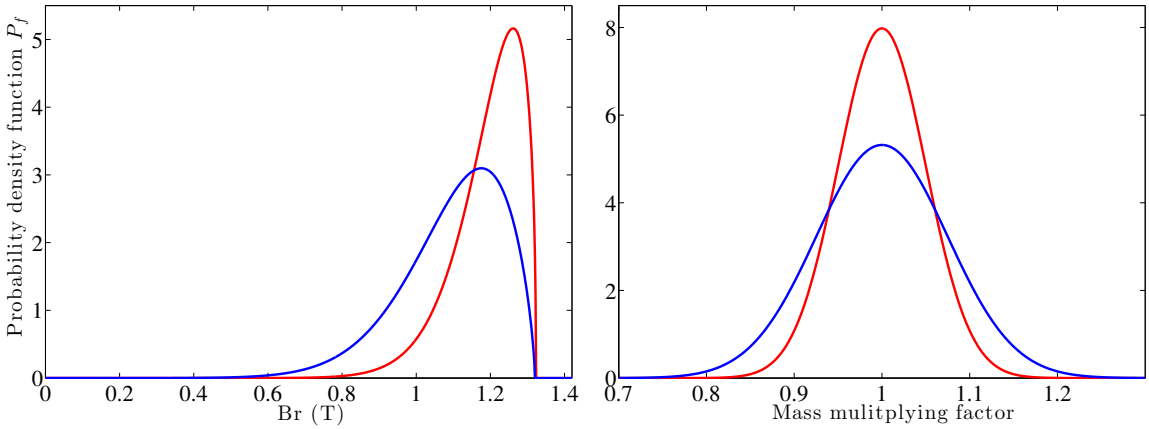

FIGURE 6.8: Probability density functions for low levels (red) and high levels (blue) of parametric uncertainty of the residual flux density Br and the mass multiplying factor.

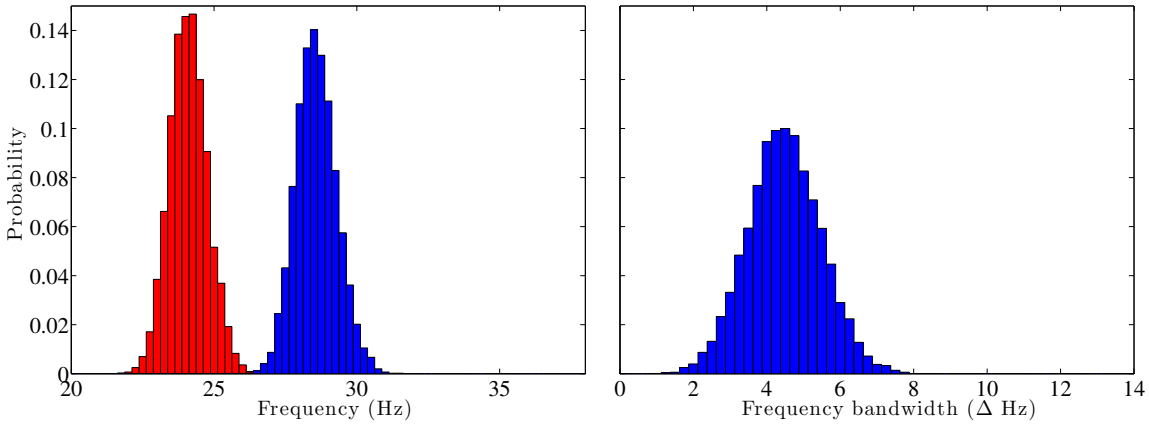

FIGURE 6.9: Monte Carlo trial probabilities for the lower (red) and higher (blue) boundary frequencies for the band structure gap a) and the bandwidth of said gap b) for the band structure in Figure 6.5. Trials were generated with the lower uncertainty probability density functions shown in red in Figure 6.8.

The second configuration examined was the double m_B tip mass at diagonal from one another with m_A for the other masses. The idealized band structure for this unit cell type is shown in Fig. 6.6. Uncertainty in this system for the first level is shown in Figure 6.11 with the larger level shown in Figure 6.12. Much like the first configuration, the larger uncertainty in parameters leads to a spreading of the distributions and greater uncertainty in the band gap size. Due to the larger idealized

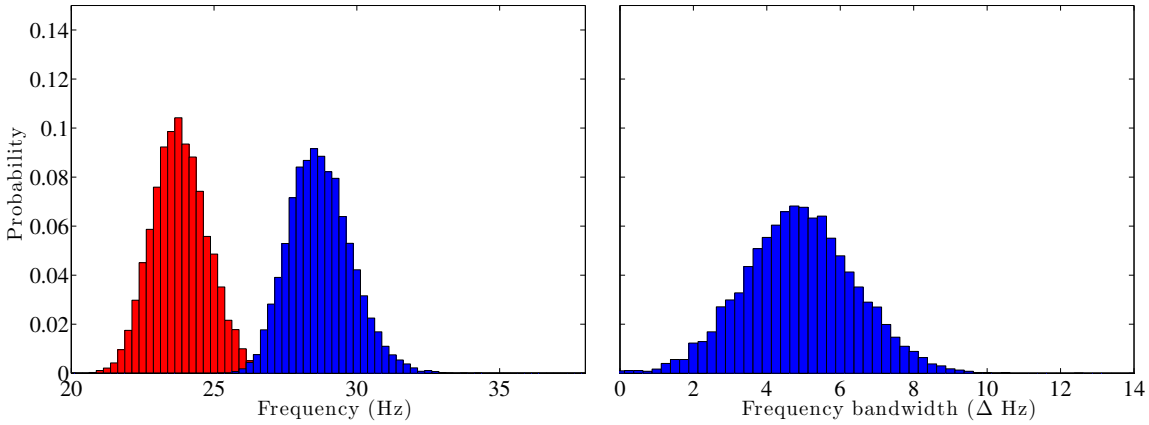

FIGURE 6.10: Monte Carlo trial probabilities for the lower (red) and higher (blue) boundary frequencies for the band structure gap a) and the bandwidth of said gap b) for the band structure in Figure 6.5. Trials were generated with the higher uncertainty probability density functions shown in blue in Figure 6.8.

band gap, the likelihood that the large variation results in a completely degraded gap is very small.

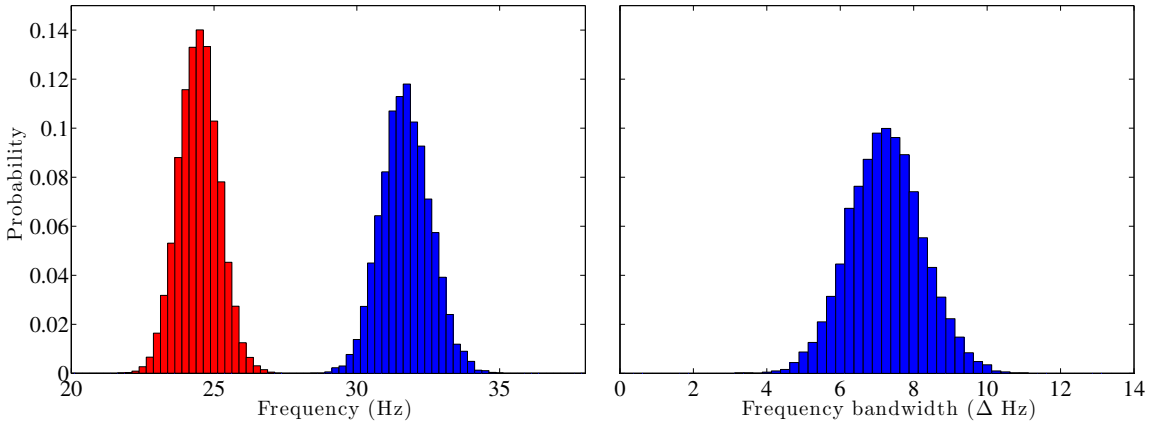

FIGURE 6.11: Monte Carlo trial probabilities for the lower (red) and higher (blue) boundary frequencies for the band structure gap a) and the bandwidth of said gap b) for the band structure in Figure 6.6. Trials were generated with the lower uncertainty probability density functions shown in red in Figure 6.8.

The Monte Carlo analysis indicates that larger levels of uncertainty manifest in a larger set of possible values for the frequency gap in the band structure. For low uncertainty the gaps show concentration about a mean level, while for the larger uncertainty levels in mass and magnetization result in a large uncertainty, meaning

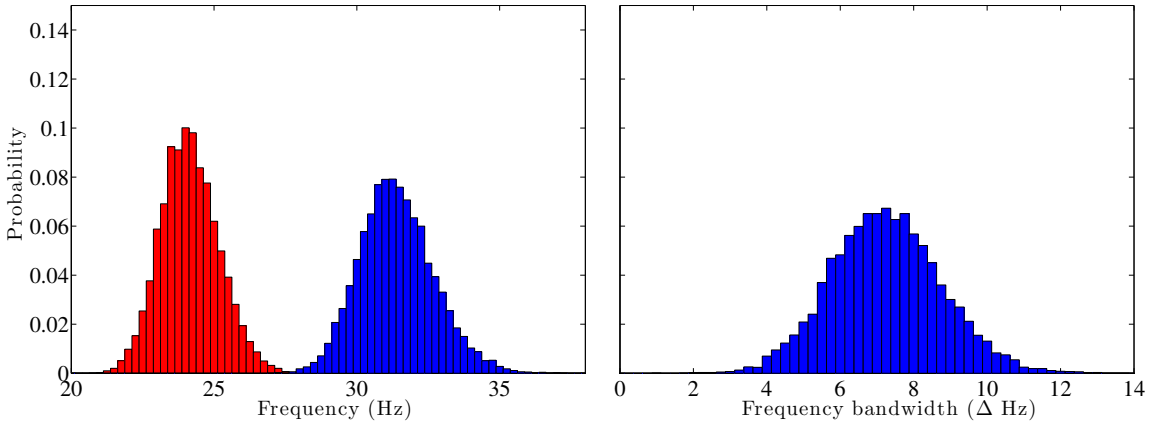

FIGURE 6.12: Monte Carlo trial probabilities for the lower (red) and higher (blue) boundary frequencies for the band structure gap a) and the bandwidth of said gap b) for the band structure in Figure 6.6. Trials were generated with the lower uncertainty probability density functions shown in blue in Figure 6.8.

a wider frequency bandwidth range and a flatter distribution of bandwidth values.

6.3 Finite system

While the infinite analysis provides an idealistic examination of the system, a more relevant approach for experimental considerations takes into account the finite nature of the physical system, as well as the effects of viscous damping on the oscillations.

Given a finite system of H x H unit cells of size N x N, a solution displacement vector with length $2\,(NH)^2$ exists for oscillations in both directions. The equation that governs the oscillations is

$$[M]\ddot{\vec{q}} + [C]\dot{\vec{q}} + [K]\vec{q} = \vec{0} \tag{6.24}$$

where $[M]$, $[C]$, and $[K]$ are the mass, viscous modal damping, and stiffness matrices, respectively. The displacement solution

$$\vec{q} = \vec{a}e^{i\Omega t} \tag{6.25}$$

represents oscillations of frequency Ω in both directions with the first $(NH)^2$ vector terms for v and the second $(NH)^2$ terms for w. Excitation is introduced by pre-

scribing the motion of a single magnet in the w direction to an acceleration with amplitude $0.5 \times g$ where g is the acceleration of gravity or 9.81 m/s^2. The damping matrix $[C]$ is presumed to be diagonal with components $c_{Np+j,Nq+k} = 2\zeta\sqrt{M_{j,k}K_{v,w}}$.

System solutions are found first by finding the equilibrium positions resulting from the nonlinear magnet interactions for each oscillator. The negative of the Jacobian matrix about from these equilibrium positions acts as the stiffness matrix $[K]$ and is used to solve for oscillation amplitudes $\vec{a}$ of Eq. 6.25.

The diagonal m_B in the 2 x 2 mass configuration was used to compare the finite lattice results with the infinite system results. The following figures show the frequency response function (FRF) for oscillation acceleration relative to input forcing for the v and w directions for subfigure a) and b) with system parameters in Table 6.1. Figure 6.13 illustrates the system dependence on the size of the lattice for $H = 5$, 13, and 21 and $\zeta = 0.001$. Figure 6.14 likewise illustrates the system dependence on the damping coefficient for $\zeta = 0.001$, 0.01, and 0.04 and $H = 13$. The dependence on the number of oscillators manifests in a frequency response function with a more pronounced band gap as the number of cells increases and the boundary-less infinite behavior is approached. For $H = 5$ the band gap exists but has an attenuation that is significantly less than the larger lattices. For the damping comparison, an increase in the damping coefficient corresponds to a smoothing and flattening of the band structure. For very low damping, the frequency response function has significant attenuation in the infinite lattice band gap region. As damping increases, the attenuation within the bad gap is comparable, albeit smoother, however the peak values relative to the prescribed excitation are significantly lower.

6.4 Conclusions

This chapter provides a theoretical exploration of a hypothetical macro scale energy filtering system with periodically varying properties and band gap behavior. Modeled

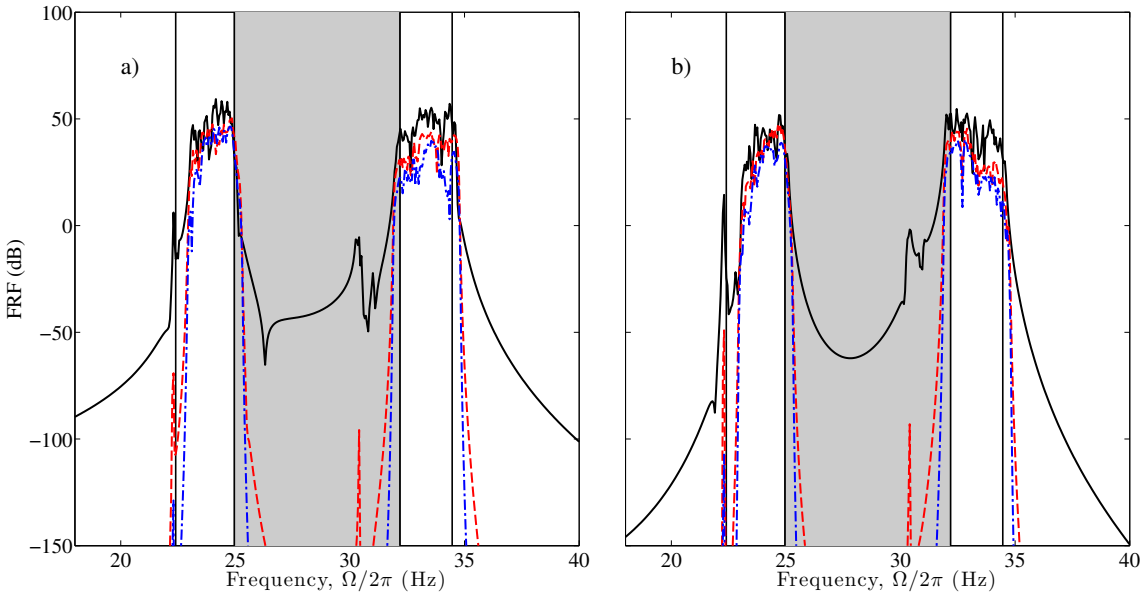

FIGURE 6.13: Frequency response function in decibels for the acceleration of the oscillator at $q = H/2 + 1$, $p = H$, $j = N$, $k = 1$ for changing numbers of unit cells H. The solid, dashed, and dash-dot line represent $H = 5$, 13, and 21, respectively. The grey region with black boarders represents the band structure gap from Figure 6.6 while the other vertical black lines represent the lower and upper propagation limits. System parameters used are found in Table 6.1 with $\zeta = 0.001$.

after phononic and photonic wave filtering systems, this larger system shows band structures with gaps in wave propagation for the idealized infinite system, with or without parametric uncertainty, and the more realistic finite system. Using magnetic tip masses and the elasticity of beams, a hypothetical system of 2 x 2 unit cells is proposed and analyzed.

The analysis first considers an infinite system of repeating 2 x 2 unit cells. The array is assumed to have either consistent, homogenous properties within each cell and thus throughout the array or non-homogenous properties in the 2 x 2 and thus periodic property variation throughout the array. The homogeneous configuration of the 2 x 2 unit cell with a gapless band structure was compared to three separate non-homogenous configurations. These configurations showed gaps in wave propagation with a shifting size and frequency location.

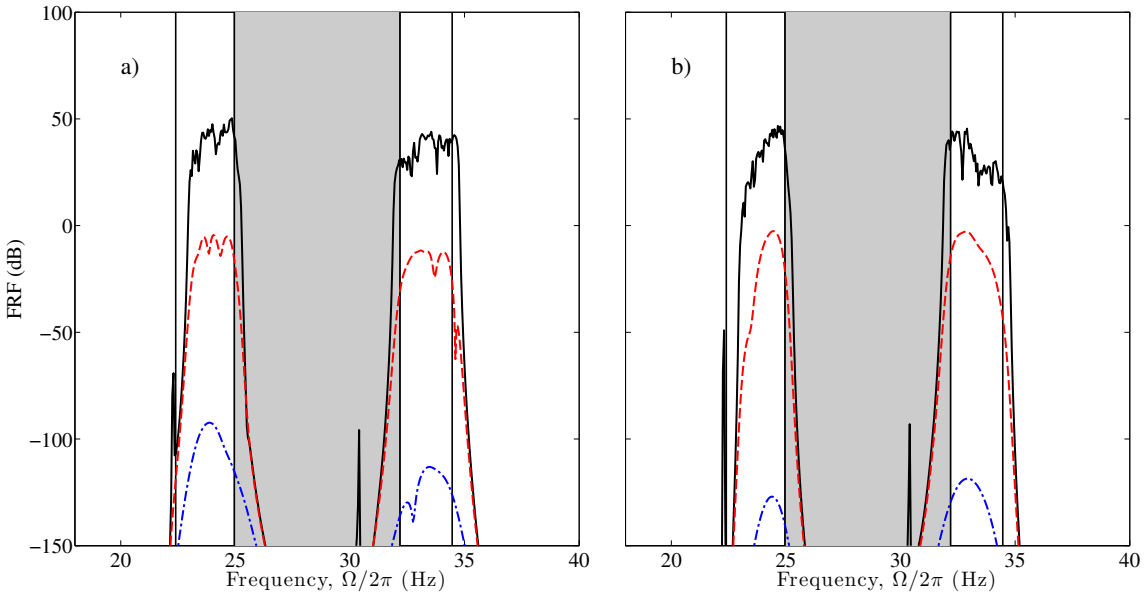

FIGURE 6.14: Frequency response function in decibels for the acceleration of the oscillator at $q = H/2 + 1$, $p = H$, $j = N$, $k = 1$ for changing damping ratio ζ. The solid, dashed, and dash-dot line represent $\zeta = 0.001$, 0.01, and 0.04, respectively. The grey region with black boarders represents the band structure gap from Figure 6.6 while the other vertical black lines represent the lower and upper propagation limits. System parameters used are found in Table 6.1 with $H = 13$.

Recognizing the existence of uncertainty in physical systems, an uncertainty analysis was performed for variations of the mass and residual flux density of the tip magnets. This analysis revealed that uncertainty in the parameters can cause changes in the band gap location and size. It is this uncertain bandwidth and frequency location that could be detrimental to the behavioral function of these band gap systems.

Furthermore, a more realistic, finite manifestation of the hypothetical was analyzed with considerations for boundary conditions and damping that are ignored in the infinite system characterization. These additional factors are shown to cause erosion of the band gap structure, however not completely, as considerable signal attenuation is still visible in the expected regions.

The exploration of this hypothetical macro-scale system provides a basis for experimental examinations, as well as a proof of concept for band gap structures in

low frequency applications. For real systems, the uncertainty associated with variations in material properties along with the considerations of boundary conditions and damping indicate that careful design and construction are important in ensuring that the theorized band gap behavior is realized in the physical system.

7

Summary

This doctoral dissertation has explored the dynamics of systems with nonlinear, magnetic interactions within the framework of energy harvesting and filtering. Nonlinearity has been utilized to more fully capture environmental vibrations and add complexity to the basic behavior of prototypically linear systems. The developments of this work include a method of analysis for nonlinear tip interactions of cantilever beams, a comparative study on the effects of nonlinear electromagnetic coupling in otherwise linear mechanical systems, a two beam, bistable oscillating system with the potential for energy harvesting, and the low-frequency band gap behavioral exploration of a two dimensional array.

7.1 Conclusions

In Chapter 2, energy harvesting systems with four classes of resorting forces were analyzed using harmonic balance. These classes were: linear, softening, hardening, and bistable. The linear system showed the expected resonant peak near the natural frequency, while the nonlinear systems were more complex. These systems showed an increased power bandwidth, with the softening system having a peak that bent

towards lower frequencies and the hardening having a higher frequency lean. The bistable harvester showed a larger power potential at low frequencies with a well mixing solution. Each of the nonlinear systems conveyed the existence of coexisting solutions with off-resonance usable power not present in the linear harvester. The robustness of the nonlinear systems to changing primary excitation frequencies or input powers illustrated the advance of such systems over their linear counterparts.

Chapter 3 looked at the effects of highly nonlinear boundary interactions on beam dynamics for a cantilever beam. Using a weakly nonlinear beam stiffness approximation, the system was analyzed to find analytical mode shapes both with and without the nonlinear magnetic tip forces. The chapter first explored the linear cantilever system with considerations for adjustments to tip mass, tip mass offset, and rotational inertia effects. Then a finessed approach using admissible functions and Rayleigh-Ritz energy methods was used on the nonlinear tip force system to find static deflections, mode shapes, and natural frequencies. This chapter's use of approximate numerical methods like Rayleigh-Ritz highlighted the care needed in these highly nonlinear systems for admissible analysis.

Chapter 4 investigated the response of an energy harvester that uses electromagnetic induction to convert ambient vibration into electrical energy. The chapter work compared the system's response behavior when either a linear or a physically motivated form of nonlinear coupling is applied. The motivation for the chapter was the prospect that nonlinear coupling could be used to improve the performance of an energy harvester by broadening its frequency response. Combined theoretical and numerical studies were utilized to investigate the harvester's response for both single and multi-frequency base excitation. The chapter showed the results of investigations that unveiled regions in the parameter space where nonlinear coupling is better than linear coupling and regions where the opposite is true. The meaningful conclusion of this chapter study was that nonlinear coupling can sometimes be detrimental, but it

can also be beneficial if properly designed into the system.

In Chapter 5, a two beam, magnetically coupled, bistable oscillator system was investigated from the perspective of its integration into an energy harvester. The system consists of two carbon fiber cantilever beams with attached magnetic tip masses. The chapter derived governing equations and provided a numerical analysis of the system. A rich array of phenomenological behavior including static bifurcations, chaotic oscillations, and sub-harmonic orbits were unveiled. The phenomenological behaviors found in the experiments were then compared with those obtained via numerical studies. Observations were then made from an energy harvesting perspective on the advantages and disadvantages of using this highly nonlinear system as a vibratory harvester.

Chapter 6 explored the band structure of a two dimensional lattice of oscillating beams with magnetic tip masses. The chapter primarily focused on regions in the band structure where wave propagation does not occur in the infinite permutation of the system due to periodically varying the mass properties. For certain configurations of the 2 x 2 repeating unit cell, it was shown that the frequency band gaps manifest in different sizes and band locations. The uncertainty in the band gap regions was additionally analyzed, using uncertainties associated with specific physical parameters, to elucidate their influence on the band gap regions. Uncertainties in the physical system were thus shown to causes changes in the band gaps that could be detrimental to the filtering properties of the system. Boundary effects and damping were also investigated for a finite-dimensional array, which shows an erosion of band gaps that could limit the expected functionality.

7.2 Future work

The studies outlined above have numerous possibilities for future expansion. The potential new investigations are organized by the relevance to a chapter detailed in

this work including Chapter 3 on nonlinear tip interactions for a cantilever beam, Chapter 4 on nonlinear coupling in linear systems, Chapter 5 on a two beam, magnetically coupled bistable oscillator system, and Chapter 6 on the band structure of a two dimensional lattice of oscillating beams with magnetic tip masses.

7.2.1 Nonlinear tip interactions of a cantilever beam

The work detailed in Chapter 3 has a few areas of expansion related to the mode shape analysis and its application. Instead of using a carbon fiber beam, the analysis can expand to an energy harvesting system with a piezo-electric strip or piezo-ceramic beam. The ability to select the first mode frequency by changing the magnet separation distance would be a valuable tool in changing dynamic systems, allowing for adaptability in the system. Beyond that, the potential for multi-mode excitation in stochastic or multi-frequency environments could allow for higher utilization of environmental vibrations.

Another adaptation that deserves a separate study is the inclusion of additional magnets or the shifting of a single magnet radially from the beam's primary axis. This could create asymmetric potential energy signatures with different frequency characteristics for different deflections. Such potential energy manipulation could provide additional assistance in energy harvesting systems with complex, multi-frequency environmental vibrations.

7.2.2 Linear and nonlinear coupling models

Chapter 4 provided a detailed look at a nonlinear coupling model for a linear mechanical oscillator. A clear future direction is an analysis for nonlinear mechanical oscillators with hardening, softening, or bistable restoring forces. A similarly detailed analysis of single and multi-frequency excitations in a system with nonlinearity in both the electrical and mechanical system deserves a full study. Such a system could

likewise show advantages for coil placement much like the analysis of the linear mechanical system.

A second area of expansion is the use of multiple coils with alternating coil wind direction. The alternating wind direction combined with the use of multiple coils could allow for a nonlinear coupling with a different coil flux shapes. These changes could prove to have advantages that expand on those found in the chapter.

7.2.3 Two beam system with a bistability from magnetic coupling

The bistable two beam system shows potential for energy harvesting. The numerical and experimental analysis provided a basis for this potential exploration, but an analytical exploration could highlight particular advantages of this system design. Because of the highly nonlinear nature, numerical continuation would be the most likely method of analysis to unveil the complex spectral characteristics of the system and the effects of damping changes on the system.

The next expansion would be a full scale energy harvesting study with an included electrical coupling mechanism, either electromagnetic or piezoelectric transduction, and an electrical system. Such a study would provide for energy harvesting comparisons with single oscillator systems or uncoupled two beam systems. Likewise, the effects of electrical coupling on the system dynamics could be explored as it relates to the power potential of the harvesting device.

Another future direction is the use of multiple coupled oscillators. A full exploration of such a system's potential for synchronization would provide a novel look at nonlinear coupled synchronous systems. Work could focus on the potential for synchronized oscillations that allow for higher collective power generation.

7.2.4 Two dimensional lattice of beams with magnetic tip masses

The hypothetical two dimensional band gap system explored in Chapter 6 highlighted the potential for these systems for application in low frequency filtering. The construction of such a system would act as an obvious first step for future work with these systems. An exhaustive physical study could detail the effects of damping, limitations on lattice size, and variations in the material and geometric characteristics of the system.

Another analytical study potential lies in the inclusion of non-periodic changes in the properties. Such a disruption, either in the form of a line or curve of different cells or just a single different cell has shown potential in lattice systems to filter or disperse energy differently. A complete study on the energy directive potential and its application beyond energy filtering and into the harvesting realm could be valuable as well.

Bibliography

[1] S. P. Beeby, M. J. Tudor, N. M. White, Energy harvesting vibration sources for microsystems applications, Measurement Science and Technology 17 (12) (2006) R175–R195.

[2] J. Paradiso, T. Starner, Energy scavenging for mobile and wireless electronics, Pervasive Computing, IEEE 4 (1) (2005) 18–27.

[3] V. Bedekar, J. Oliver, S. Priya, Pen harvester for powering a pulse rate sensor, Journal of Physics D: Applied Physics 42 (10) (2009) 105105.

[4] C. C. McGehee, Dynamics of an ocean energy harvester, Ph.D. thesis, Duke University (2013).

[5] C. Saha, T. O'Donnell, N. Wang, P. McCloskey, Electromagnetic generator for harvesting energy from human motion, Sensors and Actuators A: Physical 147 (1) (2008) 248–253.

[6] M. Lallart, S. R. Anton, D. J. Inman, Frequency self-tuning scheme for broadband vibration energy harvesting, Journal of Intelligent Material Systems and Structures 21 (9) (2010) 897–906.

[7] I. Sari, T. Balkan, H. Kulah, An electromagnetic micro power generator for wideband environmental vibrations, Sensors and Actuators A: Physical 145-146 (2008) 405–413.

[8] C. B. Williams, R. B. Yates, Analysis of a micro-electric generator for microsystems, Sensors and Actuators A: Physical 52 (1-3) (1996) 8–11.

[9] B. Mann, N. Sims, Energy harvesting from the nonlinear oscillations of magnetic levitation, Journal of Sound and Vibration 319 (1-2) (2009) 515–530.

[10] E. S. Leland, P. K. Wright, Resonance tuning of piezoelectric vibration energy scavenging generators using compressive axial preload, Smart Materials and Structures 15 (5) (2006) 1413–1420.

[11] S. Roundy, Y. Zhang, Toward self-tuning adaptive vibration-based microgenerators, in: Smart Materials, Nano-, and Micro-Smart Systems, International Society for Optics and Photonics, 2005, pp. 373–384.

[12] S. P. Beeby, R. N. Torah, M. J. Tudor, P. Glynne-Jones, T. O'Donnell, C. R. Saha, S. Roy, A micro electromagnetic generator for vibration energy harvesting, Journal of Micromechanics and Microengineering 17 (7) (2007) 1257–1265.

[13] B. Mann, B. Owens, Investigations of a nonlinear energy harvester with a bistable potential well, Journal of Sound and Vibration 329 (9) (2010) 1215–1226.

[14] B. Mann, N. Sims, On the performance and resonant frequency of electromagnetic induction energy harvesters, Journal of Sound and Vibration 329 (9) (2010) 1348–1361.

[15] A. F. Arrieta, P. Hagedorn, A. Erturk, D. J. Inman, A piezoelectric bistable plate for nonlinear broadband energy harvesting, Applied Physics Letters 97 (10) (2010) 104102–3.

[16] S. C. Stanton, C. C. McGehee, B. P. Mann, Nonlinear dynamics for broadband energy harvesting: Investigation of a bistable piezoelectric inertial generator, Physica D: Nonlinear Phenomena 239 (10) (2010) 640–653.

[17] A. Erturk, D. Inman, Broadband piezoelectric power generation on high-energy orbits of the bistable duffing oscillator with electromechanical coupling, Journal of Sound and Vibration 330 (10) (2011) 2339–2353.

[18] S. Stanton, Nonlinear electroelastic dynamical systems for inertial power generation, Ph.D. thesis, Duke University (2011).

[19] S. Shahruz, Design of mechanical band-pass filters for energy scavenging: Multi-degree-of-freedom models, Journal of Vibration and Control 14 (5) (2008) 753–768.

[20] R. Ramlan, M. Brennan, B. Mace, I. Kovacic, Potential benefits of a non-linear stiffness in an energy harvesting device, Nonlinear Dynamics 59 (4) (2010) 545–558.

[21] C. McInnes, D. Gorman, M. Cartmell, Enhanced vibrational energy harvesting using nonlinear stochastic resonance, Journal of Sound and Vibration 318 (45) (2008) 655–662.

[22] M. F. Daqaq, Transduction of a bistable inductive generator driven by white and exponentially correlated gaussian noise, Journal of Sound and Vibration 330 (11) (2011) 2554–2564.

[23] L. Gammaitoni, I. Neri, H. Vocca, Nonlinear oscillators for vibration energy harvesting, Applied Physics Letters 94 (16) (2009) 164102–3.

[24] T. D. Drysdale, R. J. Blaikie, D. R. S. Cumming, Calculated and measured transmittance of a tunable metallic photonic crystal filter for terahertz frequencies, Applied Physics Letters 83 (26) (2003) 5362–5364.

[25] S. Y. Lin, J. G. Fleming, D. L. Hetherington, B. K. Smith, R. Biswas, K. M. Ho, M. M. Sigalas, W. Zubrzycki, S. R. Kurtz, J. Bur, A three-dimensional photonic crystal operating at infrared wavelengths, Nature 394 (6690) (1998) 251–253.

[26] J. D. Joannopoulos, S. G. Johnson, J. N. Winn, R. D. Meade, Photonic crystals: molding the flow of light, Princeton, N.J. : Princeton University Press, 2011.

[27] R. Cregan, B. Mangan, J. Knight, T. Birks, P. S. J. Russell, P. Roberts, D. Allan, Single-mode photonic band gap guidance of light in air, Science 285 (5433) (1999) 1537–1539.

[28] P. S. J. Russell, Photonic band gaps, Physics World 5 (8) (1992) 37–42.

[29] P. G. Martinsson, A. B. Movchan, Vibrations of lattice structures and phononic band gaps, The Quarterly Journal of Mechanics and Applied Mathematics 56 (1) (2003) 45–64.

[30] I. El-Kady, R. H. Olsson, J. G. Fleming, Phononic band-gap crystals for radio frequency communications, Applied Physics Letters 92 (23) (2008) 233504–233504–3.

[31] C. Goffaux, J. P. Vigneron, Theoretical study of a tunable phononic band gap system, Phys. Rev. B 64 (7) (2001) 075118.

[32] M. I. Hussein, M. J. Frazier, Band structure of phononic crystals with general damping, J. Appl. Phys. 108 (9) (2010) 093506–11.

[33] J. Jensen, Phononic band gaps and vibrations in one- and two-dimensional mass-spring structures, Journal of Sound and Vibration 266 (5) (2003) 1053–1078.

[34] O. Sigmund, J. Sndergaard Jensen, Systematic design of phononic bandgap materials and structures by topology optimization, Philosophical Transactions of the Royal Society of London. Series A: Mathematical, Physical and Engineering Sciences 361 (1806) (2003) 1001–1019.

[35] L. Brillouin, Wave propagation in periodic structures; electric filters and crystal lattices, New York : Dover Publications, 1953.

[36] B. P. Bernard, B. A. M. Owens, B. P. Mann, Uncertainty propagation in the band gap structure of a 1d array of magnetically coupled oscillators, Journal of Vibration and Acoustics 135 (4) (2013) 041005–041005.

[37] Y. Xiao, J. Wen, D. Yu, X. Wen, Flexural wave propagation in beams with periodically attached vibration absorbers: Band-gap behavior and band formation mechanisms, Journal of Sound and Vibration 332 (4) (2013) 867–893.

[38] J. D. Logan, Applied Mathematics, Hoboken, N.J. : Wiley-Interscience, 2006.

[39] D. T. Greenwood, Advanced dynamics, Cambridge: Cambridge University Press, 2003.

[40] K. W. Yung, P. B. Landecker, D. D. Villani, An analytic solution for the force between two magnetic dipoles, Magnetic and Electrical Separation 9 (1) (1998) 39–52.

[41] P. B. Landecker, D. D. Villani, K. W. Yung, An analytic solution for the torque between two magnetic dipoles, Magnetic and Electrical Separation 10 (1) (1999) 29–33.

[42] B. A. Owens, B. P. Mann, Mode shape analysis for nonlinear tip interactions of a cantilever beam, Journal of Sound and Vibration (2014) in review.

[43] B. A. Owens, B. P. Mann, Linear and nonlinear electromagnetic coupling models in vibration-based energy harvesting, Journal of Sound and Vibration 331 (4) (2012) 922–937.

[44] B. A. Owens, B. P. Mann, Energy harvesting perspectives for a two beam system with a bistability from magnetic coupling, International Journal of Non-Linear Mechanics (2014) in review.

[45] B. A. Owens, B. P. Mann, Wave propagation, band gaps, and uncertainty in a 2-d lattice of beams with magnetic tip masses, Mechanical Systems and Signal Processing.

[46] A. Erturk, J. Hoffmann, D. J. Inman, A piezomagnetoelastic structure for broadband vibration energy harvesting, Applied Physics Letters 94 (25) (2009) 254102–3.

[47] A. Preumont, Mechatronics : Dynamics of Electromechanical and Piezoelectric Systems, Dordrecht : Springer, 2006.

[48] L. Meirovitch, Principles and techniques of vibrations, Upper Saddle River, NJ : Prentice Hall, 1997.

[49] T. Wang, Nonlinear bending of beams with concentrated loads, Journal of the Franklin Institute 285 (5) (1968) 386–390.

[50] T. Wang, Non-linear bending of beams with uniformly distributed loads, International Journal of Non-Linear Mechanics 4 (4) (1969) 389–395.

[51] J. Holden, On the finite deflections of thin beams, International Journal of Solids and Structures 8 (8) (1972) 1051–1055.

[52] H. H. Denman, R. Schmidt, An approximate method of analysis of large deflections, Zeitschrift fr angewandte Mathematik und Physik ZAMP 21 (3) (1970) 412–421.

[53] S. Timoshenko, Theory of elastic stability, New York : McGraw-Hill Book Company, 1936.

[54] J. G. Eisley, Large amplitude vibration of buckled beams and rectangular plates, AIAA Journal 2 (12) (1964) 2207–2209.

[55] J. Genin, H. Radwan, Nonlinear bending inertia of a vibrating beam, Journal of Applied Mathematics and Physics 21 (6) (1970) 983–990.

[56] K. Bisshopp, D. Drucker, Large deflection of cantilever beams, Quarterly of Applied Mathematics 3 (1) (1945) 272–275.

[57] Y. Tada, G. C. Lee, Finite element solution to an elastica problem of beams, International Journal for Numerical Methods in Engineering 2 (2) (1970) 229–241.

[58] H. Hibbitt, P. Marcal, J. Rice, A finite element formulation for problems of large strain and large displacement, International Journal of Solids and Structures 6 (8) (1970) 1069–1086.

[59] A. Luongo, R. Rega, F. Vestroni, Non-resonant non-planar free motions of inextensional non-compact beams, Journal of Sound and Vibration 134 (1) (1989) 73–86.

[60] J. Turner, Non-linear vibrations of a beam with cantilever-hertzian contact boundary conditions, Journal of Sound and Vibration 275 (12) (2004) 177–191.

[61] S. Crandall, The role of damping in vibration theory, Journal of Sound and Vibration 11 (1) (1970) 3–IN1.

[62] M. Da Silva, Non-linear flexural-flexural-torsional-extensional dynamics of beams, i. formulation, International Journal of Solids and Structures 24 (12) (1988) 1225–1234.

[63] K. Bathe, S. Bolourchi, Large displacement analysis of three-dimensional beam structures, International Journal for Numerical Methods in Engineering 14 (7) (1979) 961–986.

[64] A. H. Nayfeh, P. F. Pai, Non-linear non-planar parametric responses of an inextensional beam, International Journal of Non-Linear Mechanics 24 (2) (1989) 139–158.

[65] S. C. Stanton, B. A. Owens, B. P. Mann, Harmonic balance analysis of the bistable piezoelectric inertial generator, Journal of Sound and Vibration 331 (15) (2012) 3617–3627.

[66] S. C. Stanton, B. P. Mann, B. A. Owens, Melnikov theoretic methods for characterizing the dynamics of the bistable piezoelectric inertial generator in complex spectral environments, Physica D: Nonlinear Phenomena 241 (6) (2012) 711–720.

[67] R. L. Harne, K. W. Wang, A review of the recent research on vibration energy harvesting via bistable systems, Smart Materials and Structures 22 (2) (2013) 023001.

[68] H. A. Sodano, D. J. Inman, G. Park, A review of power harvesting from vibration using piezoelectric materials, Shock and Vibration Digest 36 (3) (2004) 197–206.

[69] L. Meirovitch, Fundamentals of vibrations, Boston : McGraw-Hill, 2001.

[70] A. H. Nayfeh, P. F. Pai, Linear and nonlinear structural mechanics, Hoboken, N.J. : Wiley-Interscience, Hoboken, N.J., 2004.

[71] B. P. Mann, M. A. Koplow, Symmetry breaking bifurcations of a parametrically excited pendulum, Nonlinear Dynamics 46 (4) (2006) 427–437.

[72] P. Glynne-Jones, M. J. Tudor, S. P. Beeby, N. M. White, An electromagnetic, vibration-powered generator for intelligent sensor systems, Sensors and Actuators A: Physical 110 (1-3) (2004) 344–349.

[73] R. Amirtharajah, A. P. Chandrakasan, Self-powered signal processing using vibration-based power generation, IEEE Journal of Solid-State Circuits 33 (5) (1998) 687–695.

[74] K. E. Graves, D. Toncich, P. G. Iovenitti, Theorectical comparison of motional and transformer emf device damping efficiency, Journal of Sound and Vibration 233 (3) (2000) 441–453.

[75] A. J. Sneller, B. P. Mann, On the nonlinear electromagnetic coupling between a coil and an oscillating magnet, Journal of Physics D: Applied Physics 43 (29) (2010) 295005.

[76] C. Cepnik, O. Radler, S. Rosenbaum, T. Strhla, U. Wallrabe, Effective optimization of electromagnetic energy harvesters through direct computation of the electromagnetic coupling, Sensors and Actuators A: Physical 167 (2) (2011) 416–421.

[77] S. Cheng, D. P. Arnold, A study of a multi-pole magnetic generator for low-frequency vibrational energy harvesting, Journal of Micromechanics and Microengineering 20 (2) (2010) 025015.

[78] M. F. Daqaq, C. Stabler, Y. Qaroush, T. Seuaciuc-Osrio, Investigation of power harvesting via parametric excitations, Journal of Intelligent Material Systems and Structures 20 (5) (2009) 545–557.

[79] U. von Wagner, P. Hagedorn, Piezo-beam systems subjected to weak electric field: experiments and modelling of non-linearities, Journal of Sound and Vibration 256 (5) (2002) 861–872.

[80] S. C. Stanton, A. Erturk, B. P. Mann, D. J. Inman, Nonlinear piezoelectricity in electroelastic energy harvesters: Modeling and experimental identification, Journal of Applied Physics 108 (7) (2010) 074903–9.

[81] A. Triplett, D. D. Quinn, The effect of non-linear piezoelectric coupling on vibration-based energy harvesting, Journal of Intelligent Material Systems and Structures 20 (16) (2009) 1959–1967.

[82] J. Gilbert, F. Balouchi, Comparison of energy harvesting systems for wireless sensor networks, International Journal of Automation and Computing 5 (4) (2008) 334–347.

[83] B. Yang, C. Lee, W. Xiang, J. Xie, J. H. He, R. K. Kotlanka, S. P. Low, H. Feng, Electromagnetic energy harvesting from vibrations of multiple frequencies, Journal of Micromechanics and Microengineering 19 (3) (2009) 035001.

[84] J. V. Stewart, Intermediate Electromagnetic Theory, River Edge, NJ : World Scientific, 2001.

[85] A. Kovetz, The Principles of Electromagnetic Theory, New York : Cambridge University Press, 1990.

[86] H. A. Sodano, D. J. Inman, G. Park, Comparison of piezoelectric energy harvesting devices for recharging batteries, Journal of Intelligent Material Systems and Structures 16 (10) (2005) 799–807.

[87] H. A. Sodano, D. J. Inman, G. Park, Generation and storage of electricity from power harvesting devices, Journal of Intelligent Material Systems and Structures 16 (1) (2005) 67–75.

[88] K. Cook-Chennault, N. Thambi, A. Sastry, Powering mems portable devices–a review of non-regenerative and regenerative power supply systems with special emphasis on piezoelectric energy harvesting systems, Smart Materials and Structures 17 (4) (2008) 043001.

[89] S. Priya, D. J. Inman (Eds.), Energy harvesting technologies, London : Springer, New York ; London, 2008.

[90] A. Kansal, M. Srivastava, An environmental energy harvesting framework for sensor networks, in: Low Power Electronics and Design, 2003. ISLPED '03. Proceedings of the 2003 International Symposium on, 2003, pp. 481–486.

[91] S. Meninger, J. Mur-Miranda, R. Amirtharajah, A. Chandrakasan, J. H. Lang, Vibration-to-electric energy conversion, Very Large Scale Integration (VLSI) Systems, IEEE Transactions on 9 (1) (2001) 64–76.

[92] N. Stephen, On energy harvesting from ambient vibration, Journal of Sound and Vibration 293 (12) (2006) 409–425.

[93] D. A. W. Barton, S. G. Burrow, L. R. Clare, Energy harvesting from vibrations with a nonlinear oscillator, Journal of Vibration and Acoustics 132 (2) (2010) 021009–7.

[94] I.-H. Kim, H.-J. Jung, B. M. Lee, S.-J. Jang, Broadband energy-harvesting using a two degree-of-freedom vibrating body, Applied Physics Letters 98 (21) (2011) –.

[95] L. Tang, Y. Yang, A multiple-degree-of-freedom piezoelectric energy harvesting model, Journal of Intelligent Material Systems and Structures 23 (14) (2012) 1631–1647.

[96] A. H. Nayfeh, Nonlinear Oscillations, New York : Wiley, 1979.

[97] C. Elachi, Waves in active and passive periodic structures: A review, Proceedings of the IEEE 64 (12) (1976) 1666–1698.

[98] M. S. Kushwaha, Stop-bands for periodic metallic rods: Sculptures that can filter the noise, Applied Physics Letters 70 (24) (1997) 3218–3220.

[99] D. García-Pablos, M. Sigalas, F. R. Montero de Espinosa, M. Torres, M. Kafesaki, N. García, Theory and experiments on elastic band gaps, Physical Review Letters 84 (2000) 4349–4352.

[100] H. Chen, C. T. Chan, Acoustic cloaking in three dimensions using acoustic metamaterials, Applied Physics Letters 91 (18) (2007) 183518–183518–3.

[101] A. Dubi, Monte Carlo applications in systems engineering, New York : Wiley, 2000.

[102] H. W. Coleman, W. G. Steele, Experimentation, validation, and uncertainty analysis for engineers, Hoboken, N.J. : John Wiley & Sons, 2009.

[103] B. P. Mann, D. A. Barton, B. A. Owens, Uncertainty in performance for linear and nonlinear energy harvesting strategies, Journal of Intelligent Material Systems and Structures 23 (13) (2012) 1451–1460.

[104] E. P. Furlani, Permanent magnet and electromechanical devices : materials, analysis, and applications, London : Academic, San Diego, Calif., 2001.

Biography

Benjamin Andrew Michael Owens was born on November 12, 1987 in Irving, Texas. He received his BSE degree in Mechanical Engineering and Materials Science from Duke University in 2010 and earned his MS in Mechanical Engineering from Duke in December of 2012. Ben met his wife Julie during the course of his time in Durham and they married in Hillsborough, North Carolina on June 7, 2014. Following his PhD, Ben and Julie will be moving to the DC area where Ben will be joining Applied Predictive Technologies in Arlington, Virginia as a business consultant.

Journal Publications

Mann, B.P., Owens, B.A., "Investigations of a nonlinear energy harvester with a bistable potential well," *Journal of Sound and Vibration,* Volume 329, Issue 9, 26 April 2010, Pages 1215-1226.

Owens, B.A.M., Mann, B.P., "Linear and nonlinear electromagnetic coupling models in vibration-based energy harvesting," *Journal of Sound and Vibration,*, Volume 331, Issue 4, 13 February 2012, Pages 922-937.

Stanton, C.S., Mann, B.P., Owens, B.A.M., "Melnikov theoretic methods for characterizing the dynamics of the bistable piezoelectric inertial generator in complex spectral environments," *Physica D: Nonlinear Phenomena*, Volume 241, Issue 6, 15 March 2012, Pages 711-720.

Stanton, C.S., Owens, B.A.M., Mann, B.P., "Harmonic balance analysis of the bistable piezoelectric inertial generator," *Journal of Sound and Vibration*, Volume 331, Issue 15, 16 July 2012, Pages 3617-3627.

Mann, B.P., Barton, D.A.W., Owens, B.A.M., "Uncertainty in performance for linear and nonlinear energy harvesting strategies," *Journal of Intelligent Material Systems and Structures*, Volume 23, Issue 13, 1 September 2012, Pages 1451-1460.

Bernard, B.P., Owens, B.A.M., Mann, B.P., "Uncertainty Propagation in the Band Gap Structure of a 1D Array of Magnetically Coupled Oscillators," *Journal of Vibration and Acoustics*, Volume 135, Issue 4, 6 June 2013, Pages 041005:1-7.

Owens, B.A.M., Stahl, M.T., Corron, N.J., Blakely, J.N., Illing, L. "Exactly solvable chaos in an electromechanical oscillator," *Chaos,* Volume 23, Issue 3, 15 July 2013, Pages 033109:1-9.

Owens, B.A.M., Mann, B.P. "Mode shape analysis for nonlinear tip interactions of a cantilever beam," *Journal of Sound and Vibration,* under review.

Owens, B.A.M., Mann, B.P. "Wave propagation, band gaps, and uncertainty in a 2-D lattice of beams with magnetic tip masses," *Mechanical Systems and Signal Processing,* under review.

Owens, B.A.M., Mann, B.P. "Energy harvesting perspectives for a two beam system with a bistability from magnetic coupling," *International Journal of Non-Linear Mechanics,* under review.